SUBGRID SCALE MODELING FOR LARGE EDDY SIMULATION OF SUPERCRITICAL MIXING AND COMBUSTION

A Dissertation
Presented to
The Academic Faculty

by

Umesh Unnikrishnan

In Partial Fulfillment
of the Requirements for the Degree
Doctor of Philosophy in the
School of Aerospace Engineering

Georgia Institute of Technology
December 2021

SUBGRID SCALE MODELING FOR LARGE EDDY SIMULATION OF SUPERCRITICAL MIXING AND COMBUSTION

Approved by:

Dr. Joseph C. Oefelein, Advisor
School of Aerospace Engineering
Georgia Institute of Technology

Dr. Timothy Lieuwen
School of Aerospace Engineering
Georgia Institute of Technology

Dr. Vigor Yang, Co-advisor
School of Aerospace Engineering
Georgia Institute of Technology

Dr. Ramanan Sankaran
Computational Sciences and
Engineering Division
Oak Ridge National Laboratory

Dr. Suresh Menon
School of Aerospace Engineering
Georgia Institute of Technology

Date Approved: November 05, 2021

To my parents and teachers for imparting their knowledge to me and shaping my personality

ACKNOWLEDGEMENTS

I would like to express my sincere gratitude to my advisors, Prof. Joseph Oefelein and Prof. Vigor Yang for offering their invaluable time, guidance, and support during my Ph.D. program. I thank them for providing me the opportunity and necessary resources to pursue this research topic and further my knowledge in this subject area. I am indebted to their commitment to my success and working with them has been a rewarding learning experience. I would also like to thank Prof. Suresh Menon, Prof. Timothy Lieuwen, and Dr. Ramanan Sankaran for serving on my thesis committee, reviewing my dissertation, and providing constructive feedback that have helped in refining the research directions.

This research was sponsored in part by the Air Force Office of Scientific Research, and I would like to thank Dr. Mitat Birkan for supporting this work. The research was also supported by the Georgia Tech School of Aerospace Engineering through the William R.T. Oakes Endowment and the Ralph. N. Read Endowment grants and I thank the support from these sources. The computing work for this research were conducted using the PACE computing clusters at the Georgia Institute of Technology and the Summit supercomputer at the Oak Ridge National Laboratory, and I would like to acknowledge the resources and support offered by the respective organizations.

I am extremely grateful for my loving parents, brother, and Stuti for their unconditional love, support, and patience through this long journey. I would not have made it this far without their support.

I would like to thank several colleagues - Dr. Xingjian Wang, Dr. Murali Gopal Muraleedharan, Dr. Suo Yang, Dr. Yixing Li, Dr. Balaji Muralidharan, Dr. Kalyana Chakravarthi Gottiparthi, Dr. Reetesh Ranjan, Achyut Panchal, Petro Junior Milan, among many others who I have been fortunate to work with and gain from stimulating discussions, especially during the formative years of my research.

I am grateful to many friends who have helped me sail through this journey and the stressful time – Nitish, Rohit, Prasoon and Anirudh for being amazing and supportive roommates; my friends from the SKY family – Preeti, Sareena, Kartik, Arti, Abhishek, Nanki, Divya, and several others.

Finally, but most importantly, I express my devotion and love to the Divine and my spiritual master Gurudev Sri Sri Ravi Shankar for showering grace and blessings in my life, and for the spiritual practices that have instilled the mental strength and confidence to go through the stressful times and uncertainties during the course of this program.

TABLE OF CONTENTS

LIST OF TABLES

LIST OF FIGURES

LIST OF SYMBOLS AND ABBREVIATIONS

CFD	Computational fluid dynamics
DNS	Direct numerical simulation
LES	Large eddy simulation
SGS	Subgrid scale
DSM	Dynamic Smagorinsky model
DMM	Dynamic mixed model
EOS	Equation of state
LOX	Liquid oxygen
ρ	Density
u_i	Velocity component in the i-th co-ordinate direction
p	Pressure
T	Temperature
Y_k	Mass fraction of the k-th species
e_t	Total energy
h	Specific enthalpy of the mixture
h_k	Specific enthalpy of the k-th species
$\dot{\omega}_k$	Mass production rate of the k-th species due to chemical reactions
$\boldsymbol{Q_c}$	Set of conserved variables
$\boldsymbol{Q}$	Set of primitive state variables
σ_{ij}	ij-th component of the viscous stress tensor
q_j	Heat diffusive flux in the j-th co-ordinate direction
J_{kj}	Mass diffusive flux of the k-th species in the j-th co-ordinate direction

μ	Dynamic viscosity of the mixture
λ	Thermal conductivity of the mixture
D_k	Mass diffusivity of the k-th species in the mixture
R	Specific gas constant
c_p	Specific heat capacity at constant pressure
v	Specific volume
Z	Compressibility factor
f	Mixture fraction
G	Convolution filter kernel
$\overline{\Delta}$	Filter (grid) cutoff scale
Δ_f	Filter width factor
$\widetilde{\boldsymbol{Q}}$	Set of filtered primitive state variables
τ_{ij}^{sgs}	Subgrid scale stress tensor ij-th component
Q_j^{sgs}	Subgrid scale enthalpy fluxes in the j-th coordinate direction
Φ_{kj}^{sgs}	Subgrid scale species fluxes of the k-th species in the j-th coordinate direction
ρ^{sgs}	Subgrid density
H^{sgs}	Subgrid enthalpy
$\mathcal{J}_j^{sgs}$	Subgrid turbulent diffusion
$\mathcal{D}_j^{sgs}$	Subgrid viscous diffusion
$\tilde{S}_{ij}$	Resolved scale strain rate tensor
ν_t	Subgrid eddy viscosity
C_s	Smagorinsky model coefficient
Pr_t	Subgrid Prandtl number

$Sc_{t,k}$	Subgrid Schmidt number of the k-th species
$\widehat{\Delta}$	Test filter scale
C_m	Modified Smagorinsky coefficient in the mixed model
δ	Thickness of the splitter plate
PDF	Probability density function
FDF	Filtered density function
RFM	Reynolds-filtered model
DGM	Dynamic gradient model
SSM	Scale-similarity model

SUMMARY

Advances in computing power in the past three decades have broadened the prospects for computational modeling and simulation methods to substantiate our understanding of turbulent mixing and combustion in aerospace propulsion applications. High-fidelity and predictive capability of modeling and simulation techniques are prerequisite for effective use of numerical simulations in scientific research and development. Large eddy simulation (LES) is a one such powerful technique for turbulent flow research that offers a favorable balance between computational feasibility and level of phenomenological detail. While the LES methodology and accompanying subgrid scale (SGS) modeling have been developed and applied over decades, primarily in the context of low pressure, ideal gas conditions, their extension to complex multi-physics flows encountered in aerospace propulsion requires further refinement. In particular, the application of LES to turbulent flows at high-pressure supercritical conditions presents several new modeling challenges and uncertainties. The scope of this dissertation is to investigate the theoretical LES formalism and SGS modeling framework for compressible, multi-species turbulent mixing and combustion at supercritical pressures. The goal is to identify the deficiencies with the current methodology, and to establish a refined and consistent framework that accurately accounts for all the necessary physics.

In this dissertation, a consistent theoretical formulation of the filtered governing conservation equations is derived without any prior assumptions or simplifications. The derived formulation reveals the presence of several new subgrid terms that are not considered in the conventional framework. To evaluate the relevance of these terms, two-

dimensional direct numerical simulations (DNS) are performed for spatially evolving non-reacting and reacting mixing layers at supercritical pressures. The complete set of terms in the filtered equations are quantified and analyzed using the DNS datasets. Based on the analyses, two new groups of subgrid terms are identified as important quantities to account in the LES framework – the subgrid convective fluxes associated with filtered thermodynamic quantities, and the subgrid diffusive transport fluxes. The distributions of these terms are examined to obtain physical insights regarding the origin and nature of these quantities. The use of Favre-filtered state variables is common in LES of variable density flows. The implications with the use of Favre-filtered state variables to compute filtered quantities in the LES formulation, such as the viscous stresses, heat flux, density, etc. are rigorously investigated, and the residual terms resulting from such simplified representations are quantified. Parametric analyses are performed as a function of the filter resolution to derive resolution considerations for practical LES applications.

The performance and accuracies of two state-of-the-art subgrid modeling approaches for the traditional subgrid fluxes are assessed under the supercritical non-reacting and reacting conditions. The study demonstrates the better performance of scale-similarity based models over the eddy-viscosity based approaches. The decrease in model performances with increasing filter width are quantified, highlighting the importance of appropriate resolution requirements for accurate simulations. The model performances and predicted distributions are also found to be worse for the reacting case, revealing the insufficiency of adopting conventional subgrid modeling approaches such as the gradient diffusion hypothesis for LES of supercritical combustion.

An important modeling requirement identified in this study are the terms associated with filtered equation of state or the filtered density in the derived framework. To address this modeling requirement, novel subgrid modeling approaches are proposed to model the filtered density for the supercritical mixing case. *A priori* tests of these models are conducted and good improvements are demonstrated for the representation of the filtered density.

CHAPTER 1. INTRODUCTION

1.1 Background and motivation

Turbulence is an important phenomenon in a variety of engineering systems. Understanding the physics of turbulent mixing and its interaction with other physical aspects of fluid flows such as thermodynamics, compressibility, chemical reactions, etc. is primary for the development of reliable and efficient propulsion and other energy conversion systems. The multi-scale nature of turbulence and its coupling with non-linear physical processes occurring over a wide range of length and time scales presents severe challenges that impedes advancements in this area. This dissertation focuses on combustion systems that are central to aerospace propulsion applications where fluid mixing and combustion occur at extreme operating conditions. These systems involve a multitude of complex multi-scale, multi-physics phenomena such as turbulence, compressibility effects, multi-species/multi-phase mixing and chemical reactions.

Experimental efforts in this area are often limited by the restrictions in measurement resolutions, inability to obtain simultaneous and detailed information of the complete flow field, or difficulty with establishing experimental measurements at extreme operating conditions. Moreover, the cost and time associated with such efforts could often be a severe deterrent factor. Computational fluid dynamics has growingly enabled the possibility of providing complementary and detailed description of complex flow fields in these systems. But such endeavors are limited by the available computational power. Several modeling and simulation methodologies for turbulent flows have been developed and explored over the years and applied to a broad range of applications.

In recent times, high-pressure combustion has emerged as an important regime of operation for propulsion systems, such as liquid rocket engines (LRE), gas turbines, and internal combustion engines [1]. Higher operating pressures offer several advantages for achieving the desired design goals such as increased cycle efficiency, increased power output, decreased combustor size requirements, and reduced pollutant emissions thereby lowering environment impact of combustion, and is thus suitable for high performance engines. Within these systems, the injection, mixing and reaction of propellants occur at pressures that largely exceed the critical value, in a thermodynamic regime termed as the supercritical state. Another promising application of high-pressure flows is in the use of supercritical CO_2 cycles [2] for turbine power generation that can achieve higher cycle efficiencies than conventional steam-based cycles. In this fluid regime, real-fluid thermodynamic effects are prominent, and the physical behavior of fluids are drastically different from the behavior at lower pressures as will be described in the following section.

1.2 Supercritical fluid flow modeling

A fluid is said to be in a supercritical state when its pressure and temperature are above the critical values. Figure 1.1a shows the thermodynamic phase diagram of a representative fluid. Above the critical point, the distinction between a gaseous and liquid state ceases to exist as the enthalpy of vaporization and surface tension are close to zero [3, 4]. This is also depicted in Figure 1.1b showing the T-v state diagram for oxygen. At subcritical pressures, a characteristic vaporization process occurs as shown by the constant pressure lines within the vapor-liquid saturation curve. However, at supercritical pressures

(p_{cr}=5.04 MPa for oxygen), the transition from liquid-like to gas-like phase happens in a continuous fashion.

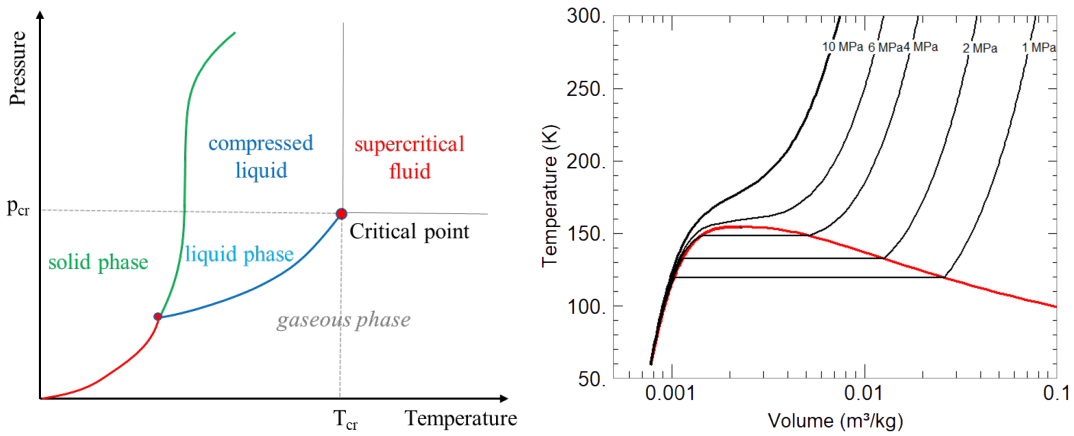

Figure 1.1 - a) Thermodynamic phase diagram of a typical fluid (left) and b) T-v diagram of oxygen (right) [5]. Red solid line shows the vapor-liquid saturation curve.

Several experimental investigations have characterized the differences between injection and mixing of high-pressure jets in subcritical and supercritical environments [6-13]. Figure 1.2 shows visualizations of a liquid nitrogen jet injected into ambient gaseous helium at subcritical and supercritical pressures from the classical experiments by Mayer et al. [7]. Injection of a liquid jet at subcritical pressures exhibits a sharp interface between the injected propellants, and involves jet breakup, ligament formation and atomization processes leading to formation of droplets. The dispersed droplets then undergo vaporization and mix with the ambient fluid. On the other hand, in the supercritical regime a thickened interface is formed between the jet and the surrounding fluid across which the mixing is continuous and controlled by molecular diffusion. Chehroudi et al. [9] measured the spreading rate of cryogenic jets injected into a range of ambient pressures ranging from subcritical and supercritical, and found the jet mixing growth rate to match quantitatively

with the turbulent mixing characteristics of variable density gaseous jets. These findings have also been corroborated with detailed measurements of cryogenic injection by Oschwald et al. [12]. Dahms and Oefelein [14-17] developed a theoretical framework to characterize the mechanism and conditions under which transition from two-phase spray phenomena to diffusion-dominated mixing occur. They showed that the two-phase interface breaks down as a result of thickening of the interfaces and reduction in mean free molecular path, thereby entering the continuum regime where diffusive transport processes dominate. Their analysis showed this to be true for the range of operating conditions and propellant mixtures that are commonly used [15]. These observations support the single-phase assumption that is commonly employed in numerical simulation of supercritical flows.

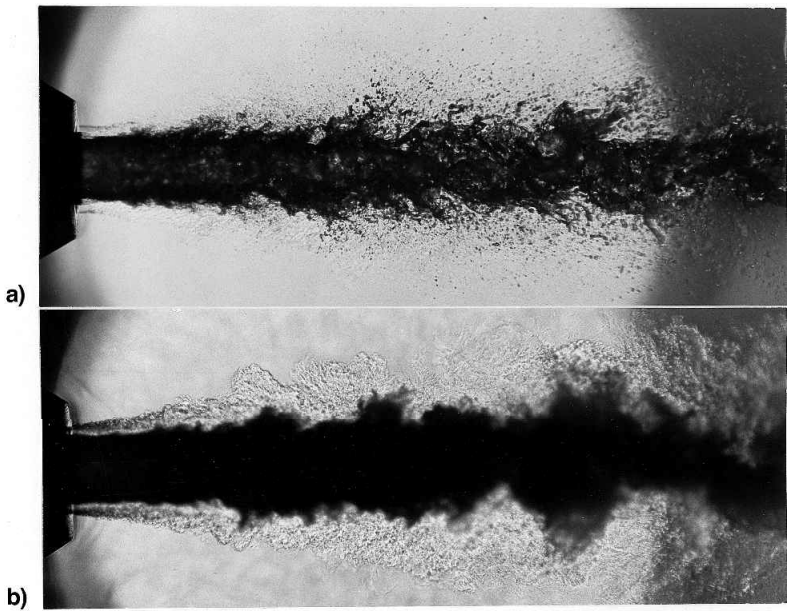

Figure 1.2 - Injection of liquid nitrogen jet into gaseous helium atmosphere at a) subcritical pressure of 1.0 MPa and b) supercritical pressure of 6.0 MPa from experiments of Mayer et al. [7].

In most combustion systems, the propellants are stored in compressed liquid state (at subcritical temperature and supercritical pressure) and injected into an environment which is at supercritical pressure and temperature. This is known as transcritical injection. The fluid undergoes transition from a liquid-like state to a supercritical state, through a process known as pseudo-boiling [18-20]. In this process, the thermodynamic and transport properties exhibit strong anomalies in the form of rapid variations. The specific heat peaks close to the critical point, and the other properties also show drastic variations. For illustration, Figure 1.3 shows the variation of density and specific heat of oxygen across the critical point. These variations manifest in the form of large thermodynamic and density gradients across the interface of transcritical mixing. In particular, the high density gradient magnitude regions which manifest through the distortion of the initial stratification and the jet mixing play an important role in determining the flow dynamics [21, 22]. Measurements of core length and spreading angles of supercritical jets have suggested the density ratio between the injected jet and the ambient to have an important effect on the jet characteristics and mixing [23, 24].

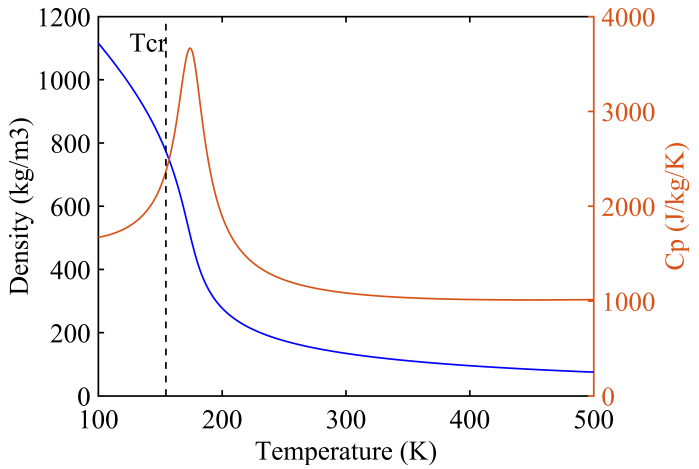

Figure 1.3 - Variation of density and specific heat of oxygen as a function of temperature [25].

Numerical modeling and simulation of transcritical and supercritical mixing and combustion entails a new set of challenges in addition to the classical issues pertaining to the modeling of turbulent fluctuations and non-linear chemical kinetics. At these conditions, real-fluid effects are prominent and must be accounted. This necessitates a consistent theoretical framework derived from first principles of thermodynamics. Oefelein and Yang [26] introduced a framework for incorporating these real-fluid thermodynamic and transport effects within numerical simulations for modeling liquid rocket engine combustion. A systematic treatment of fluid thermodynamics for general fluid flows is presented in Meng and Yang [27]. Detailed review of modeling real-fluid thermodynamic behavior and its application to numerical simulations of flows can be found in other references [1, 3, 4] and will be discussed in Chapter 2.

The non-linearities associated with real-fluid thermodynamics and the formation of large thermodynamic gradients within the diffused interface entails robust and stable numerical schemes. Studies have often reported the formation of spurious pressure oscillations that can destabilize the numerical simulation [28]. To handle the problem of spurious pressure oscillations that arise from the non-linearities of the equation of state, Terashima and Koshi [29, 30] have proposed an approach to solve a pressure evolution equation instead of the total energy equation. However, this does not guarantee proper conservation of energy and results in numerical errors with the computed temperature [31]. Other quasi-conservative approaches have been explored such as the addition of artificial dissipation [32, 33] or use of a double-flux model [34-36].

In majority of the literature in the past, the single-phase assumption is often employed in the modeling and simulation framework. However, there are uncertainties

regarding the validity of this approach in certain operating conditions for some mixtures. It is known that the critical conditions of a mixture could be significantly different from those of its constituent species [37]. In multi-species mixing, the critical pressure of the mixture at a certain composition could be higher than the local pressure resulting in a locally subcritical mixture, even when the injection pressure is supercritical with respect to the individual species. As a result, phase separation and coexistence of vapor and liquid phases could still occur, and these effects must be accounted while modeling the fluid thermodynamic and transport properties. Some experimental studies have reported the presence of spray droplets for different hydrocarbon fuels even at pressures nominally above the critical points of the injected fuel [38-40]. Modeling approaches that consider vapor-liquid equilibrium thermodynamics under such circumstances have been investigated in this context [35, 41, 42]. The problem of phase-separation is pertinent to multi-component mixtures, where the critical pressure of the mixture could be much higher than the constituent species. The disparity between the critical pressures seems to be more prominent for mixtures of long-chain hydrocarbons in general where is a large difference between the molecular configuration between the injectant and the ambient species, than for simpler fuels like hydrogen or methane [43].

Over the last two decades, much progress has been made in the modeling and simulation of supercritical mixing and combustion and some challenges persist [1, 44, 45]. An important aspect of supercritical flows that has not received sufficient focus is the effect of non-ideal, non-linear thermodynamics on the turbulent fluctuations and its implications for turbulence modeling in numerical simulations. Supercritical flows in most practical applications are inherently at high Reynolds numbers owing to the high liquid-like

densities and low gas-like molecular viscosities. The governing interfacial dynamics in the supercritical regime are diffusion-dominated, and turbulence plays an important role in the mixing and transport processes. Studies on supercritical mixing layers have highlighted several key differences in the flow dynamics and turbulence mechanisms of high-pressure flows as compared to atmospheric pressure flows [22, 46]. It is imperative that the turbulence modeling and simulation techniques employed in the study of high-pressure supercritical flows should be able to capture these effects. Before a discussion on these aspects is attempted, an understanding of the historical development of turbulence modeling and its current landscape is necessary.

1.3 The state of the art in turbulence modeling and simulation

Turbulent flows are characterized by non-linear physical processes occurring over a broad range of length and time scales, with the underlying processes at different scales being tightly coupled. This multi-scale, non-linear feature of turbulent flows at high Reynolds numbers is the most challenging aspect for numerical simulations. Resolving the entire range of scales numerically, called the direct numerical simulation (DNS), is the most straight forward approach. However, the computational cost for DNS scales as the cube of the Reynolds number and thus, this technique is restricted to flows at low Reynolds number in simple, confined domains. With significant advances in computing power over the past several years, DNS has been leveraged for multi-physics flows in different regimes [47-49]. However, it is perceived that even with the current and projected developments, DNS would not be amenable for realization of complex flows in practical configurations

and operating conditions. Simulation methods must, therefore, employ some form of modeling to reduce the computational cost requirements while still be able to achieve a quantitative description of the flow to the desired level of phenomenological detail. Reynolds-averaged Navier-Stokes (RANS) is an approach where the effects of all turbulent scales are modeled, and an averaged flow field is computed. The RANS technique is computationally tractable but lacks in the level of fidelity and detail for complex flows where the unsteady dynamics of turbulent fluctuations play a key role. Large eddy simulation (LES) is an intermediate technique between DNS and RANS in terms of computational cost and fidelity of the solution and has found substantial success for the simulation of complex flows over the past years.

1.3.1 Philosophy of large eddy simulation

The philosophy of LES is based on Kolmogorov's hypothesis of local isotropy which states that at sufficiently large Reynolds numbers, the turbulent motions at the small scales are statistically isotropic, and independent of the behavior of the large scales which depend on the flow configuration and boundaries. The large-scale eddies contain the most energy of the flow and play the most dominant role in the flow dynamics. The idea is to then separate and resolve the large-scale motions directly while accounting for the effect of the small scales upon the resolved scale motion. Since the turbulent dynamics at small scales is considered independent of the flow geometry, a universal modeling approach is potentially viable. The idea was first explored by Smagorinsky in the context of meteorological flows [50] and the first numerical LES simulation of a channel flow was conducted by Deardorff [51]. LES has been shown to provide accurate descriptions of flows that are governed by the large-scale turbulent structures.

In most LES implementations, the scale separation is implicitly provided by the numerical discretization of the domain (grid) used in the simulation. By virtue of the numerical discretization, the turbulent field variations below the grid (subgrid) scale are inherently cutoff. The origin of subgrid scale effects is attributed to the non-linear nature of turbulent flows and can be understood from a physical perspective. The turbulent interactions at different length scales being non-linear and coupled, affect physical processes occurring at the remaining scales. The inter-scale interactions of physical processes induce additional effects on the physical dynamics of the resolved scale flow field. These interactions can be broadly perceived as 1) interactions of the resolved scale processes within themselves, 2) interactions of resolved processes with those occurring at the subgrid scales, and 3) the interactions of processes within the subgrid scales. While the interactions of type (1) are resolved directly in LES, the interactions of type (2) and (3) are unresolved but affect the dynamical evolution of the resolved scale field. This enforces the need for additional models, referred to as subgrid scale (SGS) models, to incorporate these effects on the resolved scales of turbulent motion.

1.3.2 Subgrid-scale modeling for LES

Subgrid scale modeling is a central topic of research in the development and application of the LES methodology. As discussed earlier, SGS effects stem from the non-linearities in the governing flow physics. For incompressible flows, the source of non-linearity is the convective flux in the momentum transport. Models which assume an eddy-viscosity hypothesis are commonly used to model the subgrid term associated with the convective flux as a "subgrid stress". The Smagorinsky model [50] is one of the earliest developed model of this form which has been widely used or has served as a foundation

for other modeling approaches. Limitations of the Smagorinsky model include the inability to account for backscatter of energy from the small scales to large scales [52], incorrect limiting behavior in near wall-regions, and ambiguities with the value of the model coefficient [51]. To address these limitations, Germano et al. [53, 54] proposed a dynamic modeling approach to determine the model coefficient within the simulation as a function of space and time using the local resolved flow field. Modeling approaches that do not assume an eddy-viscosity form have also been investigated such as the scale-similarity model [55, 56], gradient model [57], and approximate deconvolution models [58, 59]. Comprehensive reviews of SGS modeling for incompressible flows can be found in [60-62].

For compressible flow applications, additional subgrid terms arise from the non-linearities in the energy equation. SGS models for compressible flows have mostly been derived by extending the earlier described approaches for incompressible flows while considering the compressibility effects. Yoshizawa [63] generalized the Smagorinsky model by introducing a separate model for the isotropic part of SGS stress tensor. Using Germano's dynamic modeling approach, Moin et al. [64] formulated dynamic eddy-diffusivity models for the subgrid stresses and energy fluxes for compressible flows. Erlebacher et al.[65] extended the mixed model of Bardina et al. [66] for the subgrid terms in the momentum and energy equation in their study of compressible isotropic turbulence. Vreman et al. [67] further refined the compressible form of the mixed model by applying the dynamic modeling approach to evaluate the model coefficients and tested their approach for compressible mixing layers.

For reacting flows, the mixing of scalar quantities and subsequent chemical reactions essentially occur at the molecular level which is unresolved. Therefore, the filtered reaction rate in LES must be modeled entirely to account for the turbulence-chemistry interactions, and this presents an additional set of modeling challenges. In reacting LES, subgrid models for the momentum and scalar transport developed for the non-reacting studies were retained along with the simplifying assumptions in the LES formulation, and efforts were mostly focused on modeling the subgrid turbulence-chemistry interactions. A majority of these modeling approaches have been developed through extension of RANS models by using additional information from LES [68, 69]. These include the flamelet-based models [70, 71], conditional-moment closure [72], probability density function (PDF) based closure [73, 74], among others.

DNS serves as a valuable research tool for deriving fundamental insights of the turbulence dynamics in representative conditions, and aid the development of models that can represent the physics of subgrid scales in LES applications [75-77]. Data from DNS simulations also provide a way to evaluate the accuracy and consistency of SGS models in an *a priori* fashion [57, 78]. In the context of incompressible flows, several studies have been undertaken in this direction that have been instrumental in providing an understanding of model characteristics, thereby enabling improvements of different modeling approaches [75, 79]. On the other hand, limited studies are available for compressible turbulence. Moreover, the realization of DNS has so far been possible only for low to moderate Reynolds numbers flows in highly simplified flow configurations, such as homogeneous isotropic turbulence, temporal mixing layers or wall-bounded flows with periodicity. These realizations do not necessarily represent the complete turbulent flow characteristics in

practical systems where the flows are inherently high-Re, anisotropic and inhomogeneous. Vreman et al. [67, 80] used DNS of temporal compressible mixing layers to evaluate the magnitudes of resolved and subgrid terms in the governing equations and assess different models for the subgrid terms. Similar analysis was performed by Martin et al. [81] using DNS of compressible isotropic turbulence. A comprehensive assessment of SGS models in more complex flow configurations and conditions is lacking.

1.3.3 Deficiencies with LES of supercritical mixing and combustion

LES was historically developed in the context of incompressible, single-species, ideal gas flows. LES of incompressible flows has been investigated in great detail and issues have been systematically identified and documented [60, 62, 82-84]. With advancements in computing capabilities over the years, the application of the LES methodology has extended to other multi-physics flow regimes, including compressible flows, and multi-species reacting flows [69, 85, 86]. The increasing interest and need for high-pressure combustion applications provided the motivation to adopt the LES methodology in a number of studies of high-pressure mixing and combustion for propulsion applications by several groups [32, 87-97]. The extension of the methodology incorporates the physical aspects of the flow such as the real-fluid thermodynamics and non-ideal transport phenomena. However, this has not been accompanied by a systematic treatment of the LES formalism and rigorous justification of the underlying simplifications and SGS modeling framework that have been carried over from the low-pressure framework.

Non-ideal gas flows, such as those in supercritical environments, pose a new set of modeling requirements for LES with respect to inclusion of the effects of non-ideal thermodynamics and their interaction with the turbulent fluctuations at the subgrid scales. Bellan and co-workers [21, 46, 98] have conducted a series of DNS of transitional temporal mixing layers at supercritical conditions for different binary species mixtures and Reynolds numbers. These studies revealed distinct effects of flow dynamics under these conditions that are summarized in [22]. A characteristic feature among them is the occurrence of regions with high density gradient magnitudes (HDGM) that are formed through species entrainment and mixing. These regions are found to have an important role in the vorticity dynamics of the flow. It is interpreted that these regions act as a strong source of anisotropy by transferring energy from the normal to tangential fluctuations. It was also shown that the dissipation in supercritical mixing layers contain a substantial contribution from the species and heat fluxes unlike ideal gas flows where most of the small-scale dissipation is attributed to viscous effects [98]. The dissipation was also found to be strongly correlated to the HDGM regions further highlighting their importance to the small-scale dynamics. These findings suggest that modeling approaches need to account for these physics, and the adoption of existing SGS models must precede a careful validation.

Using these DNS databases, Selle et al. [99] evaluated the magnitudes of terms in the filtered equations to assess the validity of assumptions that are typically made in LES formulation of low-pressure flows. Their studies revealed that the subgrid terms associated with the filtered pressure and diffusive heat flux terms, which are considered negligible for ideal gas flows, are particularly relevant under supercritical conditions. A similar study has also been reported by Borghesi and Bellan [100] for multi-species mixing. Ma et al. [101]

examined reacting hydrogen shear layers and reported that the significance of these two additional subgrid terms are increased compared to non-reacting flows. The magnitudes of the terms were also found to increase with Reynolds number. Foster and Miller [102] investigated the subgrid contributions from the filtered diffusive mass fluxes in reacting hydrogen-oxygen mixing layers. Their findings suggest that the subgrid diffusive mass fluxes are considerable and comparable to the subgrid species flux in regions of high SGS scalar dissipation and temperature variance. Lapenna and Creta [103] performed DNS of temporal jets at transcritical and supercritical conditions, and quantified the errors in the evaluation of various thermodynamic and transport properties when subgrid effects are not considered. The errors were shown to be particularly prominent in the transcritical case in which strong variation of properties occur across the pseudo-boiling interface.

The enhanced significance of these terms in this flow regime can be attributed to the non-linearities associated with the non-ideal thermodynamics and the associated state relations which are used to compute the pressure and transport quantities such as the thermal conductivity and heat flux, etc. As a result of these non-linearities, the filtered representation of the terms become non-trivial, and the simplifications applied in the conventional LES formulation are no longer valid.

One peculiar aspect with respect to modeling of high-pressure flows is the equation of state (EOS) that defines the relationship among the thermodynamic state variables – pressure, density, temperature, and mixture composition. This is an important modeling consideration for high-pressure flows where real-fluid effects are significant. Therefore, an accurate representation of filtered EOS in the LES framework for supercritical mixing and combustion applications is essential. Recent studies [99, 103, 104] have highlighted the

deficiencies with the conventional simplification and the need for incorporating subgrid scale effects in the closure of the real-fluid EOS. This problem is also relevant under ideal gas conditions for compressible, multi-species flows as pointed out by Ribert et al. [105], but gains more significance under supercritical conditions [104]. There have been some preliminary attempts to address this issue [100, 106, 107] with limited success but further studies are necessary before a SGS model that can be implemented in LES can be made available.

A major limitation with the past studies on supercritical turbulent mixing is that they considered temporal shear layer configurations that do not depict the complete spatial-temporal characteristics of spatially inhomogeneous turbulence. Moreover, the Reynolds numbers considered in these studies were in the transitional regime of the order of 1000-4000, where the scale separation and dynamics of small scales are much different from those of practical high Reynolds number flows. Consequently, the conclusions reached regarding subgrid effects from these studies require further validation.

1.4 Objectives and outline of the dissertation

It is perceived that the realization of DNS for systems of practical interest will be limited in the foreseeable future even with projected advancements in high performance computing, and LES will remain an important tool for design and analysis of practical combustion and fluid-based power generation systems. Considering the uncertainties that exist around the LES formalism and its applicability at supercritical conditions, it is worthwhile to examine the current approach and identify the deficiencies. The overarching

goal of this dissertation research is to investigate the LES-SGS modeling framework for supercritical mixing and combustion and to provide a refined understanding of the modeling issues. Specifically, this thesis aims to address the following questions.

1. The current LES formulation is founded on underlying assumptions and simplifications, most of which have been carried over from the historical implementations in much simpler flow regimes. Here the term "simpler" is used to refer to flows that are incompressible or weakly compressible, involving single species and at ideal gas conditions. Specifically, the formulation involves simplified representations of filtered terms and neglect of certain correlations and subgrid terms that are either absent or found negligible in other flow regimes. These assumptions require examination in the light of complex multi-physics flow conditions at supercritical conditions. To this end, a systematic derivation of the LES formulation is presented in Chapter 2. The derived formulation takes into account the coupled multi-physics, multi-scale nature of the flow at these conditions, and highlights all the filtered terms that are obtained devoid of any simplifications.
2. Data from highly resolved DNS simulations at relevant operating conditions is necessary to obtain a quantitative understanding of the terms in the derived filtered equations, undertake an *a priori* assessment of the relevance of different terms and determine the acceptable simplifications that can be made. As part of this dissertation research, DNS of turbulent mixing layers are performed at high Reynolds numbers under compressible, supercritical, non-reacting and reacting conditions. Data from these simulations is used to compute the complete set of filtered terms in the governing equations and assess the relevance of different terms to establish modeling

requirements for LES. These are reported in Chapter 4 and Chapter 5 for the non-reacting and reacting cases respectively.

3. There have been limited studies on the assessment of SGS models under supercritical conditions. Moreover, the performance of models as a function of filter or grid size is important to understand the efficacy of different models for practical LES applications, where grid resolution is a primary constraint for computational feasibility. Chapter 6 presents an evaluation of two state-of-the-art modeling approaches that have been successfully used for low-pressure flows. The accuracies of the SGS models are evaluated at different filter widths for the non-reacting and reacting cases.
4. Literature suggests that the subgrid effects in the filtered equation of state are relevant for multi-component mixtures, especially at supercritical conditions. A subgrid modeling approach to account for these effects is thus required, and modeling efforts in this direction are scarce. To address this problem, modeling approaches for the filtered equation of state are proposed and formulated based on existing turbulence theories. The accuracies of these models are investigated for the supercritical mixing case. The model formulations and *a priori* assessments are presented in Chapter 7.

Finally, a summary of the research accomplishments, including key conclusions drawn from this research, and recommended directions for future efforts in this topic are provided in Chapter 8.

CHAPTER 2. THEORETICAL FORMULATION FOR LES

This chapter introduces the governing equations for multi-component flows under the general compressible, high-pressure conditions, followed by the mathematical background required for LES filtering. A systematic derivation of the filtered equations for LES is then presented for flows at the described conditions. The derived formulation is devoid of any simplifications that are made in the incompressible, ideal gas formulation, and is therefore applicable to fluid flows over the entire range of thermodynamic conditions. The formulation highlights all relevant terms that result from the mathematical filtering operation, including those that vanish or are neglected in the current LES implementations. The mathematical and physical significance of these terms are discussed in the context of supercritical turbulent multi-species mixing. Finally, formulations of representative subgrid models that have been developed for the conventional subgrid fluxes are described.

2.1 Instantaneous governing equations

The governing equations for fluid motion in the continuum regime are differential equations that derived from the conservation principles of total mass, momentum, energy, and individual species masses, along with constitutive relations for the viscous stresses, diffusive fluxes, and a thermodynamic equation of state. The system of equations is valid at all scales of motions representative of turbulent flows and provides the theoretical framework to perform DNS simulations.

2.1.1 Conservation equations and constitutive relations

Mass

$$\frac{\partial \rho}{\partial t} + \frac{\partial \rho u_j}{\partial x_j} = 0 \tag{2.1}$$

Momentum

$$\frac{\partial \rho u_i}{\partial t} + \frac{\partial}{\partial x_j}(\rho u_i u_j + p\delta_{ij}) = \frac{\partial \sigma_{ij}}{\partial x_j} \tag{2.2}$$

Energy

$$\frac{\partial \rho e_t}{\partial t} + \frac{\partial}{\partial x_j}\left(\rho\left(h + \frac{1}{2}u_i u_i\right)u_j\right) = \frac{\partial}{\partial x_j}(q_j + \sigma_{ij}u_i) \tag{2.3}$$

Species

$$\frac{\partial \rho Y_k}{\partial t} + \frac{\partial}{\partial x_j}(\rho Y_k u_j) = \frac{\partial}{\partial x_j}(J_{kj}) + \dot{\omega}_k \tag{2.4}$$

Here $\rho, u_i, p, and\ Y_k$ denote the density, velocity components, pressure, and mass fraction of species k, respectively. $\dot{\omega}_k$ denotes the mass production rate of species k due to chemical reactions in a reacting flow system. The specific total energy e_t is defined as, $e_t = e + u_i u_i/2$, where e is the internal energy per unit mass of the mixture and includes the sensible energy and the heats of formation of all the species in the given mixture. The

specific enthalpy of the mixture is defined as $h = (e + p/\rho)$ and the corresponding total specific enthalpy is $h_t = h + u_j u_j/2$. The notation $\boldsymbol{Q_c} = \{\rho, \rho u_i, \rho e_t, \rho Y_k\}$ is introduced to denote the set of conservative quantities that are solved for in the above conservative formulation.

In addition, constitutive relationships are required for the diffusive fluxes, namely the viscous stress tensor σ_{ij}, the heat fluxes q_j and the diffusive fluxes J_{kj} of species k. These are given as

$$\sigma_{ij} = \mu\left[\left(\frac{\partial u_i}{\partial x_j} + \frac{\partial u_j}{\partial x_i}\right) - \frac{2}{3}\frac{\partial u_k}{\partial x_k}\delta_{ij}\right] \tag{2.5}$$

$$q_j = -\lambda\frac{\partial T}{\partial x_j} + \rho\sum_{k=1}^{N} h_k D_k \frac{\partial Y_k}{\partial x_j} \tag{2.6}$$

$$J_{kj} = \rho D_k \frac{\partial Y_k}{\partial x_j} \tag{2.7}$$

The thermodynamic and transport properties, including the dynamic viscosity μ, thermal conductivity λ, mass diffusivity of the k^{th} species D_k, specific enthalpy of the k^{th} species h_k, mixture specific internal energy e and mixture specific enthalpy h, are evaluated from fundamental thermodynamic theories to be discussed in Section 2.1.3. In this formulation, radiation and body forces are neglected. The viscous stress tensor is based on the assumptions of Newtonian fluid and Stokes hypothesis. The heat and mass diffusive fluxes are assumed to follow Fourier and Fick's laws respectively. Dufour and Soret cross-

diffusion effects are neglected in Equations (2.6) and (2.7) respectively. Studies investigating their significance have yielded contrasting conclusions and a general agreement regarding the need for including these terms has not yet been reached [88, 108-110]. Moreover, the diffusivity coefficients for these effects are difficult to obtain under flow conditions considered. For these reasons, and to enable a focused discussion on the filtering procedure, these terms are not considered in this work. However, note that this assumption is not necessary for the derivation of the filtered equations presented in this chapter, and can easily be relaxed. Once the reader is acquainted with the derivation of the filtered equations and the subgrid terms that follow in Section 2.3, the filtered and subgrid components corresponding to the cross-diffusion terms can also be constructed and included in the formulation in future efforts if found necessary.

For simulation of supercritical flows, a primitive-variable based approach is often used where the pressure and temperature are computed directly from the conservation equations instead of density and internal energy [103, 111, 112]. This approach eliminates the need for expensive iterative schemes to compute the pressure and temperature from the density and internal energy. The set of primitive state variables computed in this approach is denoted as $\boldsymbol{Q} = \{p, u_i, T, Y_k\}$, and all other secondary quantities are computed from the primitive variables in a form $\phi = \phi(\boldsymbol{Q})$. The set of conservative variables and primitive variables can be related to each other through a unique transformation $\boldsymbol{Q} = F(\boldsymbol{Q_c})$. The expression for the constitutive relations for thermodynamic quantities are easier to represent and compute using the primitive state variables, and this transformation is applied as an intermediate step even in conservative-variable approaches.

2.1.2 Equation of state

The simulation of compressible flows requires a thermodynamic equation of state that provides the relationship among the thermodynamic state variables, such as pressure, temperature and density for a given mixture composition. For low-pressure gas flows, the ideal gas equation of state can be used. However, real-fluid effects become dominant at high-pressures and these need to be accounted through a real-fluid equation of state. Cubic equations of state such as Peng-Robinson (PR) [113], Redlich-Kwong (RK) [114] or the Soave-Redlich-Kwong (SRK) [115] are frequently used in practice to balance computational efficiency and model accuracy. These equations provide semi-empirical corrections to account for intermolecular forces and molecular volume effects. Although more accurate equations of state are also available, these are not amenable to CFD applications considering the computational cost. It is important to point to the fact that in simulation of real-fluid flows, the contribution of the real-fluid property evaluations alone could account for about 50% of the computational cost [116, 117].

Cubic equations of state can be represented in general form as

$$p = \frac{RT}{(v - b_m)} - \frac{a_m}{v^2 + uvb_m + wb_m{}^2} \tag{2.8}$$

where the parameters $(u, w) = (2, -1)$ for the PR and $(1,0)$ for the SRK equations of state. R is the specific gas constant and v is the specific volume which is the reciprocal of the density ρ. The coefficients a_m and b_m account for intermolecular interactions and molecular volume effects within the mixture, and these are functions of the temperature

and mixture composition. For a multi-component mixture, these coefficients are obtained from the coefficients of the respective components using the mixing rules derived from the extended corresponding states principle [118, 119].

$$a_m = \sum_{i=1}^{N}\sum_{j=1}^{N} X_i X_j a_{ij} \qquad b_m = \sum_{i=1}^{N}\sum_{j=1}^{N} X_i X_j b_{ij}$$
$$a_{ij} = \sqrt{a_i a_j}\left(1 - k_{ij}\right) \qquad b_{ij} = \frac{1}{8}\left(b_i^{\frac{1}{3}} + b_j^{\frac{1}{3}}\right)^3 \left(1 - l_{ij}\right) \tag{2.9}$$

a_i and b_i are the coefficients of the individual pure components of the mixture. The values for a given species can be obtained as a function of the temperature and critical properties, depending upon the form of the equation of state used [120]. k_{ij} and l_{ij} are the binary interaction coefficients that account for intermolecular forces and volumetric effects respectively among the mixture components. Detailed expressions of the model coefficients and recommended values of the parameters can be found in [120].

The equation of state can alternatively be expressed in terms of the compressibility factor Z as

$$p = \rho RTZ \tag{2.10}$$

The compressibility factor quantifies the deviation from the ideal gas behavior and $Z \to 1$ at low pressures and high pressures. The compressibility factor can be computed through an alternate form of the cubic equation of state as [1]

$$Z^3 - (1 + B - uB)Z^2 + (A + wB^2 - uB - uB^2)Z - (AB + wB^2 + wB^3) \quad (2.11)$$

where $A = a_m \frac{p}{R^2T^2}$ and $B = b_m \frac{p}{RT}$.

This form is explicit in terms of pressure and temperature and allows the compressibility function to be computed directly through an analytical solution. Here, the highly non-linear nature of Equations (2.9)-(2.11) is emphasized which will be shown to have important implications for LES filtering.

In the primitive-variable approach where the pressure and temperature are computed directly, the equation of state is used to compute the density from the primitive state variables through the compressibility factor as

$$\rho(\boldsymbol{Q}) = \frac{p}{RTZ} \quad (2.12)$$

Note that R and Z are also functions of the primitive state variables $\boldsymbol{Q}$.

2.1.3 Thermodynamic and transport properties for real-fluid mixtures

The evaluation of thermodynamic properties, such as enthalpy, internal energy, specific heat, etc., for real-fluid mixtures is done in two steps. First, the properties of the mixture are computed at a reference pressure from the corresponding reference state properties of the component species. The reference pressure p^0 is taken to be at a value where ideal gas conditions can be assumed, and the reference state properties of the component species are combined using the ideal gas mixing laws. Departure functions are

then computed to provide the dense-fluid corrections to account for high-pressure effects [120]. These departure functions are derived from Maxwell's relations [121] and are given as

$$C_p(T,\rho) - C_{v0}(T) = -\int_{\rho_0}^{\rho}\left[\frac{T}{\rho^2}\left(\frac{\partial^2 p}{\partial T^2}\right)_\rho\right]_T d\rho + \frac{T}{\rho^2}\frac{(\partial p/\partial T)_\rho^2}{(\partial p/\partial \rho\,)_T}$$

$$h(T,p) - h_0(T) = -\int_{p_0}^{p}\left[\frac{1}{\rho} + \frac{T}{\rho^2}\left(\frac{\partial \rho}{\partial T}\right)_p\right]_T dp$$

$$e(T,\rho) - e_0(T) = -\int_{\rho_0}^{\rho}\left[\frac{p}{\rho^2} - \frac{T}{\rho^2}\left(\frac{\partial p}{\partial T}\right)_\rho\right]_T d\rho$$

The thermodynamic derivatives in the departure function expressions are obtained directly from the chosen form of the equation of state.

The computation of transport properties is done in a similar fashion. The reference-state properties of the mixture are obtained from the corresponding reference-state properties of the component species. The deviations from the reference state can be obtained using the extended corresponding states methodologies of Ely and Hanley [122, 123] or Chung et al. [124] for the mixture molecular viscosity and thermal conductivity. For the binary mass diffusivities, the corrections are computed using the corresponding states methodology given by Takahashi [125].

For multi-component mixtures, a mixture-averaged diffusion coefficient is considered for each species that represent the diffusivity of the species into the mixture. This is computed using Wilke's mixing rule [126, 127] as

$$D_k = \frac{1 - Y_k}{\sum_{\substack{i=1 \\ i \neq k}}^{N} X_i / D_{ki}}$$

Detailed reviews of thermodynamic and transport property evaluation at high-pressure conditions can be found in references [1, 3, 27, 128-130]. At this point, a discussion on the non-linearities in the thermodynamic and transport property evaluation framework are in order. For a compressible flow involving a thermally perfect, calorically imperfect gas, the temperature dependence of thermodynamic and transport properties are approximated as non-linear polynomial functions. The ideal-gas mixing rules involve a coupling of the mixture composition and the fluid properties, and thereby temperature. For the case of high-pressure non-ideal fluids, the departure functions pose further sources of complex non-linearities within the governing system of equations. These non-linearities among the different fluid properties and state variables coupled with the multi-scale nature of turbulent flows has important ramifications for the flow evolution at different turbulent scales.

2.2 Mathematical background of LES filtering

Before deriving the LES equations, it is necessary to establish a strong mathematical foundation of the LES filtering procedure and its mathematical properties. This will facilitate an understanding of the derivation of the LES equations and identification of the deficiencies with the current formulation.

2.2.1 Convolution kernel and its properties

The governing equations for the large, resolved scales in LES are derived from the instantaneous equations by applying a low-pass spatial filtering operation that filters the small-scale information from the flow-field and retains the large-scale information. Accordingly, an instantaneous field variable ϕ can be decomposed as the sum of its filtered (resolved) component $\bar{\phi}$ and the subgrid component ϕ'.

$$\phi = \bar{\phi} + \phi' \tag{2.13}$$

This is analogous to the classical Reynolds decomposition in RANS where the variable is decomposed into an ensemble-averaged and the corresponding fluctuating component. The filtered variable $\bar{\phi}$ is, however, an unsteady term that includes information of the large-scale turbulent fluctuations in space and time.

The filtering operation is defined by the convolution integral

$$\overline{\phi(\boldsymbol{x}, t)} = \iiint_V \phi(\boldsymbol{r}, t) G(\boldsymbol{x} - \boldsymbol{r}, t; \overline{\Delta}) d\boldsymbol{r} \tag{2.14}$$

where the kernel G defines the filter function that filters out information from scales smaller than the cutoff length-scale $\overline{\Delta}$, called the filter scale. V denotes the volume of the domain in which the flow field occurs.

A number of filter kernels have been considered such as the box (top-hat), Gaussian and spectral cutoff filters [131]. The properties of the filter that is used in implicitly filtered

LES is determined by the resolution characteristics of the numerical discretization scheme. The top-hat filter is characteristic of the explicit finite-volume/finite-difference schemes used in most CFD solvers. For a top-hat filter, the filter kernel is given by a constant within a local filter volume V_Δ defined by a sphere of radius equal to the filter width Δ, and the convolution integral represents the volume averaged flow-field within the filter volume.

$$G(\boldsymbol{r};\Delta) = \begin{cases} \frac{1}{\overline{\Delta}} & |\boldsymbol{r}| \leq \frac{\overline{\Delta}}{2} \\ 0 & |\boldsymbol{r}| > \frac{\overline{\Delta}}{2} \end{cases} \tag{2.15}$$

$$\overline{\phi(\boldsymbol{x},t)} = \frac{1}{V_{\overline{\Delta}}} \iiint_{V_{\overline{\Delta}}} \phi(\boldsymbol{r},t)d\boldsymbol{r} \tag{2.16}$$

For non-isotropic filters, as is the case for cartesian grid discretization, a filter width can be defined for each co-ordinate direction and the resulting filtering operation represents the volume-averaged field within the corresponding finite volume cell. The filter is a linear operator that is commutative with the spatial and temporal derivatives for homogeneous filter widths. However, for practical flows which are essentially non-isotropic and inhomogeneous, the grid and hence the filter kernel must be a function of space in accordance with the variation of turbulent length scales in different regions of the flow. In this case, the filtering operator is not commutative in general with the differential operator, and results in commutation errors. It has been shown that these errors are of the same order as the discretization errors of the numerical scheme [132]. Alternatively, one can consider the governing equation transformed in the computational space, as is typically done in numerical simulations using non-uniform grids and perform the filtering procedure in the

computational space. The filter width is then defined in the computational space and is uniform, and the filtering and derivative operations are commutative in the computational space, if appropriate filtered transformation metrics are considered [133]. Development of alternate filters that are commutative with the derivative operators on non-uniforms grids have also been attempted [134-136] with applications to explicitly filtered LES. These numerical issues will not be tackled in this dissertation and the filtering will be based on the computational space.

The most important property of the convolution integral is that it is non-commutative with respect to non-linear functions. For example, the filter of a product of two variables is not equal to the product of the respective filtered variables. More generally, the filtered value of a non-linear function is not equal to the function evaluated using the filtered parameters. This can be mathematically represented as

$$\overline{\phi_1\phi_2} \neq \overline{\phi_1}\,\overline{\phi_2}$$
$$\overline{\psi(\phi_1, \phi_2, \dots, \phi_n)} \neq \psi(\overline{\phi_1}, \overline{\phi_2}, \dots, \overline{\phi_n}) \tag{2.17}$$

This inequality is the mathematical source of the subgrid terms. The basis of this inequality can be interpreted from a physical perspective. The filtered quantity on the left-hand side represents the net contribution of the quantity at the resolved scales of motion and includes the effects of all interscale interactions across the resolved and subgrid scales. In contrast, the right-hand side represents contributions purely from the resolved scales of motion. The correlations of the left-hand side are generally not computed directly in LES since they require complete information of the correlation among the variables at all scales.

Hence the difference between the two quantities which represents the subgrid scale correlation must be modeled.

2.2.2 Favre-filtering and its implications

For variable density flows, an additional Favre-filtering operation is defined [137] to provide a simplified representation of the filtered governing equations in a form that closely resembles the unfiltered equations. The Favre-filtering operator is given as

$$\tilde{\phi} = \frac{\overline{\rho\phi}}{\bar{\rho}} \tag{2.18}$$

and accordingly, a Favre decomposition can be expressed as

$$\phi = \tilde{\phi} + \phi'' \tag{2.19}$$

This operator is applied for the velocities, energy, and species mass fractions which occur together with density in the conservative formulation, while the Reynolds filtering (Equation (2.14)) is applied for pressure and density.

From Equation (2.18), the Favre-filtering operator is interpreted to implicitly act as a density-weighted filtering operator. This aspect has important consequences for flow with large density stratifications or gradients. This is the case for strongly compressible flows, or flows involving large thermodynamic gradients in the form of temperature and/or species composition, as is frequently encountered in combustion. For transcritical and supercritical mixing, density is a strong non-linear function of the state variables, and

consequently the Favre-filtered variable is most likely to differ significantly from the Reynolds-filtered counterpart.

2.3 Filtered equations for LES

2.3.1 Filtered conservation equations

The system of equations that govern the dynamics of the resolved large eddies can be derived by applying the filtering operator on the conservation equations (2.1)-(2.4). The filtered conservation equations can be written as

$$\frac{\partial \overline{\rho(\boldsymbol{Q})}}{\partial t} + \frac{\partial}{\partial x_j}\left(\overline{\rho(\boldsymbol{Q})}\tilde{u}_j\right) = 0 \tag{2.20}$$

$$\begin{aligned} &\frac{\partial\left(\overline{\rho(\boldsymbol{Q})}\tilde{u}_i\right)}{\partial t} + \frac{\partial}{\partial x_j}\left(\overline{\rho(\boldsymbol{Q})}\tilde{u}_i\tilde{u}_j + \bar{p}\delta_{ij}\right) \\ &\qquad = \frac{\partial}{\partial x_j}\overline{\sigma_{ij}(\boldsymbol{Q})} - \frac{\partial}{\partial x_j}\overline{\rho(\boldsymbol{Q})}\left(\widetilde{u_i u_j} - \tilde{u}_i\tilde{u}_j\right) \end{aligned} \tag{2.21}$$

$$\begin{aligned} &\frac{\partial\left(\overline{\rho(\boldsymbol{Q})}\widetilde{e_t(\boldsymbol{Q})}\right)}{\partial t} + \frac{\partial}{\partial x_j}\left(\overline{\rho(\boldsymbol{Q})}\left(\widetilde{h(\boldsymbol{Q})} + \frac{1}{2}\tilde{u}_i\tilde{u}_i\right)\tilde{u}_j\right) \\ &\qquad = \frac{\partial}{\partial x_j}\left\{\overline{q_j(\boldsymbol{Q})} + \overline{u_i\sigma_{ij}(\boldsymbol{Q})} - \overline{\rho(\boldsymbol{Q})}\left(\widetilde{h(\boldsymbol{Q})u_j} - \widetilde{h(\boldsymbol{Q})}\tilde{u}_j\right)\right. \\ &\qquad\qquad \left. - \frac{1}{2}\overline{\rho(\boldsymbol{Q})}\left(\widetilde{u_i u_i u_j} - \tilde{u}_i\tilde{u}_i\tilde{u}_j\right)\right\} \end{aligned} \tag{2.22}$$

$$\frac{\partial \overline{\rho(\boldsymbol{Q})}\tilde{Y}_k}{\partial t} + \frac{\partial}{\partial x_j}\left(\overline{\rho(\boldsymbol{Q})}\tilde{Y}_k\tilde{u}_j\right) = \frac{\partial}{\partial x_j}\left(\overline{J_{kj}(\boldsymbol{Q})} - \overline{\rho(\boldsymbol{Q})}\left(\widetilde{Y_k u_j} - \tilde{Y}_k\tilde{u}_j\right)\right) + \overline{\dot{\omega}_k(\boldsymbol{Q})} \tag{2.23}$$

Here, the Favre-filtering operator, inequalities associated with the filtering operation of non-linear quantities, and commutivity of the filtering and differential operators in the computational space are considered. Commutivity errors associated with the grid transformation metrics are within the order of numerical accuracy and are not considered in this work.

Upto this point, the filtered equations (2.20)-(2.23) closely resemble the conventional LES framework except for the way the filtered secondary quantities, such as the diffusive fluxes, internal energy, and density are treated. The notation $\widetilde{\boldsymbol{Q}}_{\boldsymbol{c}} = \{\bar{\rho}, \bar{\rho}\tilde{u}_i, \bar{\rho}\widetilde{e_t}, \bar{\rho}\tilde{Y}_k\}$ is used to denote the set of conservative variables that are computed in conservative variable-based LES and $\widetilde{\boldsymbol{Q}} = \{\bar{p}, \tilde{u}_i, \tilde{T}, \tilde{Y}_k\}$ is the corresponding set of filtered variables in the primitive variable-based approach.

2.3.2 Filtered equation of state

Depending upon the numerical scheme used, different forms of the equation of state can be implemented either to calculate pressure or density as a function of other state variables. In the conservative variable approach with the equation of state used to compute pressure in Equation (2.8), the filtered pressure is given as

$$\overline{p(\boldsymbol{Q})} = \overline{\frac{RT}{(v(\boldsymbol{Q}) - b(\boldsymbol{Q}))}} - \overline{\frac{a(\boldsymbol{Q})}{v(\boldsymbol{Q})^2 + uv(\boldsymbol{Q})b(\boldsymbol{Q}) + wb(\boldsymbol{Q})^2}} \tag{2.24}$$

In current LES implementations, the filtered pressure is approximated in terms of the filtered state variables as

$$p(\widetilde{\boldsymbol{Q}}) = \frac{R\tilde{T}}{\left(v(\widetilde{\boldsymbol{Q}}) - b(\widetilde{\boldsymbol{Q}})\right)} - \frac{a(\widetilde{\boldsymbol{Q}})}{v(\widetilde{\boldsymbol{Q}})^2 + uv(\widetilde{\boldsymbol{Q}})b(\widetilde{\boldsymbol{Q}}) + wb(\widetilde{\boldsymbol{Q}})^2} \tag{2.25}$$

Based on the derived understanding of the non-linearities associated with the computation of each model parameter in conjunction with the associated mixing rules for multi-component mixtures, and the inequalities that arise from the resulting non-commutivity of the filtering operator (Equation (2.17)), additional subgrid effects are clearly relevant. This can be defined as the subgrid pressure p^{sgs} and given as

$$p^{sgs} = \overline{p(\boldsymbol{Q})} - p(\widetilde{\boldsymbol{Q}}) \tag{2.26}$$

Preliminary studies have shown the relevance of this quantity at high-pressure conditions [99, 104] and even for ideal, multi-component mixtures [105]. The filtered equation of state for a multi-component mixture can equivalently be written as

$$\bar{p} = \overline{\rho Z R T} = \overline{\rho R_u Z T \sum_{k=1}^{n} \frac{Y_k}{W_k}} = \bar{\rho} R_u \sum_{k=1}^{n} \frac{\widetilde{ZTY_k}}{W_k} \tag{2.27}$$

For ideal mixtures ($Z = 1$), the expression involves temperature-species mass fraction covariances which are approximated in current formulations. For non-ideal mixtures, the introduction of the compressibility factor yields a triple covariance that involves a more complex coupling among the thermodynamic state variables.

In the primitive variable-based approach where the equation of state given in the form of Equation (2.12) is used, the filtered density is given as

$$\overline{\rho(\boldsymbol{Q})} = \overline{\left(\frac{p}{Z(\boldsymbol{Q})R(\boldsymbol{Q})T}\right)} \tag{2.28}$$

In current LES implementations, the filtered density is approximated in terms of the filtered variables as

$$\rho(\widetilde{\boldsymbol{Q}}) = \frac{\bar{p}}{Z(\widetilde{\boldsymbol{Q}})R(\widetilde{\boldsymbol{Q}})\tilde{T}} \tag{2.29}$$

The difference between the two expressions yields a subgrid term, which is termed as the subgrid density in this dissertation.

2.3.3 Conventional subgrid terms for convective fluxes

The subgrid terms that are generally considered in Equations (2.21)-(2.23) are those associated with the simplified representation of the covariances in the convective fluxes. These are the subgrid stresses τ_{ij}^{sgs}, subgrid heat flux Q_j^{sgs}, and the subgrid species mass fluxes Φ_{kj}^{sgs} which are defined as,

$$\tau_{ij}^{sgs} = \overline{\rho(\boldsymbol{Q})}\left(\widetilde{u_i u_j} - \tilde{u}_i \tilde{u}_j\right) \tag{2.30}$$

$$Q_j^{sgs} = \overline{\rho(\boldsymbol{Q})}\left(\widetilde{h(\boldsymbol{Q})u_j} - \widetilde{h(\boldsymbol{Q})}\tilde{u}_j\right) \tag{2.31}$$

$$\Phi_{kj}^{sgs} = \overline{\rho(\boldsymbol{Q})}\left(\widetilde{Y_k u_j} - \tilde{Y}_k \tilde{u}_j\right) \tag{2.32}$$

Using the Favre decomposition (Equation (2.19)) the subgrid fluxes associated with the convective terms can be further decomposed into three components, following Germano's decomposition [138] for the subgrid stresses. The decomposition can be expressed in general form as

$$\bar{\rho}\left(\widetilde{\phi_i u_j} - \tilde{\phi}_i \tilde{u}_j\right) = L_{ij} + C_{ij} + R_{ij} \tag{2.33}$$

where,

$$L_{ij} = \bar{\rho}\left(\widetilde{\tilde{\phi}_i \tilde{u}_j} - \tilde{\tilde{\phi}}_i \tilde{\tilde{u}}_j\right)$$

$$C_{ij} = \bar{\rho}\left(\widetilde{\tilde{\phi}_i u_j''} + \widetilde{\phi_i'' \tilde{u}_j} - \tilde{\tilde{\phi}}_i \widetilde{u_j''} - \widetilde{\phi_i''} \tilde{\tilde{u}}_j\right)$$

$$R_{ij} = \bar{\rho}\left(\widetilde{\phi_i'' u_j''} + - \widetilde{\phi_j''} \widetilde{u_j''}\right)$$

L_{ij}, C_{ij} and R_{ij} are termed the Leonard, Cross, and Reynolds terms respectively. These terms are modified from the original Leonard decomposition [139] and satisfy Galilean invariance [140]. The Leonard term represents interactions among the resolved scales of motion. The Cross term is an interscale term representing interactions between

the resolved and subgrid scales, whereas the Reynolds term represents interactions within the subgrid scales that produce a net contribution on the resolved scales. Several modeling approaches for these subgrid fluxes have been investigated and routinely implemented in LES simulations. Some representative models will be discussed in Section 2.4.

The subgrid flux associated with the kinetic energy flux in the filtered energy equation (2.22) can be rearranged as

$$\begin{aligned}\overline{\rho(\boldsymbol{Q})}\left(\widetilde{u_i u_i u_j} - \tilde{u}_i\tilde{u}_i\tilde{u}_j\right) &= \overline{\rho(\boldsymbol{Q})}\left(\left(\widetilde{u_i u_i u_j} - \widetilde{u_i}\tilde{u}_i\tilde{u}_j\right) + \left(\widetilde{u_i}\widetilde{u}_i - \tilde{u}_i\tilde{u}_i\right)\tilde{u}_j\right) \\ &= \overline{\rho(\boldsymbol{Q})}\left(\widetilde{u_i u_i u_j} - \widetilde{u_i}\tilde{u}_i\tilde{u}_j\right) + \tau_{ii}^{sgs}\tilde{u}_j\end{aligned} \tag{2.34}$$

The first term is usually neglected, while the second term is modeled using the subgrid model applied for the subgrid stress. In some studies, this entire term is modeled along with the subgrid enthalpy flux using a gradient diffusivity model. However, there are uncertainties regarding treatment of a mechanical energy term in a manner used for the thermodynamic energy [81]. In this study, this term is considered in its original form without the usual subgrid models or assumptions.

2.3.4 New subgrid terms for diffusive fluxes and thermodynamic quantities

In addition to the subgrid terms for the convective fluxes, new terms arise that are relevant for compressible flows, especially those involving multi-component mixtures and/or supercritical conditions. In current LES formulations, it is customary to adopt a simplified representation for the secondary terms computed in terms of the resolved variables, without any associated correlations. However, considering the inequalities

associated with the convolutional integral of the filtering process as stated in Equation (2.17), this representation is fundamentally incorrect and gives rise to residual terms.

$$\sigma_{ij}^{sgs} = \overline{\sigma_{ij}(\boldsymbol{Q})} - \sigma_{ij}(\widetilde{\boldsymbol{Q}})$$

$$= \overline{\mu(\boldsymbol{Q})\left[\left(\frac{\partial u_i}{\partial x_j} + \frac{\partial u_j}{\partial x_i}\right) - \frac{2}{3}\frac{\partial u_k}{\partial x_k}\delta_{ij}\right]} \tag{2.35}$$

$$- \mu(\widetilde{\boldsymbol{Q}})\left[\left(\frac{\partial \tilde{u}_i}{\partial x_j} + \frac{\partial \tilde{u}_j}{\partial x_i}\right) - \frac{2}{3}\frac{\partial \tilde{u}_k}{\partial x_k}\delta_{ij}\right]$$

$$q_j^{sgs} = \overline{q_j(\boldsymbol{Q})} - q_j(\widetilde{\boldsymbol{Q}})$$

$$= -\overline{\lambda(\boldsymbol{Q})\frac{\partial T}{\partial x_j}} + \overline{\rho(\boldsymbol{Q})\sum_{k=1}^{N} h_k(\boldsymbol{Q})D_k(\boldsymbol{Q})\frac{\partial Y_k}{\partial x_j}} \tag{2.36}$$

$$- \left(-\lambda(\widetilde{\boldsymbol{Q}})\frac{\partial \tilde{T}}{\partial x_j} + \rho(\widetilde{\boldsymbol{Q}})\sum_{k=1}^{N} h_k(\widetilde{\boldsymbol{Q}})D_k(\widetilde{\boldsymbol{Q}})\frac{\partial \tilde{Y}_k}{\partial x_j}\right)$$

$$J_{kj}^{sgs} = \overline{J_{kj}(\boldsymbol{Q})} - J_{kj}(\widetilde{\boldsymbol{Q}}) = \overline{\rho(\boldsymbol{Q})D(\boldsymbol{Q})\frac{\partial Y_k}{\partial x_j}} - \rho(\widetilde{\boldsymbol{Q}})D(\widetilde{\boldsymbol{Q}})\frac{\partial \widetilde{Y}_k}{\partial x_j} \tag{2.37}$$

The diffusive fluxes are expressed as a gradient diffusion term, with each flux term proportional to gradients of primitive variables through the corresponding transport property. For LES of single-component flows under incompressible or weakly compressible conditions, the transport properties are a weak function of temperature and can be treated to be roughly constant. Assuming density variations to be nominal, the terms can then be considered negligible as has been done in compressible LES [64, 65]. However,

this may not be justifiable when the transport properties vary strongly at the subgrid scale. To further understand the aspect of filtering the diffusive fluxes, consider a triple decomposition where the subgrid diffusive flux terms are split into three components based on the level of simplification of the filtering operator.

For example, the subgrid viscous stress σ_{ij}^{sgs} can be decomposed as

$$\sigma_{ij}^{sgs} = \sigma_{ij}^{sgs(1)} + \sigma_{ij}^{sgs(2)} + \sigma_{ij}^{sgs(3)} \tag{2.38}$$

where

$$\sigma_{ij}^{sgs(1)} = \left(\overline{\mu(\boldsymbol{Q})\left[\left(\frac{\partial u_i}{\partial x_j} + \frac{\partial u_j}{\partial x_i}\right) - \frac{2}{3}\frac{\partial u_k}{\partial x_k}\delta_{iJ}\right]} - \overline{\mu(\boldsymbol{Q})}\left[\left(\frac{\partial \bar{u}_i}{\partial x_j} + \frac{\partial \bar{u}_j}{\partial x_i}\right) - \frac{2}{3}\frac{\partial \bar{u}_k}{\partial x_k}\delta_{ij}\right]\right)$$

$$\sigma_{ij}^{sgs(2)} = \overline{\mu(\boldsymbol{Q})}\left(\left[\left(\frac{\partial \bar{u}_i}{\partial x_j} + \frac{\partial \bar{u}_j}{\partial x_i}\right) - \frac{2}{3}\frac{\partial \bar{u}_k}{\partial x_k}\delta_{ij}\right] - \left[\left(\frac{\partial \tilde{u}_i}{\partial x_j} + \frac{\partial \tilde{u}_j}{\partial x_i}\right) - \frac{2}{3}\frac{\partial \tilde{u}_k}{\partial x_k}\delta_{ij}\right]\right)$$

$$\sigma_{ij}^{sgs(3)} = \left(\overline{\mu(\boldsymbol{Q})} - \mu(\tilde{\boldsymbol{Q}})\right)\left[\left(\frac{\partial \tilde{u}_i}{\partial x_j} + \frac{\partial \tilde{u}_j}{\partial x_i}\right) - \frac{2}{3}\frac{\partial \tilde{u}_k}{\partial x_k}\delta_{ij}\right]$$

The first term represents the subgrid covariance between the molecular viscosity and the strain rate. The second term represents the contribution due to subgrid fluctuations of the primitive variables on the molecular viscosity. The third term is the error due to the difference between Favre-filtered and Reynolds-filtered velocities. A similar decomposition can be done for the diffusive heat and species fluxes as well.

For the diffusive heat flux this yields,

$$q_j^{sgs} = q_j^{sgs(1)} + q_j^{sgs(2)} + q_j^{sgs(3)} \tag{2.39}$$

$$q_j^{sgs(1)} = -\overline{\lambda(\boldsymbol{Q})\frac{\partial T}{\partial x_j}} + \overline{\sum_{k=1}^{N} \rho(\boldsymbol{Q}) h_k(\boldsymbol{Q}) D_k(\boldsymbol{Q}) \frac{\partial Y_k}{\partial x_j}}$$

$$-\left(-\overline{\lambda(\boldsymbol{Q})}\frac{\partial \bar{T}}{\partial x_j} + \sum_{k=1}^{N} \overline{\rho(\boldsymbol{Q}) h_k(\boldsymbol{Q}) D_k(\boldsymbol{Q})}\frac{\partial \bar{Y}_k}{\partial x_j}\right)$$

$$q_j^{sgs(2)} = -\overline{\lambda(\boldsymbol{Q})}\left(\frac{\partial \tilde{T}}{\partial x_j} - \frac{\partial \bar{T}}{\partial x_j}\right) + \sum_{k=1}^{N} \overline{\rho(\boldsymbol{Q}) h_k(\boldsymbol{Q}) D_k(\boldsymbol{Q})}\left(\frac{\partial \bar{Y}_k}{\partial x_j} - \frac{\partial \tilde{Y}_k}{\partial x_j}\right)$$

$$q_j^{sgs(3)} = -\left(\overline{\lambda(\boldsymbol{Q})} - \lambda(\tilde{\boldsymbol{Q}})\right)\frac{\partial \tilde{T}}{\partial x_j}$$

$$+ \sum_{k=1}^{N} \left(\overline{\rho(\boldsymbol{Q}) h_k(\boldsymbol{Q}) D_k(\boldsymbol{Q})} - \rho(\tilde{\boldsymbol{Q}}) h_k(\tilde{\boldsymbol{Q}}) D_k(\tilde{\boldsymbol{Q}})\right)\frac{\partial \tilde{Y}_k}{\partial x_j}$$

Similarly, for the species diffusive fluxes,

$$J_{kj}^{sgs} = J_{kj}^{sgs(1)} + J_{kj}^{sgs(2)} + J_{kj}^{sgs(3)} \tag{2.40}$$

$$J_{kj}^{sgs(1)} = \overline{\rho(\boldsymbol{Q}) D(\boldsymbol{Q}) \frac{\partial Y_k}{\partial x_j}} - \overline{\rho(\boldsymbol{Q}) D(\boldsymbol{Q})}\frac{\partial \bar{Y}_k}{\partial x_j}$$

$$J_{kj}^{sgs(2)} = \overline{\rho(\boldsymbol{Q})D_k(\boldsymbol{Q})}\left(\frac{\partial \bar{Y}_k}{\partial x_j} - \frac{\partial \tilde{Y}_k}{\partial x_j}\right)$$

$$J_{kj}^{sgs(3)} = \left(\overline{\rho(\boldsymbol{Q})D_k(\boldsymbol{Q})} - \rho(\widetilde{\boldsymbol{Q}})D_k(\widetilde{\boldsymbol{Q}})\right)\frac{\partial \tilde{Y}_k}{\partial x_j}$$

In addition, subgrid terms also arise from the non-linearities associated with computation of thermodynamic quantities such as density, internal energy, and enthalpy. The subgrid density resulting from the filtered equation of state was discussed in Section 2.3.2. In the energy equation, additional subgrid terms result from the simplification of the filtered enthalpy, kinetic energy fluxes, and the viscous diffusion terms. These can be denoted as

$$\rho^{sgs} = \overline{\rho(\boldsymbol{Q})} - \rho(\widetilde{\boldsymbol{Q}}) \tag{2.41}$$

$$H^{sgs} = \overline{\rho(\boldsymbol{Q})h(\boldsymbol{Q})} - \rho(\widetilde{\boldsymbol{Q}})h(\widetilde{\boldsymbol{Q}}) \tag{2.42}$$

$$\mathcal{J}_j^{sgs} = \frac{1}{2}\left(\overline{\rho(\boldsymbol{Q})u_i u_i u_j} - \overline{\rho(\boldsymbol{Q})}\tilde{u}_i\tilde{u}_i\tilde{u}_j\right) \tag{2.43}$$

$$\mathcal{D}_j^{sgs} = \overline{u_i\sigma_{ij}(\boldsymbol{Q})} - \tilde{u}_i\sigma_{ij}(\widetilde{\boldsymbol{Q}}) \tag{2.44}$$

2.3.5 Filtered equations for a priori analyses

With the incorporation of the subgrid term definitions discussed in Sections 2.3.3 and 2.3.4, the final set of filtered equations can be recast as

$$\frac{\partial\overline{\rho(\boldsymbol{Q})}}{\partial t}+\frac{\partial}{\partial x_j}(\rho(\widetilde{\boldsymbol{Q}})\tilde{u}_j)+\frac{\partial}{\partial x_j}(\rho^{sgs}\tilde{u}_j)=0 \tag{2.45}$$

$$\frac{\partial(\overline{\rho(\boldsymbol{Q})}\tilde{u}_i)}{\partial t}+\frac{\partial}{\partial x_j}(\rho(\widetilde{\boldsymbol{Q}})\tilde{u}_i\tilde{u}_j+\bar{p}\delta_{ij})+\frac{\partial}{\partial x_j}(\rho^{sgs}\tilde{u}_i\tilde{u}_j) = \frac{\partial\sigma_{ij}(\widetilde{\boldsymbol{Q}})}{\partial x_j}-\frac{\partial\tau_{ij}^{sgs}}{\partial x_j}+\frac{\partial\sigma_{ij}^{sgs}}{\partial x_j} \tag{2.46}$$

$$\frac{\partial(\overline{\rho(\boldsymbol{Q})}\widetilde{e_t(\boldsymbol{Q})})}{\partial t}+\frac{\partial}{\partial x_j}\left(\rho(\widetilde{\boldsymbol{Q}})\left(h(\widetilde{\boldsymbol{Q}})+\frac{\tilde{u}_i\tilde{u}_i}{2}\right)\tilde{u}_j\right)+\frac{\partial H^{sgs}\tilde{u}_j}{\partial x_j}+\frac{\partial}{\partial x_j}\left(\frac{\rho^{sgs}\tilde{u}_i\tilde{u}_i\tilde{u}_j}{2}\right) = \frac{\partial}{\partial x_j}\{q_j(\widetilde{\boldsymbol{Q}})+\tilde{u}_i\sigma_{ij}(\widetilde{\boldsymbol{Q}}))\}-\frac{\partial Q_j^{sgs}}{\partial x_j}-\frac{\partial\mathcal{J}_j^{sgs}}{\partial x_j}+\frac{\partial q_j^{sgs}}{\partial x_j}+\frac{\partial\mathcal{D}_j^{sgs}}{\partial x_j} \tag{2.47}$$

$$\frac{\partial\overline{\rho(\boldsymbol{Q})}\tilde{Y}_k}{\partial t}+\frac{\partial(\rho(\widetilde{\boldsymbol{Q}})\tilde{Y}_k\tilde{u}_j)}{\partial x_j}+\frac{\partial}{\partial x_j}(\rho^{sgs}\tilde{Y}_k\tilde{u}_j) = \frac{\partial J_{kj}(\widetilde{\boldsymbol{Q}})}{\partial x_j}-\frac{\partial\Phi_{kj}^{sgs}}{\partial x_j}+\frac{\partial J_{kj}^{sgs}}{\partial x_j}+\overline{\dot{\omega}_k(\boldsymbol{Q})} \tag{2.48}$$

The terms in blue font represent the conventional subgrid convective fluxes for which modeling approaches have been considered and are used in practice. Some of these approaches will be discussed in the next section. The terms in red represent the new set of subgrid terms that need further investigation to determine their significance and behavior. These terms will be the primary focal point in Chapters 4 and 5. The filtered reaction rate

$\overline{\dot{\omega}_k(\boldsymbol{Q})}$ presents a separate area of research in turbulent combustion modeling that has received significant focus in the community [68, 69, 141-144]. Hence, modeling of this term is not studied further in this dissertation.

It is recognized that the magnitudes of the spatial derivatives of the resolved and subgrid terms are more relevant in determining the flow evolution than the magnitudes of the terms themselves. The form of the filtered equations (2.45)-(2.48) provides a basis for *a priori* evaluation of different terms in the exact style in which they appear in the governing system.

2.4 Subgrid scale models for the conventional subgrid fluxes

The SGS terms for the convective fluxes are the primary source of non-linearity in the governing equation for thermodynamically simple flows. Consequently, they have received significant focus in the SGS modeling literature. Several modeling approaches have been developed, investigated, and refined through past efforts, and reasonable success has been achieved in modeling these SGS terms. While most of the models were initially developed for incompressible flows, they have been extended for compressible flows as well. In this section, we briefly describe some of the widely adopted subgrid models for the convective fluxes in compressible LES.

2.4.1 Dynamic Smagorinsky/eddy-diffusivity models

The Boussinesq eddy-viscosity hypothesis was adopted by Smagorinsky [50] for modeling the subgrid stresses τ_{ij}^{sgs}. Accordingly, the deviatoric part of the subgrid stress tensor is modeled in a form analogous to the viscous stress tensor

$$\tau_{ij}^{sgs,d} = \tau_{ij}^{sgs} - \frac{\delta_{ij}}{3}\tau_{kk}^{sgs} = \nu_t\left(\tilde{S}_{ij} - \frac{\delta_{ij}}{3}\tilde{S}_{kk}\right) \tag{2.49}$$

where $\tilde{S}_{ij}$ is the resolved strain rate tensor given as $\tilde{S}_{ij} = \frac{1}{2}\left(\frac{\partial \tilde{u}_i}{\partial x_j} + \frac{\partial \tilde{u}_j}{\partial x_i}\right)$ and $\left|\tilde{S}\right| = \left(2\tilde{S}_{ij}\tilde{S}_{ij}\right)^{1/2}$. ν_t represents the subgrid eddy viscosity and is modeled as the product of an appropriate length and velocity scales representing the subgrid turbulent fluctuations. In the Smagorinsky model [50], these characteristic scales are estimated in terms of the resolved strain rate $\bar{S}_{ij}$ and the local filter length scale (which is assumed to be equal to the local grid width). The model coefficient C_s was taken to be constant with a value suggested by Lilly [145] using equilibrium assumption in the inertial sub-range.

$$\nu_t = -2C_s\overline{\Delta}^2\left|\tilde{S}\right| \tag{2.50}$$

The trace of the stress tensor, which is twice the subgrid turbulent kinetic energy, is modeled by Yoshizawa [63] as

$$\tau_{kk}^{sgs} = -2C_I\overline{\Delta}^2\bar{\rho}\left|\tilde{S}\right|^2 \tag{2.51}$$

Limitations with the use of a constant model coefficient were addressed through the dynamic model approach [53, 146]. The model coefficients are determined as a function of the solution in space and time through Germano's identity [53]. This involves an additional level of filtering at a test filter scale $\widehat{\Delta}$ that is slightly larger than the grid filter scale. The subtest filter stresses are given as $T_{ij} = \widehat{\overline{\rho u_i u_j}} - \widehat{\overline{\rho u_i}}\,\widehat{\overline{\rho u_j}}/\hat{\bar{\rho}}$. The resolved turbulent stress (called the Leonard stress) is then expressed in terms of the turbulent stresses at the grid and test filter scales using Germano's identity.

$$\mathcal{L}_{ij} = T_{ij} - \hat{\tau}_{ij} = \left(\frac{\widehat{\overline{\rho u_i}\,\overline{\rho u_j}}}{\bar{\rho}}\right) - \frac{\widehat{\overline{\rho u_i}}\,\widehat{\overline{\rho u_j}}}{\hat{\bar{\rho}}} \tag{2.52}$$

Using the Smagorinsky model, the deviatoric component of $\mathcal{L}_{ij}$ can be expressed as

$$\mathcal{L}_{ij}^{d} = \mathcal{L}_{ij} - \frac{\delta_{ij}}{3}\mathcal{L}_{kk} = C_s \mathcal{M}_{ij}$$

where $\mathcal{M}_{ij} = -2\overline{\Delta}^2\left(\frac{\hat{\Delta}^2}{\Delta^2}\hat{\bar{\rho}}\left|\breve{\tilde{S}}\right|\left(\breve{\tilde{S}}_{ij} - \frac{\delta_{ij}}{3}\breve{\tilde{S}}_{kk}\right) - \widehat{\bar{\rho}\left|\breve{\tilde{S}}\right|\left(\breve{\tilde{S}}_{ij} - \frac{\delta_{ij}}{3}\breve{\tilde{S}}_{kk}\right)}\right)$

The $\breve{\tilde{(.)}}$ notation represents a Favre-filtered quantity at the test filter level. Finally, the model coefficient is determined by Lilly's least squares method [146] as

$$C_s = \frac{\langle \mathcal{L}_{ij}^{d}\mathcal{M}_{ij}\rangle}{\langle \mathcal{M}_{ij}\mathcal{M}_{ij}\rangle} \tag{2.53}$$

The angular brackets indicate spatial averaging in the homogeneous direction to avoid large unphysical oscillations of the model coefficient that can destabilize the numerical solution.

Subsequently, the approach has been extended for compressible flows including models for the subgrid heat flux and scalar fluxes [64]. The subgrid heat flux Q_j^{sgs} is modeled through a subgrid thermal conductivity that is computed in terms of the eddy viscosity and a SGS Prandtl number Pr_t. The model formulation can be given as,

$$Q_j^{sgs} = \overline{\rho h u_j} - \frac{\overline{\rho h}\,\overline{\rho u_j}}{\bar{\rho}} = \frac{-2C_s\overline{\Delta}^2\bar{\rho}\left|\tilde{S}\right|}{Pr_t}\frac{\partial \tilde{T}}{\partial x_j} \tag{2.54}$$

The SGS Prandtl number is computed through the dynamic model approach as

$$\frac{C_s}{Pr_t} = \frac{< \mathcal{L}_j{}^h \mathcal{M}_j{}^h >}{< \mathcal{M}_j{}^h \mathcal{M}_j{}^h >}$$

where

$$\mathcal{L}_j{}^h = \left(\frac{\widehat{\overline{\rho h}\,\overline{\rho u_j}}}{\bar{\rho}}\right) - \frac{\widehat{\overline{\rho h}}\,\widehat{\overline{\rho u_j}}}{\hat{\bar{\rho}}}$$

$$\mathcal{M}_j{}^h = -2\overline{\Delta}^2\left(\frac{\widehat{\Delta}^2}{\overline{\Delta}^2}\hat{\bar{\rho}}\left|\tilde{\tilde{S}}\right|\frac{\partial \tilde{\tilde{T}}}{\partial x_j} - \widehat{\bar{\rho}\left|\tilde{S}\right|\frac{\partial \tilde{T}}{\partial x_j}}\right)$$

Similarly, the subgrid diffusive flux are modeled with a subgrid species diffusivity in terms of a SGS Schmidt number as

$$\Phi_{kj}^{sgs} = \overline{\rho Y_k u_j} - \frac{\overline{\rho Y_k}\,\overline{\rho u_j}}{\bar{\rho}} = \frac{-2C_s\overline{\Delta}^2\bar{\rho}\left|\tilde{S}\right|}{Sc_{t,k}}\frac{\partial \tilde{Y}_k}{\partial x_j} \tag{2.55}$$

The SGS Schmidt numbers are computed as

$$\frac{C_s}{Sc_{t,k}} = \frac{\langle \mathcal{L}_j{}^k \mathcal{M}_j{}^k \rangle}{\langle \mathcal{M}_j{}^k \mathcal{M}_j{}^k \rangle}$$

$$\mathcal{L}_j^k = \left(\frac{\widehat{\overline{\rho Y_k}\,\overline{\rho u_j}}}{\bar{\rho}}\right) - \frac{\widehat{\overline{\rho Y_k}}\,\widehat{\overline{\rho u_j}}}{\hat{\bar{\rho}}}$$

$$\mathcal{M}_j{}^k = -2\overline{\Delta}^2\left(\frac{\widehat{\Delta}^2}{\overline{\Delta}^2}\hat{\bar{\rho}}\left|\breve{\tilde{S}}\right|\frac{\partial \breve{\tilde{Y}}_k}{\partial x_j} - \widehat{\bar{\rho}\left|\tilde{S}\right|\frac{\partial \tilde{Y}_k}{\partial x_j}}\right)$$

2.4.2 Dynamic mixed model

Mixed models are a class of models that combine a scale-similarity model with an eddy-diffusivity model. The scale-similarity model was originally proposed by Bardina et al. [66], and is based on the fractal nature of turbulence at the small scales. The scale-similarity hypothesis postulates that the structure of turbulence at subgrid scales is similar to those at the smallest resolved scales. The subgrid stress was modeled in terms of the filtered resolved velocity field. The scale-similarity model has been shown to yield significantly better correlation for the subgrid stresses but does not provide the required dissipation to the flow field. To alleviate this, the addition of an eddy-viscosity term was proposed yielding the mixed model. The mixed model can also be interpreted based on the Germano decomposition in Equation (2.33). The Leonard term can be computed directly

based on the resolved flow field and is identical to the scale-similarity model, while the Cross and Reynolds terms are modeled by the eddy-viscosity term.

The mixed model formulation for the subgrid stresses can be written as

$$\tau_{ij} - \frac{\delta_{ij}}{3}\tau_{kk} = A_{ij} - \frac{\delta_{ij}}{3}A_{kk} - 2C_m\overline{\Delta}^2\bar{\rho}\left|\tilde{S}\right|\left(\tilde{S}_{ij} - \frac{\delta_{ij}}{3}\tilde{S}_{kk}\right) \tag{2.56}$$

where $A_{ij} = \bar{\rho}\left(\widetilde{\tilde{u}_i\tilde{u}_j} - \tilde{\tilde{u}}_i\tilde{\tilde{u}}_j\right)$ is the scale similarity term, and C_m is the modified Smagorinsky model coefficient. The model coefficient value can either be prescribed with a constant value as done by Erlebacher et al. [65] for compressible simulations. Alternatively, these can be evaluated within a dynamic modeling framework. Following Germano's approach, Zang et al. [147] formulated a dynamic mixed model for incompressible flows. Vreman et al. [148] have made further refinements to this model and also extended the formulation for compressible flow applications [67]. In the dynamic mixed model, the model coefficient is given as

$$C_m = \frac{\langle\left(\mathcal{L}_{ij}^d - \mathcal{H}_{ij}^d\right)\mathcal{M}_{ij}\rangle}{\langle\mathcal{M}_{ij}\mathcal{M}_{ij}\rangle} \tag{2.57}$$

with $\mathcal{H}_{ij} = \hat{\bar{\rho}}\left(\widehat{\tilde{\tilde{u}}_i\tilde{\tilde{u}}_j} - \hat{\tilde{\tilde{u}}}_i\hat{\tilde{\tilde{u}}}_j\right) - \widehat{\bar{\rho}\left(\widetilde{\tilde{u}_i\tilde{u}_j} - \tilde{\tilde{u}}_i\tilde{\tilde{u}}_j\right)}$.

Similarly, the formulation for the subgrid heat flux is given as

$$Q_j = \bar{\rho}\left(\widetilde{\tilde{h}\tilde{u}_J} - \tilde{\tilde{h}}\tilde{\tilde{u}}_j\right) - \frac{2C_m\overline{\Delta}^2\bar{\rho}\left|\tilde{S}\right|}{Pr_t}\frac{\partial\tilde{T}}{\partial x_j} \tag{2.58}$$

$$\frac{C_s}{Pr_t} = \frac{\langle\left(\mathcal{L}_j{}^h - \mathcal{H}_j{}^h\right)\mathcal{M}_j{}^h\rangle}{\langle\mathcal{M}_j{}^h\mathcal{M}_j{}^h\rangle}$$

$$\mathcal{H}_j{}^h = \hat{\bar{\rho}}\left(\widetilde{\tilde{\tilde{h}}\tilde{\tilde{u}}_J} - \tilde{\tilde{\tilde{h}}}\tilde{\tilde{\tilde{u}}}_j\right) - \widehat{\bar{\rho}\left(\widetilde{\tilde{h}\tilde{u}_J} - \tilde{\tilde{h}}\tilde{\tilde{u}}_J\right)}$$

and the subgrid species fluxes are given as

$$\Phi_{kj}^{sgs} = \bar{\rho}\left(\widetilde{\tilde{Y}_k\tilde{u}_J} - \tilde{\tilde{Y}}_k\tilde{\tilde{u}}_j\right) - \frac{2C_m\overline{\Delta}^2\bar{\rho}\left|\tilde{S}\right|}{Sc_{t,k}}\frac{\partial\tilde{Y}_k}{\partial x_j} \tag{2.59}$$

$$\frac{C_s}{Sc_{t,k}} = \frac{\langle\left(\mathcal{L}_j{}^k - \mathcal{H}_j{}^k\right)\mathcal{M}_j{}^k\rangle}{\langle\mathcal{M}_j{}^k\mathcal{M}_j{}^k\rangle}$$

$$\mathcal{H}_j{}^k = \hat{\bar{\rho}}\left(\widetilde{\tilde{\tilde{Y}}_k\tilde{\tilde{u}}_J} - \tilde{\tilde{\tilde{Y}}}_k\tilde{\tilde{\tilde{u}}}_j\right) - \widehat{\bar{\rho}\left(\widetilde{\tilde{Y}_k\tilde{u}_J} - \tilde{\tilde{Y}}_k\tilde{\tilde{u}}_J\right)}$$

CHAPTER 3. COMPUTATIONAL FRAMEWORK FOR DIRECT NUMERICAL SIMULATIONS

3.1 Overview

This chapter describes the computational configuration, flow conditions, and numerical framework used to conduct the DNS simulations. DNS of a spatially evolving supercritical mixing layer constituted by methane and liquid oxygen (LOX) under both non-reacting mixing and reacting conditions are conducted. Study of flows at low Reynolds number, such as those reported in the majority of available literature [46, 98, 99, 103], does not furnish a complete understanding of the physics of small-scale motion due to the limited range of scales represented and lack of scale separation. The Reynolds number of the flow in this study is of the order of 10^4-10^5 which is representative of practical operating conditions. However, this would impose a large grid requirement for 3D DNS that can only be realized on large-scale computing systems which are limited at the time of this study. The computational complexity added by the thermodynamic and transport property evaluation scheme [116, 117] further inhibit realization of 3D DNS within an affordable cost and time. DNS is, therefore, limited to a two-dimensional setup in this study to achieve a flow configuration that is representative of practical systems with a tractable computational cost. Two-dimensional DNS of supercritical mixing and combustion at high Reynolds numbers have been investigated in some past studies [88, 149, 150]. Such studies allow a compromise between computational feasibility and realistic Reynolds number which is essential to understand modeling issues for practical applications. It is recognized that the flow structures and turbulence energy cascade in 2D DNS are different from that

of realistic 3D turbulent flows. Studies on compressible non-reacting and reacting mixing layers [80, 151] have compared *a priori* subgrid assessments from 2D and 3D DNS. These studies have reported that the conclusions obtained from either setting are comparable in spite of quantitative differences in the subgrid terms.

3.2 Problem description and computational framework

3.2.1 Flow configuration

For the baseline DNS study used to generate the database, a canonical transcritical/supercritical planar mixing layer configuration is considered. The mixing layer is constituted by LOX and gaseous methane streams that are initially co-flowing along a splitter plate as shown in Figure 3.1. This fundamental flow configuration is representative of many propulsion applications, such as fuel injectors. The computational domain and flow conditions are adopted from a previous study [152, 153] and chosen to represent conditions close to those of liquid rocket engine operation. Gaseous methane at 300 K is injected from the top of the splitter plate at a velocity of 60 m/s, while LOX at 120 K is injected from the bottom at a velocity of 10 m/s. The operating pressure is 100 bar, well above the critical pressures of methane, oxygen, and the resulting mixture at all compositions. The thickness of the splitter plate δ is 0.3 mm, comparable to the thickness of typical injectors employed in propulsion engines. A plate length of 1 mm is included to account for the effect of the boundary layer development before mixing occurs.

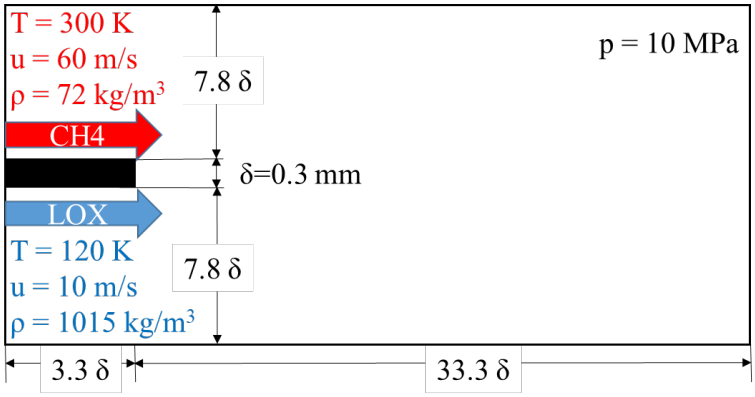

Figure 3.1 – Computational domain and flow conditions for the DNS study.

The computational domain spans a distance of 10 mm downstream from the trailing edge of the plate and 5 mm in the transverse direction. A mean velocity profile following a one-seventh power law superimposed with broadband fluctuations of 5% turbulence intensity is used to provide a fully developed turbulent boundary layer at the inlet for both incoming streams. No-slip boundary conditions are applied on the surfaces of the splitter plate. Outflow conditions are prescribed along the top, bottom and exit boundaries. The Reynolds number based on the LOX density and viscosity, splitter plate thickness, and velocity difference across the plate is about 1.5×10^5.

3.2.2 Grid resolution

A grid with a total of around 19 million cells is used for discretizing the present two-dimensional problem. The grid is finer in the mixing layer region with 2000 grid cells used in the transverse direction to discretize the 0.3 mm rim of the splitter plate. The grid is gradually stretched in the y-direction away from the mixing layer. The transverse grid spacing is also stretched in the downstream direction to capture the expected growth of the mixing layer and evolution of turbulent scales. To estimate the sufficiency of the grid

resolution for DNS, a maximum turbulent velocity of $u' = 10\, m/s$ in the recirculation zone downstream of the splitter plate is assumed. The turbulent Reynolds number based on the local flow properties is about 1.6×10^4 with respect to the methane and 2.7×10^4 to the oxygen inlet flow conditions. The latter is taken to be the maximum local Reynolds number for resolution considerations. The ratio of the largest to the smallest (Kolmogorov) length scales based on this Reynolds number is estimated to be $l_0/\eta = Re^{0.75} \approx 2000$. Considering the largest length scale to be of the order of magnitude of the plate thickness, $l_0 \approx 3 \times 10^{-4} m$, the order of magnitude of the Kolmogorov length scale is $\eta \approx 0.15\, \mu m$. The transverse grid spacing in the near field and along the center axis of the domain is about $0.15\, \mu m$. It should be noted that the values of local flow properties and turbulent velocities are conservative estimates. The local Reynolds number in reality would be at least one order of magnitude lower due to the low velocity in the recirculation region and reduction in density of oxygen caused by mixing. *A posteriori* estimates of the Kolmogorov scale was also computed from the DNS simulated flow field as $\eta_k = (\nu^3/\varepsilon)^{1/4}$, with the turbulent dissipation rate estimated as $\varepsilon = 2\nu S_{ij} S_{ij}$. The Kolmogorov scale estimates were found to be smallest in the core of the mixing layer with values in the order of 0.5-1 μm. The Prandtl number and Schmidt numbers estimated from the DNS flow field are in the range of 0.8-2.0 and 0.9-5.0 within the core of the mixing layer. The corresponding Batchelor scales $\eta_B = \eta_k (\mathrm{Pr}\ or\ Sc)^{-1/2}$ are also within the grid resolution considered. For the reacting case, the scales are further increased due to increased viscosity in the high-temperature flame regions. The spatial resolution in the mixing layer is, thus, deemed sufficient to resolve the entire range of turbulent length scales for both cases.

3.2.3 Theoretical framework and numerical schemes

The DNS simulation is conducted using an in-house CFD solver that has been developed and validated for fluid flows at all speeds and at all fluid thermodynamic states. The solver implements the theoretical framework described in Section 2.1. To circumvent the numerical stiffness arising from rapid flow property variations in the supercritical regime, a preconditioned solution approach is used [111, 112]. All the thermodynamic properties, including those occurring in the preconditioning matrix, are computed based on a unified treatment of general fluid thermodynamics derived directly from fundamental thermodynamic theories [27]. The Soave-Redlich-Kwong equation of state [115] is used and the thermodynamic and transport property evaluation scheme is as described in Section 2.1.3. The preconditioned formulation follows a primitive-variable approach and solves for the pressure and temperature as primary independent variables instead of density and internal energy. This eliminates the need for the laborious iterative procedure involved in solving for temperature from internal energy [112]. It also facilitates static load balance among computational blocks in a distributed computing environment. The resultant scheme is highly efficient and suitable for parallel computation.

The numerical framework is based on a finite-volume methodology, along with a dual time integration technique [111]. Temporal discretization is done using a second order backward difference scheme for the real-time integration, while the pseudo-time integration is performed with a four-stage Runge-Kutta scheme. For the real-time integration, a time step of $\Delta t = 20\ ns$ is imposed with upto 40 pseudo time integration steps within each real time step to ensure convergence of the pseudo time derivative. Spatial discretization is achieved using a fourth order, central-difference scheme in

generalized coordinates. A nine-point stencil is employed to evaluate the convective flux in each spatial direction to improve the spectral resolution of small-scale turbulence structures. Fourth-order matrix dissipation with a total-variation-diminishing switch developed by Swanson and Turkel [154] is applied to ensure numerical stability and minimize oscillations in regions with steep property variations.

Finally, a multi-block domain decomposition technique is employed to facilitate the implementation of parallel computing with message passing interfaces (MPI) at the domain boundaries. The parallelization methodology is robust, and the speedup is almost linear. The theoretical and numerical scheme used is well established and has been applied to a variety of numerical studies of multi-scale, multi-physics problems in the context of supercritical fluid and combustion dynamics [155], including the vaporization, mixing, and combustion of liquid droplets under supercritical conditions [156, 157], cryogenic fluid injection [89, 158], and mixing and combustion in both shear coaxial and swirl injectors [90, 93, 159].

3.3 Combustion modeling approach for the reacting case

The computational configuration, grid discretization, and numerical framework for the reacting DNS are identical to those employed in the non-reacting study. For the reacting case, the Reynolds number is lowered in the mixing layer due to thermal expansion caused by heat release and the consequent reduction in density and increase in gas viscosity. The spatial resolution in the mixing layer is, thus, considered sufficient to resolve the entire range of turbulent length scales for both cases.

DNS of turbulent combustion involves the solution of appropriate chemistry mechanisms, often containing tens or hundreds of chemical species and reaction steps. These reaction processes and the governing conservation equations are to be solved on a grid that is sufficiently fine to resolve the length and time scales associated with the turbulence and flame. For high pressure combustion, added computational costs are incurred for the evaluation of real-fluid thermodynamic and transport properties which scales with the number of species N as $\mathcal{O}(N^2)$ or greater according to the mixing rules. The computation of real-fluid properties could constitute over 50% of the total computational time depending on the number of species [116, 117]. For reacting flows with multi-species transport and detailed chemical kinetics, the computations associated with finite-rate kinetics would further increase the computational complexity by an order of magnitude depending on the number of species and the reaction mechanism used to represent the chemical processes. Given these considerations, DNS of high-pressure combustion with finite-rate chemical kinetics is computationally prohibitive for realistic flow configurations unless some simplifications are made.

To circumvent this problem, the flamelet approximation is used in this study to model the combustion process. A fundamental assumption of the flamelet model is that the reaction processes are infinitely fast compared to the fluid dynamic processes. The turbulent flame is therefore considered to behave as an aggregate of locally one-dimensional laminar flames that are convected by the turbulent flow structures. The idea is to decouple the solution of the turbulent flow field from the solution of chemistry and solve for the evolution of chemical species in the mixture fraction space [160]. The flamelet concept is believed to be valid when the Karlovitz number is smaller than 100 [143]. The

Karlovitz number is defined as the ratio between the chemical time scale to the smallest Kolmogorov time scale.

$$Ka = \frac{t_f}{t_\eta} \tag{3.1}$$

In other words, the flamelet assumption holds when the time scales of the flame are much smaller than the Kolmogorov scales. The characteristic time scale of the flame can be estimated as [143]

$$t_f = \frac{f_{st}^2(1 - f_{st})^2}{\chi_q} \tag{3.2}$$

where f_{st} is the stoichiometric mixture fraction. For the methane-oxygen mixture considered in this study, $f_{st} = 0.2$. The extinction (quenching) scalar dissipation rate χ_q can be obtained from solutions of counterflow diffusion flames of oxygen and methane at the given operating conditions. The value is estimated to be $3.6 \times 10^5 s^{-1}$ at the stoichiometric condition at 10 MPa [161]. This gives a flame time scale of $7.1 \times 10^{-8} s$. The Kolmogorov time scale t_η, calculated from the Reynolds number, integral length scale, and reference velocity, is estimated to be of the order of $10^{-6} - 10^{-7} s$. The resulting Karlovitz number is thus of the order of $10^{-1} - 10^{-2}$, and the flamelet assumption is justified for the flow configuration considered in this study.

The flame thickness of a non-premixed flame depends on the pressure and strain rate. The maximum strain rate in the current configuration for the non-reacting flow is found to be $6 \times 10^5 s^{-1}$. The corresponding laminar flame thickness is about 20 μm, based

on the half maximum width of temperature [162, 163]. The mesh resolution in the flame zone is of the order of 1 μm, which is much smaller than the flame thickness. Thus, all the relevant turbulent and flame scales are resolved directly. The coupling of flamelet-based models with DNS simulations have been considered in previous works [164-166] to overcome the computational challenges associated with detailed chemical kinetics. Mukhopadhyay et al. [167] have shown that coarse DNS combined with a filtered flamelet approach can reproduce the resolved DNS results if the grid size is of the order of the flame thickness. The grid employed in this study is already fine enough to fully resolve the flame thickness, and therefore a filtered approach is not necessary and the laminar flamelet solution is used directly to represent the chemistry at each cell.

The flamelet model implemented in this study uses pre-computed laminar flamelet solution obtained from simulations of one-dimensional counterflow diffusion flames that incorporates real-fluid thermodynamics and validated chemical kinetics [161, 162]. The oxygen/methane chemistry is modeled based on the reduced chemical mechanism of Sung et al. [168, 169]. The solutions are tabulated in a look-up table that is given as input to the CFD solver. The mixture fraction (f) and scalar dissipation rate (χ) are used as input parameters, to obtain the species composition from the table at each time step. The flamelet solutions are only tabulated at a reference pressure corresponding to the prespecified operating condition. This is a reasonable assumption since pressure fluctuations in the flow are within 1% of the reference pressure. For the DNS simulation, the conservation equation for the mixture fraction is given as:

$$\frac{\partial \rho f}{\partial t} + \frac{\partial \rho u_j f}{\partial x_j} = \frac{\partial}{\partial x_j}\left(\rho D \frac{\partial f}{\partial x_j}\right) \tag{3.3}$$

The scalar dissipation rate is computed as

$$\chi = 2D\left(\frac{\partial f}{\partial x_j}\right)^2 \tag{3.4}$$

where the diffusivity D is estimated from the mixture thermal conductivity with the assumption of unity Lewis number. Accounting for real-fluid mass diffusivities of individual species could be important in determining the flame characteristics [170], but is reserved for future studies. It is emphasized here that the primary focus of this study is to investigate inconsistencies associated with LES filtering and subgrid modeling at supercritical conditions. The flamelet model offers a computational balance to obtain a representative, fully resolved, multi-species reacting flowfield upon which the LES modeling issues can be analyzed.

3.4 Filtering procedure for *a priori* evaluation

The resolved terms and the associated subgrid terms in the LES formulation described in Section 2.3.5 are computed exactly from the DNS database through explicit spatial filtering employing a box filter. The filtering is performed in the computational space which offers some advantages. The filter width in the computational space is kept homogenous. As a result, the filter operator is commutative with the spatial derivatives in the computational space [132, 133]. A constant filter width in computational space also

renders a non-uniform LES grid in the physical space which preserves the same grid stretching as the DNS. This is desirable since it provides a direct examination of the LES formulation on grid topologies that are applied in practical non-homogeneous flows.

The filtered quantities are represented on a grid which is coarser than the DNS grid by a factor Δ_f. The filter width factor Δ_f is defined as the ratio between the local LES cell size to the corresponding DNS cell size in the computational space.

$$\Delta_f = \frac{\Delta_{LES}}{\Delta_{DNS}} \tag{3.5}$$

Three values of Δ_f are chosen – 2, 5, and 10 to represent fine, moderate, and coarse resolution LES grids. Based on the LES grid defined in the computational space, the filtered quantities are computed by evaluating the discrete box filter defined in Equation (2.16). For the evaluation of spatial derivatives, the corresponding derivatives are computed in the computational space using second order central difference schemes and then transformed to the physical space using the transformation metrics of the LES grid. With this methodology, the evaluated spatial derivatives based on the filtered variables are consistent with the filtered spatial variables since the commutation is valid in the uniform computational space. There still remain residual errors that are isolated and within the order of accuracy of the filtered grid metrics [133]. These residual errors are to be treated along with the numerical discretization errors and are not considered in this study.

CHAPTER 4. NON-REACTING BINARY-SPECIES MIXING STUDIES

4.1 Overview

This chapter presents a systematic examination of the terms in the LES formulation for the non-reacting, binary-species turbulent mixing case. The primary objective is to quantify the complete set of terms in the filtered conservations equations for LES derived in Chapter 2 and assess the validity of the currently employed LES simplifications. In particular, the relevance and significance of the new set of subgrid terms identified in Section 2.3.5 are evaluated to determine the need to model these terms.

A global order of magnitude analysis is performed to reveal the relevance of different subgrid terms with respect to the leading order terms in the governing equations. The differences between Favre-filtered and Reynolds-filtered variables are investigated. The modeling errors associated with the computation of the filtered thermodynamic and transport coefficients using resolved Favre-filtered quantities are also quantified. The analyses are done at different filter widths to provide insights to modeling requirements for LES at different resolutions.

4.2 Flow field description

Instantaneous visualizations of the flowfield are shown in Figure 4.1 in terms of distributions of density, mixture fraction, magnitude of second derivative of density

(shadowgraph) and vorticity magnitude. No distinct interface is observed between the liquid oxygen and methane stream, as the surface tension and enthalpy of vaporization are close to zero across the critical mixing temperature. Strong vortices develop due to the velocity difference, and stringy, finger-like structures appear along the liquid oxygen stream. The mixing layer behaviour is similar to classical variable-density fluid mixing, as observed in the experiments of Chehroudi et al. [9].

Another important observation from the density and shadowgraph images is the rapid variation of density and resulting steep density gradients across the mixing layer. The large density gradient regions that are a characteristic feature of transcritical and supercritical mixing are highlighted in the shadowgraph visualizations. As the LOX stream, which is initially at a subcritical temperature of 120K, meets the warmer gaseous methane stream downstream of the splitter plate, its temperature increases. The oxygen stream subsequently goes through a transcritical regime, where thermodynamic and transport properties are known to be very sensitive to changes in pressure and temperature, resulting in strong variations of these quantities. For illustration, the transverse variations of density and specific heat across the mixing layer is shown in Figure 4.2. This feature imposes a strict resolution requirement for accurately resolving the flow variations, especially at the smallest turbulent scales.

The DNS database captures the complete spatio-temporal evolution of the inhomogeneous flow field and provides rich information that is lacking in previous studies that employed temporal flow configurations with periodic boundaries. Figure 4.3 shows the flow evolution through instantaneous snapshots of density at various time instants. The spatial and temporal motions of the fine turbulent scales are captured in very high detail.

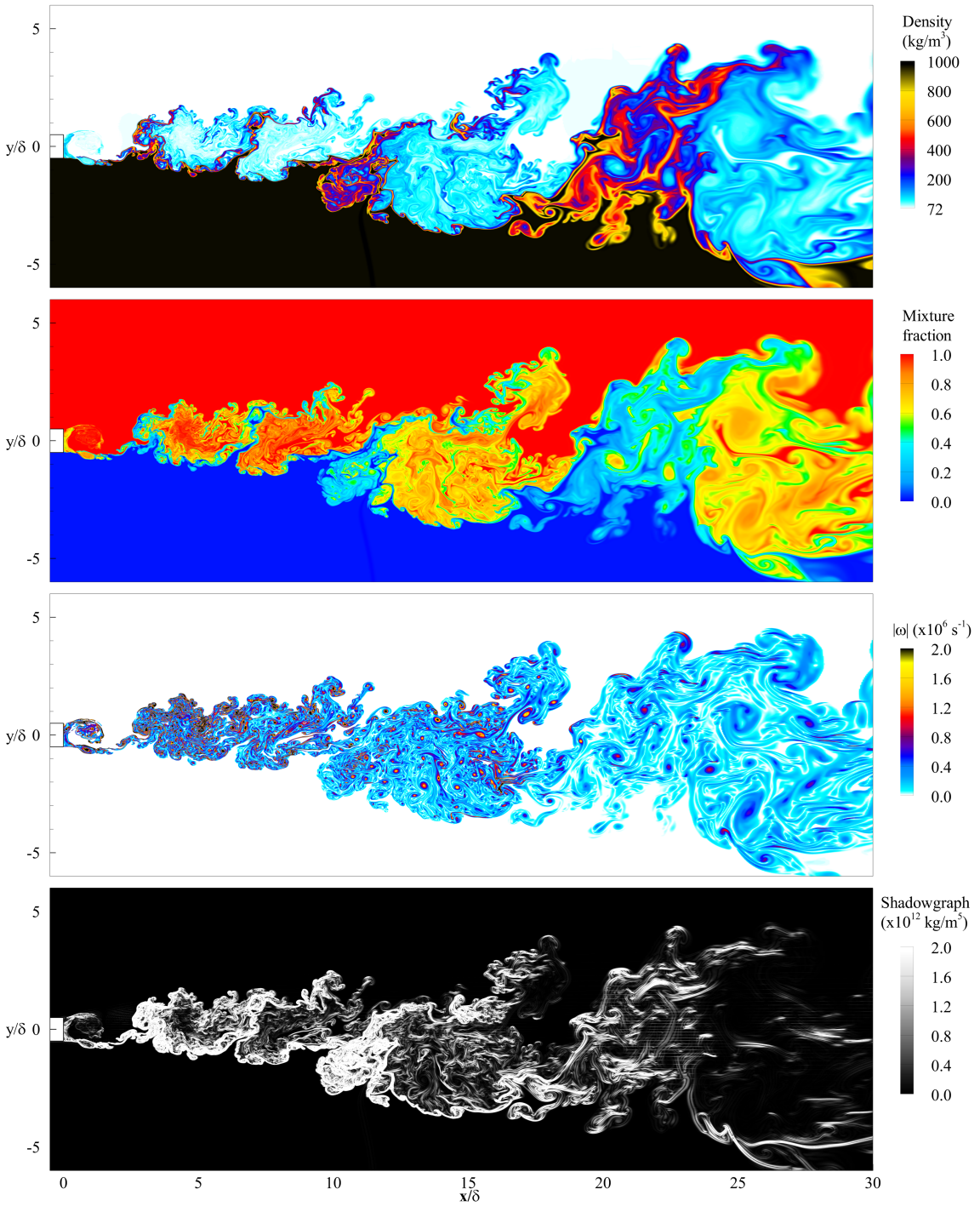

Figure 4.1 – Instantaneous visualizations of the non-reacting flow field: distributions of density, mixture fraction, vorticity magnitude and second derivative of density (shadowgraph image) (from top to bottom).

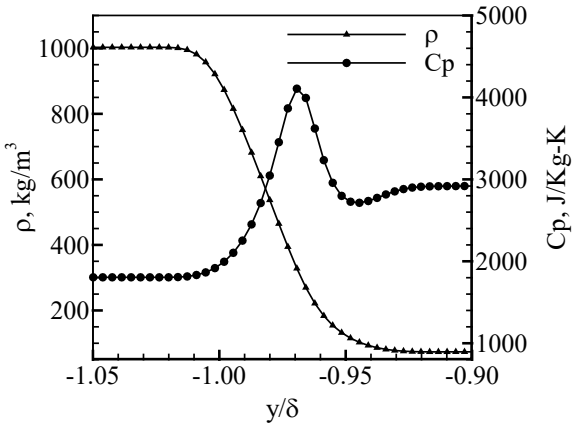

Figure 4.2 – Transverse variation of density and specific heat across the mixing layer.

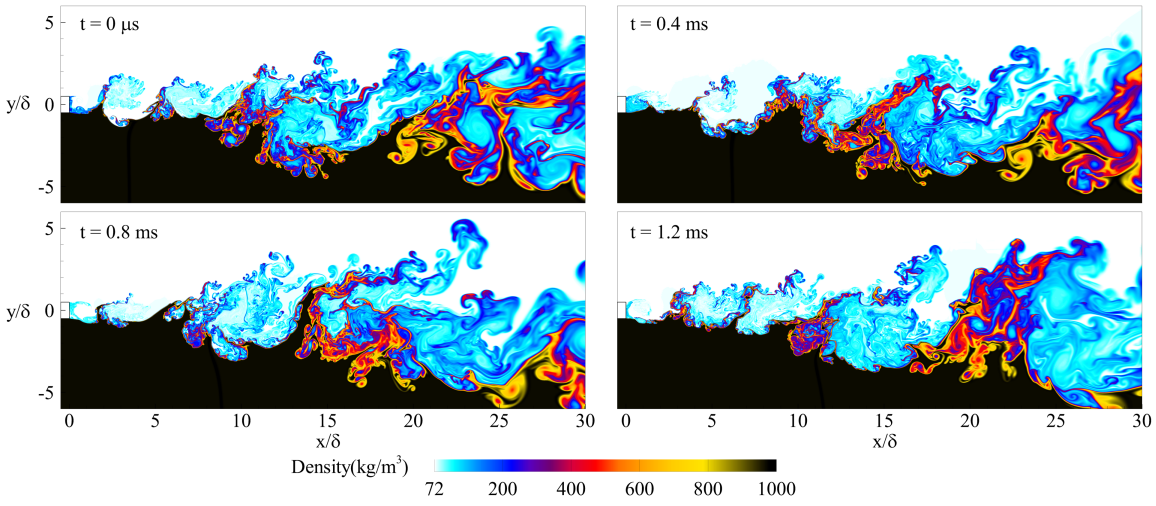

Figure 4.3 – Spatio-temporal evolution of the density field at various time instants.

4.3 Order of magnitude analysis of terms in the filtered equations

To assess the significance of terms in the governing filtered equations, the order of magnitude of each term is quantified. The terms are considered in the same spatial

derivative form as they appear in the governing equations to provide a true understanding of their contributions. The L^2 norms of the terms computed within the core of the mixing layer field is used as the metric for the analysis. The L^2 norms are normalized by the total number of cells over which the norms are computed. The L^2 norms and L^∞ norms computed over the entire flowfield were also evaluated for comparison and the trends were found to be identical. Global L^2 norms have been used to quantify the order of magnitudes of terms in several past studies [99, 100, 171]. The distributions of resolved terms and their subgrid terms are found to follow a similar trend with maximum and minimum values in the same regions. Therefore, the use of a global metric is considered reasonable for obtaining a preliminary overall understanding of the contribution of different terms. In addition to the global magnitudes, the spatial distributions of the terms are also of interest since the flow is inhomogeneous. These distributions are also analyzed for each conservation equation. The new subgrid terms associated with the diffusive fluxes and thermodynamic quantities that are introduced in this work are of particular interest. The relative magnitudes of these terms with respect to their corresponding resolved term is presented to understand their relevance.

The analyses are carried out for three different filter widths. The filter width factor is defined as the ratio between the local LES filter (grid) width and the DNS grid width $\Delta_f = \Delta_{LES}/\Delta_{DNS}$. Filter width factors of 2, 5 and 10 are chosen to represent fine, moderate, and coarse resolution LES. Note that the filter width factors should be interpreted in the computational space where the filtering is defined rather than the physical space where the local DNS and LES filter sizes are non-uniform.

4.3.1 Total mass conservation equation

The order of magnitude of terms in the filtered total mass conservation equation are presented in Table 4.1. It is seen that the residual mass flux terms associated with the subgrid density are two orders of magnitude lower than the resolved mass flux terms at Δ_f = 2. It may possibly be acceptable to neglect these terms at this resolution and retain only the resolved terms. However, this must be strictly justified with *a posteriori* analyses to evaluate the effect of neglecting this term even though it is small. With increase in filter width, the magnitudes of the resolved terms decrease while those of the residual terms increase. The amount of subgrid contributions increases with filter width in general. In the continuity equation the resolved and residual terms represent the convective mass fluxes occurring at the resolved and subgrid scales respectively. As the filter width is increased, the convective flux at the subgrid level increases, leading to increased magnitude of the residual terms. As a result, the residual terms become increasingly significant with respect to the corresponding resolved term. For example, the order of magnitude of the mass flux in the streamwise direction $(\partial \rho^{sgs} \tilde{u}/\partial x)$ is about 1% compared to the corresponding resolved term $\left(\partial \rho(\widetilde{\boldsymbol{Q}})\tilde{u}/\partial x\right)$ at Δ_f = 2 and increases to about 8.5% at Δ_f = 10. The contribution of the transverse flux is slightly higher because of larger gradients in the transverse direction.

Table 4.1 – Order of magnitude of terms in the filtered continuity equation at different filter widths (non-reacting), unit: x10^8 kg $m^{-3}s^{-1}$.

Δ_f	$\frac{\partial}{\partial x}(\rho(\widetilde{\boldsymbol{Q}})\tilde{u})$	$\frac{\partial}{\partial y}(\rho(\widetilde{\boldsymbol{Q}})\tilde{v})$	$\frac{\partial}{\partial x}(\rho^{sgs}\tilde{u})$	$\frac{\partial}{\partial y}(\rho^{sgs}\tilde{v})$
2	2.07	1.39	2.27e-2	6.18e-2
5	1.59	1.20	6.11e-2	1.09e-1
10	1.06	0.92	9.06e-2	1.39e-1

To derive a detailed understanding of the distribution of the residual terms, the relative magnitude of the residual fluxes are computed as the ratio between the instantaneous residual flux term and the corresponding resolved flux term at each LES cell. The distribution is shown in Figure 4.4. The trend of increasing relative magnitude of the residual contributions with filter width is observed. The relative magnitudes are more significant than those interpreted from the L^2 norms. The peak magnitudes are around 4% for the finest resolution and increases above 20% for the coarsest resolution. In fact, there are localized regions where the relative magnitude is as high as 40%. The regions where the residual fluxes attain significance are closely correlated with the interface between the pure LOX stream and the mixing layer core. In these regions, large variations of density occur as a result of transition from transcritical LOX to a supercritical mixture. Considering the relevance of the residual terms, it is deemed important to account for and model the subgrid density or equivalently the filtered density especially at coarser grid resolutions.

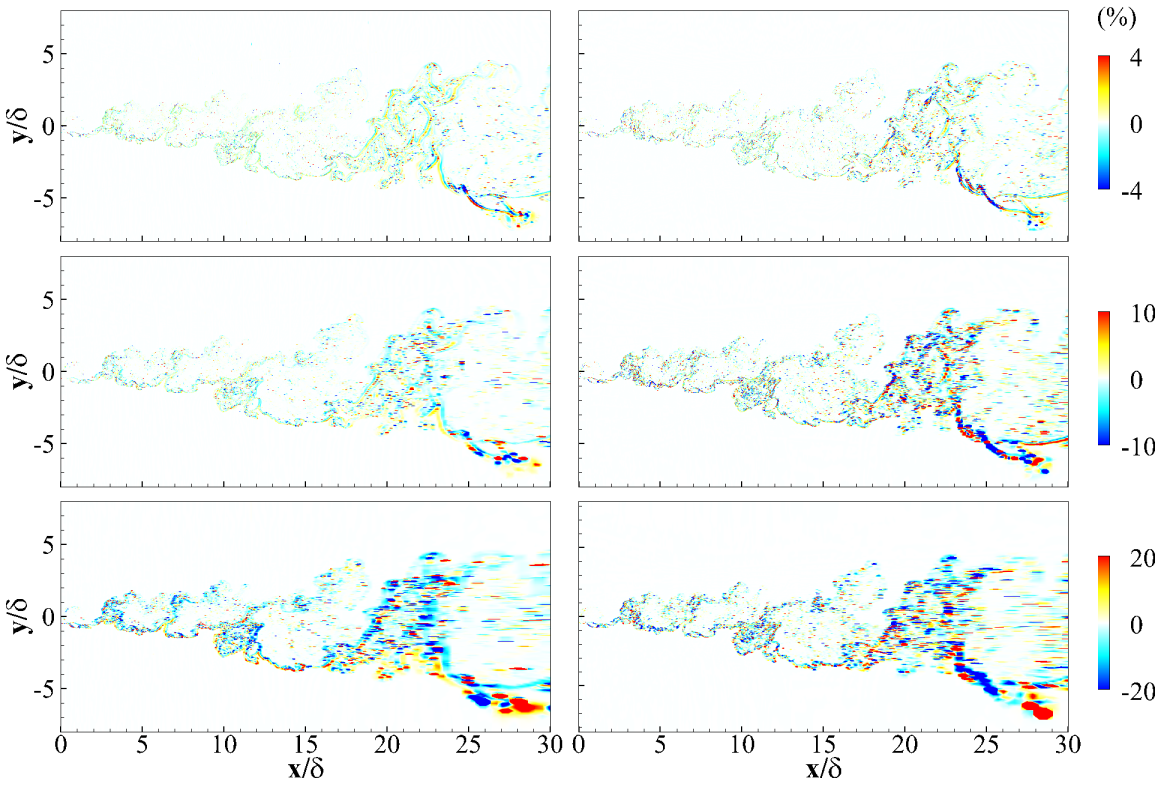

Figure 4.4 – Relative magnitude of residual flux terms in the filtered continuity equation at different filter widths (row-wise) (non-reacting). x-derivative flux (left) and y-derivative flux (right).

4.3.2 Momentum conservation equations

The order of magnitude of the terms in the filtered x- and y-momentum conservation equations are presented in Table 4.2 and Table 4.3 respectively. The convective flux terms, pressure gradient, and the conventional subgrid convective fluxes are the leading order terms, which is expected in high Reynolds number flows. Similar to the continuity equation, the magnitudes of the resolved convective flux terms decrease while the magnitudes of the subgrid conventional flux terms increase with filter width. An interesting observation is that the residual convective flux terms associated with the subgrid

density are one magnitude higher than the conventional subgrid fluxes. The magnitudes of these residual terms also increase with filter width. At Δ_f = 5 and 10 they are comparable in magnitude to the pressure gradient terms particularly in the x-momentum equation. This re-emphasizes the need for accurate representation of the filtered density.

The resolved viscous fluxes are about 4 orders of magnitude lower than the convective fluxes, compliant with the Reynolds number of the flow. The subgrid viscous fluxes are one order of magnitude lower than the viscous fluxes for Δ_f = 2. The resolved viscous fluxes decrease in magnitude with increasing filter width, while their subgrid contributions remain roughly same. At Δ_f = 10, the subgrid viscous flux contributions are comparable in magnitude to the resolved viscous fluxes. It is not clear to what extent these terms would affect the accuracy of the equation. One argument that can be made is that the resolved viscous fluxes must be considered in the equation even though they are much lower in magnitude compared to the convective fluxes and pressure gradient terms. Therefore, the subgrid viscous fluxes which are comparable in magnitude must also be accounted for. The viscous forces originate at the molecular level and therefore act primarily at small scales. In that sense, it is potentially important to account for these subgrid effects to accurately model the viscous dissipation.

In a recent study on temporal mixing layers by Ovais et al. [171], the subgrid viscous flux was found to be one to two orders of magnitude smaller than the resolved flux. Their Reynolds number was of the order of 600. This underscores the need to consider realistic Reynolds numbers for subgrid modeling investigations.

The relative magnitude of the residual flux terms associated with the subgrid density in the u-momentum equation are presented in Figure 4.5. The trend is similar to that observed for the residual terms in the continuity equation. The magnitude of the terms become significant with respect to the resolved convective fluxes as the filter width is increased. At Δ_f = 10, the magnitudes of the terms reach upto 20-40% of the resolved convective fluxes and must be accounted. Figure 4.6 shows the relative magnitude of the subgrid viscous fluxes with the corresponding resolved viscous fluxes. The trend is different from that observed in Figure 4.5. Unlike the subgrid terms associated with the subgrid density which peak in the LOX interface of the mixing layer, the subgrid viscous fluxes are significant within the entire core of the mixing layer. This can be attributed to the intense turbulent mixing and continuous variation in mixture composition and molecular viscosity/viscous fluxes at the subgrid level. These subgrid effects are not captured within the resolved viscous fluxes that are computed purely based on the resolved field variables. These effects gain significance with increased filter width as more variations occur at the subgrid level. The peak values of the subgrid viscous fluxes are higher than the resolved viscous fluxes in some cells implying that the viscous effects are incorrectly captured if the subgrid contributions are not considered.

Table 4.2 – Order of magnitude of terms in the filtered x-momentum equation at different filter widths (non-reacting), unit: x10^8 kg $m^{-2}s^{-2}$.

Δ_f	$\frac{\partial}{\partial x}(\rho(\widetilde{\boldsymbol{Q}})\tilde{u}\tilde{u})$	$\frac{\partial}{\partial y}(\rho(\widetilde{\boldsymbol{Q}})\tilde{u}\tilde{v})$	$\frac{\partial \tau_{xx}^{sgs}}{\partial x}$	$\frac{\partial \tau_{xy}^{sgs}}{\partial y}$
2	79.71	31.06	4.29e-2	6.07e-2
5	61.49	26.58	1.67e-1	2.98e-1
10	40.12	20.19	3.44e-1	5.66e-1

Δ_f	$\frac{\partial \bar{p}}{\partial x}$	$\frac{\partial}{\partial x}(\rho^{sgs}\tilde{u}\tilde{u})$	$\frac{\partial}{\partial y}(\rho^{sgs}\tilde{u}\tilde{v})$
2	3.94	0.68	0.38
5	3.75	1.89	1.40
10	3.45	2.87	2.22

Δ_f	$\frac{\partial \sigma_{xx}(\widetilde{\boldsymbol{Q}})}{\partial x}$	$\frac{\partial \sigma_{xy}(\widetilde{\boldsymbol{Q}})}{\partial y}$	$\frac{\partial \sigma_{xx}^{sgs}}{\partial x}$	$\frac{\partial \sigma_{xy}^{sgs}}{\partial y}$
2	1.21e-2	7.68e-2	1.48e-3	7.38e-3
5	6.60e-3	4.75e-2	2.26e-3	1.17e-2
10	3.20e-3	2.70e-3	2.07e-3	9.24e-3

Table 4.3 – Order of magnitude of terms in the filtered y-momentum equation at different filter widths (non-reacting), unit: x10^8 kg $m^{-2}s^{-2}$.

Δ_f	$\frac{\partial}{\partial x}(\rho(\widetilde{\boldsymbol{Q}})\tilde{u}\tilde{v})$	$\frac{\partial}{\partial y}(\rho(\widetilde{\boldsymbol{Q}})\tilde{v}\tilde{v})$	$\frac{\partial \tau_{xy}^{sgs}}{\partial x}$	$\frac{\partial \tau_{yy}^{sgs}}{\partial y}$
2	22.03	20.24	3.74e-2	5.98e-2
5	17.23	17.46	1.32e-1	3.04e-1
10	12.06	13.25	2.37e-1	6.47e-1

Δ_f	$\frac{\partial \bar{p}}{\partial y}$	$\frac{\partial}{\partial x}(\rho^{sgs}\tilde{u}\tilde{v})$	$\frac{\partial}{\partial y}(\rho^{sgs}\tilde{v}\tilde{v})$
2	3.74	0.19	0.51
5	3.68	0.53	1.20
10	3.57	0.79	1.65

Δ_f	$\frac{\partial \sigma_{xy}(\widetilde{\boldsymbol{Q}})}{\partial x}$	$\frac{\partial \sigma_{yy}(\widetilde{\boldsymbol{Q}})}{\partial y}$	$\frac{\partial \sigma_{xy}^{sgs}}{\partial x}$	$\frac{\partial \sigma_{yy}^{sgs}}{\partial y}$
2	1.29e-2	2.90e-2	2.15e-3	7.85e-3
5	7.52e-3	1.88e-2	3.33e-3	6.63e-3
10	4.00e-3	1.08e-2	3.12e-3	6.55e-3

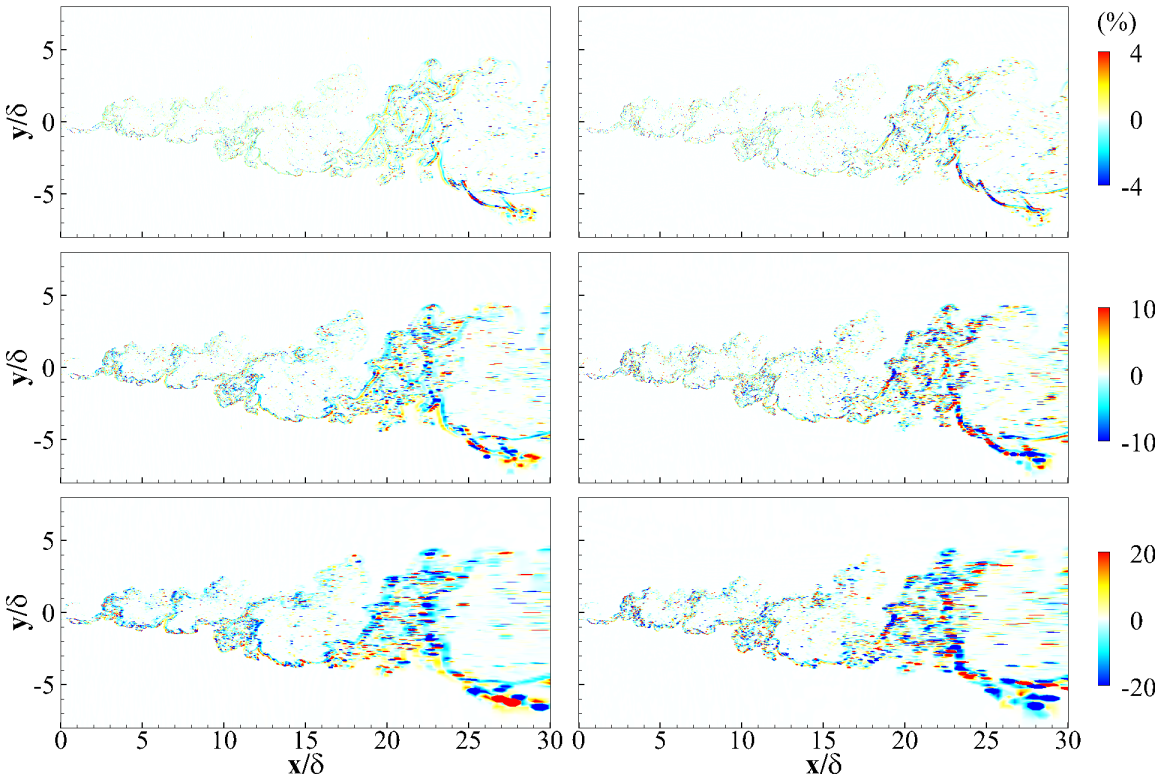

Figure 4.5 – Relative magnitude of residual convective flux terms associated with the subgrid density in the filtered x-momentum equation at different filter widths (row-wise) (non-reacting). x-derivative flux (left) and y-derivative flux (right).

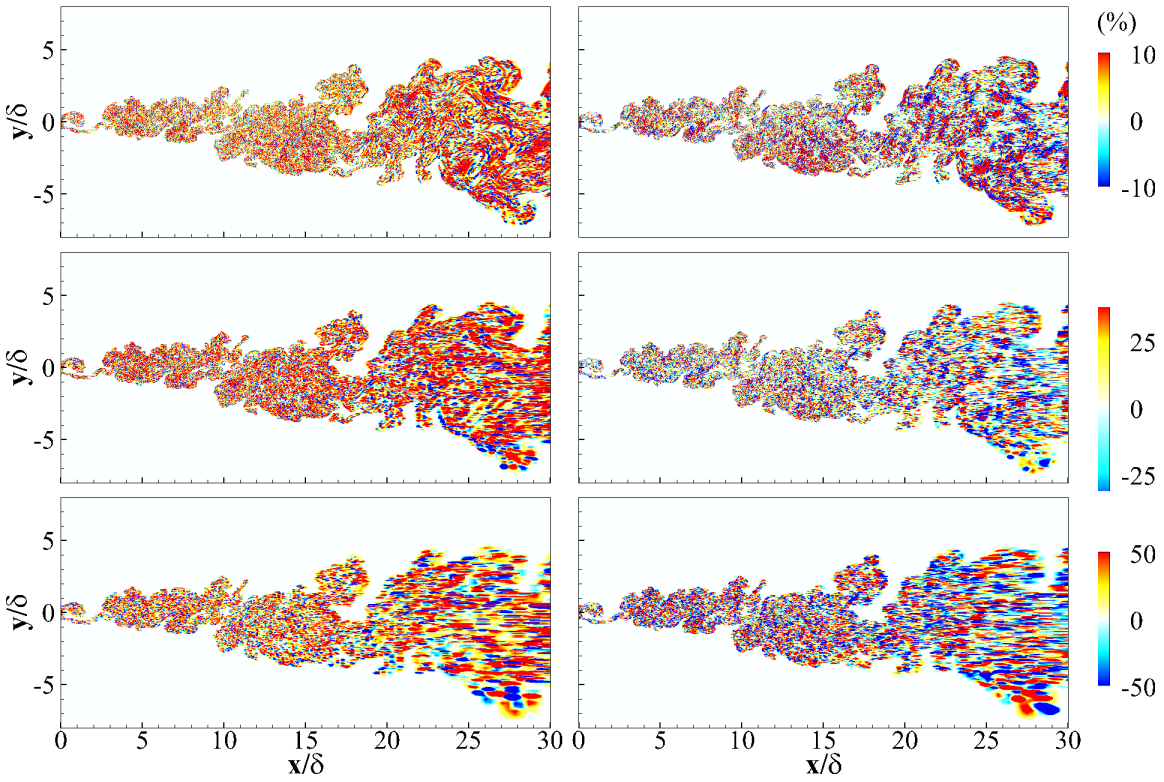

Figure 4.6 – Relative magnitude of subgrid viscous flux terms in the filtered x-momentum equation at different filter widths (row-wise) (non-reacting). x-derivative flux (left) and y-derivative flux (right).

4.3.3 Total energy conservation equation

The orders of magnitude of the terms in the filtered energy equation as a function of filter width is presented in Table 4.4. The resolved convective enthalpy fluxes are the leading order terms. The conventional subgrid enthalpy fluxes are two orders of magnitude lower at $\Delta_f = 2$. The magnitudes of the resolved enthalpy fluxes decrease, while those of the subgrid enthalpy fluxes increase with increasing filter width. Another set of terms of significance with respect to the convective fluxes are the residual terms involving H^{sgs} arising from the filtered product of the density and enthalpy. The magnitudes of these

terms are comparable and slightly larger than the subgrid enthalpy flux, and the magnitudes increase with filter width. These terms rank second in the order of magnitude of all terms in the energy equation and therefore neglecting this term in the filtered equation is not reasonable.

The contributions from the kinetic energy fluxes are 3-4 orders of magnitude smaller than the enthalpy fluxes. The contributions from the subgrid turbulent diffusive fluxes $\mathcal{J}_x^{sgs}$ are even smaller by about two orders of magnitude compared to the corresponding resolved kinetic energy fluxes. Similarly, the residual kinetic energy flux terms associated with the subgrid density are also about two orders of magnitude lower than the resolved kinetic energy fluxes. The magnitudes of these terms increase with filter width but remain much lower compared to other leading terms. Thus, neglecting these terms could be justifiable at these flow conditions. The residual kinetic energy flux terms associated with the subgrid density could easily be accounted if the filtered density is modeled correctly.

The next set of terms of importance are the diffusive heat flux terms. These terms appear larger in magnitude than the resolved kinetic energy fluxes, particularly the flux term in the y-direction owing to the larger transverse thermal and scalar stratifications. The contributions from the corresponding subgrid diffusive heat fluxes q_j^{sgs} are only one order of magnitude smaller than the resolved counterparts at $\Delta_f = 2$ but become comparable in magnitude at $\Delta_f = 10$ due to decrease in magnitude of the resolved heat fluxes.

The viscous diffusion terms are the lowest in magnitude compared to all the other terms. The resolved contributions from these terms are 6-7 orders of magnitude smaller

than the leading order terms, and the corresponding subgrid contributions are one order of magnitude smaller than the resolved components. Even though the subgrid viscous diffusion terms are significant with respect to the corresponding resolved viscous diffusion, the overall magnitude of these terms with respect to the other terms suggest that neglecting subgrid contributions in these terms might not have a considerable impact for modeling, atleast at similar conditions.

Figure 4.7 and Figure 4.8 show the distribution of the magnitude of the subgrid convective flux associated with the subgrid enthalpy H^{sgs} and the subgrid diffusive heat flux q_j^{sgs}, scaled relative to their corresponding instantaneous resolved flux terms. The trends are quite similar to those observed for the counterpart terms in the momentum equations.

Table 4.4 – Order of magnitude of terms in the filtered energy equation at different filter widths (non-reacting), unit: x10^{12} kg m^{-1}s^{-3}.

Δ_f	$\frac{\partial}{\partial x}(\rho(\widetilde{\boldsymbol{Q}})h(\widetilde{\boldsymbol{Q}})\tilde{u})$	$\frac{\partial}{\partial y}(\rho(\widetilde{\boldsymbol{Q}})h(\widetilde{\boldsymbol{Q}})\tilde{v})$	$\frac{\partial Q_x^{sgs}}{\partial x}$	$\frac{\partial Q_y^{sgs}}{\partial y}$
2	135.21	109.10	1.16	1.60
5	102.69	95.17	3.87	6.18
10	72.88	78.00	6.46	10.28

Table 4.4 continued

Δ_f	$\frac{\partial}{\partial x}(\rho(\widetilde{\boldsymbol{Q}})\tilde{u}_i\tilde{u}_i\tilde{u})$	$\frac{\partial}{\partial y}(\rho(\widetilde{\boldsymbol{Q}})\tilde{u}_i\tilde{u}_i\tilde{v})$	$\frac{\partial \mathcal{J}_x^{sgs}}{\partial x}$	$\frac{\partial \mathcal{J}_y^{sgs}}{\partial y}$
2	2.15e-1	7.88e-2	2.40e-4	3.02e-4
5	1.65e-1	6.68e-2	8.55e-4	1.52e-3
10	1.07e-1	5.00e-2	1.93e-3	2.84e-3

Δ_f	$\frac{\partial H^{sgs}\tilde{u}}{\partial x}$	$\frac{\partial H^{sgs}\tilde{v}}{\partial x}$	$\frac{\partial}{\partial x}(\rho^{sgs}\tilde{u}_i\tilde{u}_i\tilde{u})$	$\frac{\partial}{\partial y}(\rho^{sgs}\tilde{u}_i\tilde{u}_i\tilde{v})$
2	3.17	8.47	1.51e-3	7.65e-4
5	8.31	14.93	4.20e-3	2.70e-3
10	11.65	18.69	6.53e-3	4.30e-3

Δ_f	$\frac{\partial q_x(\widetilde{\boldsymbol{Q}})}{\partial x}$	$\frac{\partial q_y(\widetilde{\boldsymbol{Q}})}{\partial y}$	$\frac{\partial q_x^{sgs}}{\partial x}$	$\frac{\partial q_y^{sgs}}{\partial y}$
2	3.16e-1	2.87	7.68e-2	8.38e-1
5	1.70e-1	1.52	6.50e-2	7.62e-1
10	4.11e-2	0.71	3.51e-2	4.47e-1

Table 4.4 continued

Δ_f	$\frac{\partial}{\partial x}\left(\tilde{u}\sigma_{xx}(\tilde{\boldsymbol{Q}}) + \tilde{v}\sigma_{xy}(\tilde{\boldsymbol{Q}})\right)$	$\frac{\partial}{\partial y}\left(\tilde{u}\sigma_{xy}(\tilde{\boldsymbol{Q}}) + \tilde{v}\sigma_{yy}(\tilde{\boldsymbol{Q}})\right)$	$\frac{\partial \mathcal{D}_x^{sgs}}{\partial x}$	$\frac{\partial \mathcal{D}_y^{sgs}}{\partial y}$
2	4.14e-5	2.41e-4	3.90e-6	2.23e-5
5	2.25e-5	1.56e-4	6.38e-6	3.68e-5
10	9.82e-6	7.99e-5	6.46e-6	3.10e-5

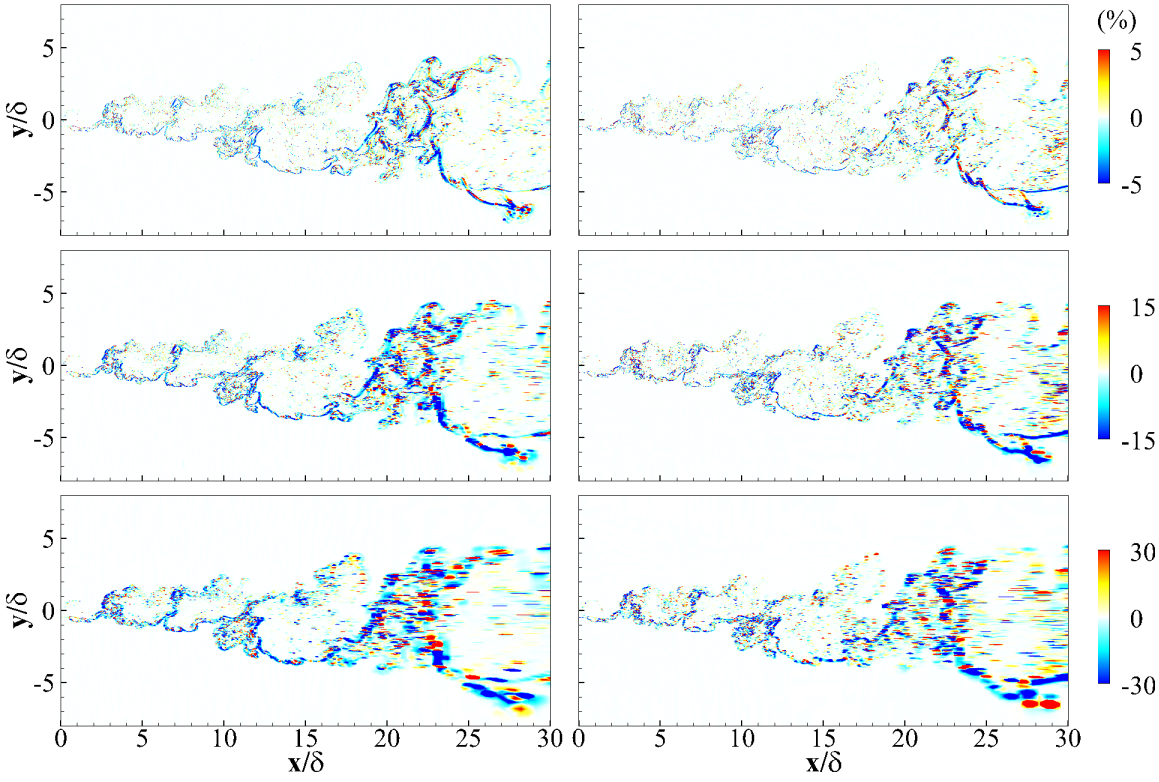

Figure 4.7 – Relative magnitude of residual convective flux terms associated with the subgrid enthalpy in the filtered energy equation at different filter widths (row-wise) (non-reacting). x-derivative flux (left) and y-derivative flux (right).

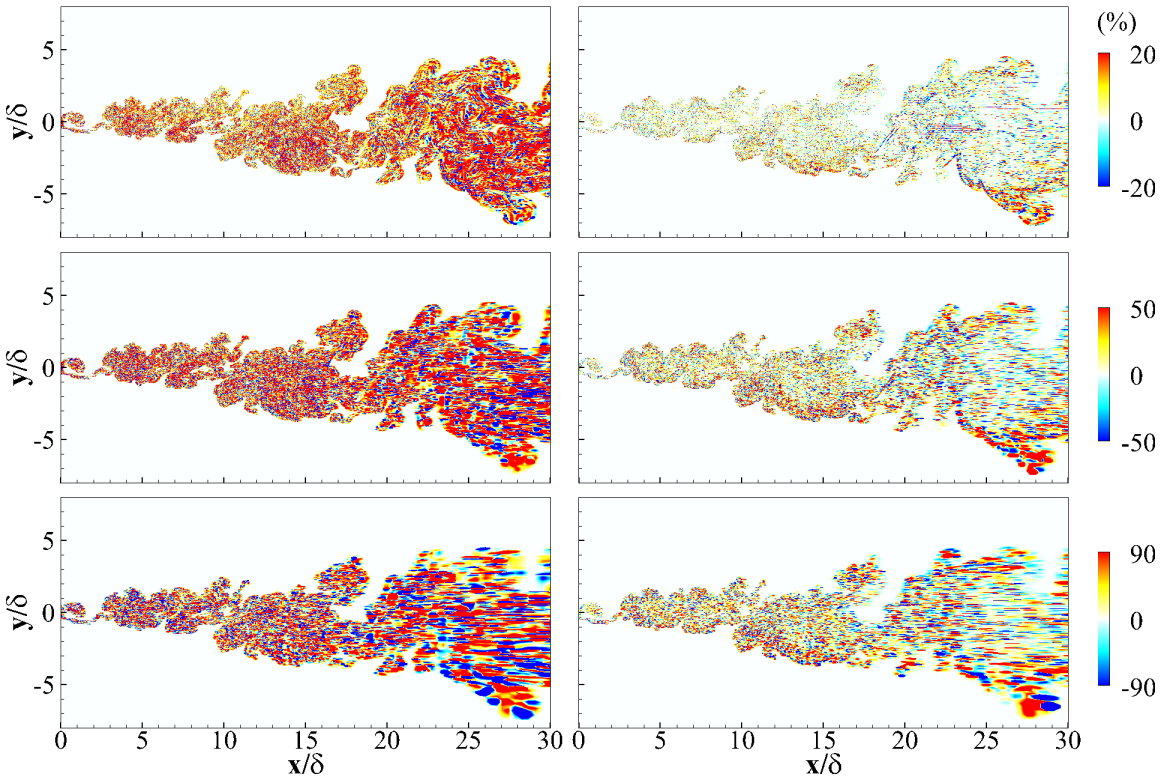

Figure 4.8 – Relative magnitude of subgrid diffusive heat flux terms in the filtered energy equation at different filter widths (row-wise) (non-reacting). x-derivative flux (left) and y-derivative flux (right).

4.3.4 Species mass conservation equations

The order of magnitude of terms in the filtered mass conservation equations for the CH_4 and O_2 species are shown in Table 4.5 and Table 4.6 respectively. The trends observed in both equations are similar with minor differences. The resolved species convective fluxes are the leading order terms in both equations. The magnitudes of the resolved convective flux terms for O_2 are one order higher due to the larger variation of density associated with oxygen. The subgrid species convective fluxes are of similar magnitude for both species and increase with filter width. For CH_4, the magnitudes of the subgrid

species convective fluxes are around 1% of the resolved convective fluxes at $\Delta_f = 2$ and increases to about 10-15% at $\Delta_f = 10$. For O_2, the contribution of subgrid species convective fluxes increase from around 0.2% to 2%. The residual species flux associated with the subgrid density are higher than the subgrid species fluxes, especially in the O_2 transport equation where the residual fluxes are one order of magnitude higher than the corresponding subgrid species fluxes. This once again highlights the need for an accurate modeling of the filtered density through the filtered equation of state and accounting for necessary subgrid effects in the filtered equation of state.

The resolved species diffusive fluxes are three and four orders of magnitude lower than the leading resolved convective fluxes in the CH_4 and O_2 equations respectively. The corresponding subgrid diffusive fluxes are smaller by one order of magnitude with respect to the resolved diffusive fluxes with increasing relative significance at higher filter widths.

The distributions of the relative magnitude of the subgrid convective fluxes associated with the subgrid density and the subgrid diffusive fluxes with respect to their resolved counterparts are shown in Figure 4.9 and Figure 4.10 respectively. The overall trends are similar to those of the equivalent terms in the momentum and energy equations. However, the relative magnitudes of the subgrid diffusive flux terms are much higher by almost a factor of 2 and are even greater than the resolved diffusive fluxes in certain regions at higher filter widths. Accounting for this term is considered important from a modeling perspective. The species diffusive fluxes also play an important role in modeling the subgrid mixing of species which is essential for combustion applications.

Table 4.5 – Order of magnitude of terms in the filtered CH_4 species mass conservation equation at different filter widths (non-reacting), unit: x10^7 kg $m^{-3}s^{-1}$.

Δ_f	$\frac{\partial}{\partial x}(\rho(\widetilde{\boldsymbol{Q}})\tilde{Y}_{CH4}\tilde{u})$	$\frac{\partial}{\partial y}(\rho(\widetilde{\boldsymbol{Q}})\tilde{Y}_{CH4}\tilde{v})$	$\frac{\partial \Phi_{CH4,x}^{sgs}}{\partial x}$	$\frac{\partial \Phi_{CH4,y}^{sgs}}{\partial y}$
2	2.67	2.23	2.48e-2	3.62e-2
5	1.98	1.94	8.26e-2	1.40e-1
10	1.38	1.57	1.37e-1	2.33e-1

Δ_f	$\frac{\partial}{\partial x}(\rho^{sgs}\tilde{Y}_{CH4}\tilde{u})$	$\frac{\partial}{\partial y}(\rho^{sgs}\tilde{Y}_{CH4}\tilde{v})$
2	5.07e-2	1.36e-1
5	1.32e-1	2.41e-1
10	1.82e-1	3.00e-1

Δ_f	$\frac{\partial}{\partial x}J_{CH4,x}(\widetilde{\boldsymbol{Q}})$	$\frac{\partial}{\partial y}J_{CH4,y}(\widetilde{\boldsymbol{Q}})$	$\frac{\partial}{\partial x}J_{CH4,x}^{sgs}$	$\frac{\partial}{\partial x}J_{CH4,y}^{sgs}$
2	6.22e-3	5.64e-2	1.51e-3	1.64e-2
5	2.29e-3	2.98e-2	1.28e-3	1.50e-2
10	8.00e-4	1.38e-2	6.92e-3	8.81e-3

Table 4.6 – Order of magnitude of terms in the O_2 species mass conservation equation at different filter widths (non-reacting), unit: x10^7 kg $m^{-3}s^{-1}$.

Δ_f	$\frac{\partial}{\partial x}(\rho(\widetilde{\boldsymbol{Q}})\tilde{Y}_{O2}\tilde{u})$	$\frac{\partial}{\partial y}(\rho(\widetilde{\boldsymbol{Q}})\tilde{Y}_{O2}\tilde{v})$	$\frac{\partial \Phi_{O2,x}^{sgs}}{\partial x}$	$\frac{\partial \Phi_{O2,y}^{sgs}}{\partial y}$
2	21.08	14.24	2.83e-2	3.62e-2
5	16.17	12.19	7.73e-2	1.40e-1
10	10.75	9.28	1.10e-1	2.33e-1

Δ_f	$\frac{\partial}{\partial x}(\rho^{sgs}\tilde{Y}_{O2}\tilde{u})$	$\frac{\partial}{\partial y}(\rho^{sgs}\tilde{Y}_{O2}\tilde{v})$
2	1.81e-1	4.97e-1
5	4.92e-1	8.92e-1
10	7.46e-1	1.14

Δ_f	$\frac{\partial}{\partial x}J_{O2,x}(\widetilde{\boldsymbol{Q}})$	$\frac{\partial}{\partial y}J_{O2,y}(\widetilde{\boldsymbol{Q}})$	$\frac{\partial}{\partial x}J_{O2,x}^{sgs}$	$\frac{\partial}{\partial x}J_{O2,y}^{sgs}$
2	3.12e-3	2.83e-2	7.60e-4	8.24e-3
5	1.15e-3	1.50e-2	6.41e-4	7.53e-3
10	4.02e-4	6.94e-3	3.47e-4	4.42e-3

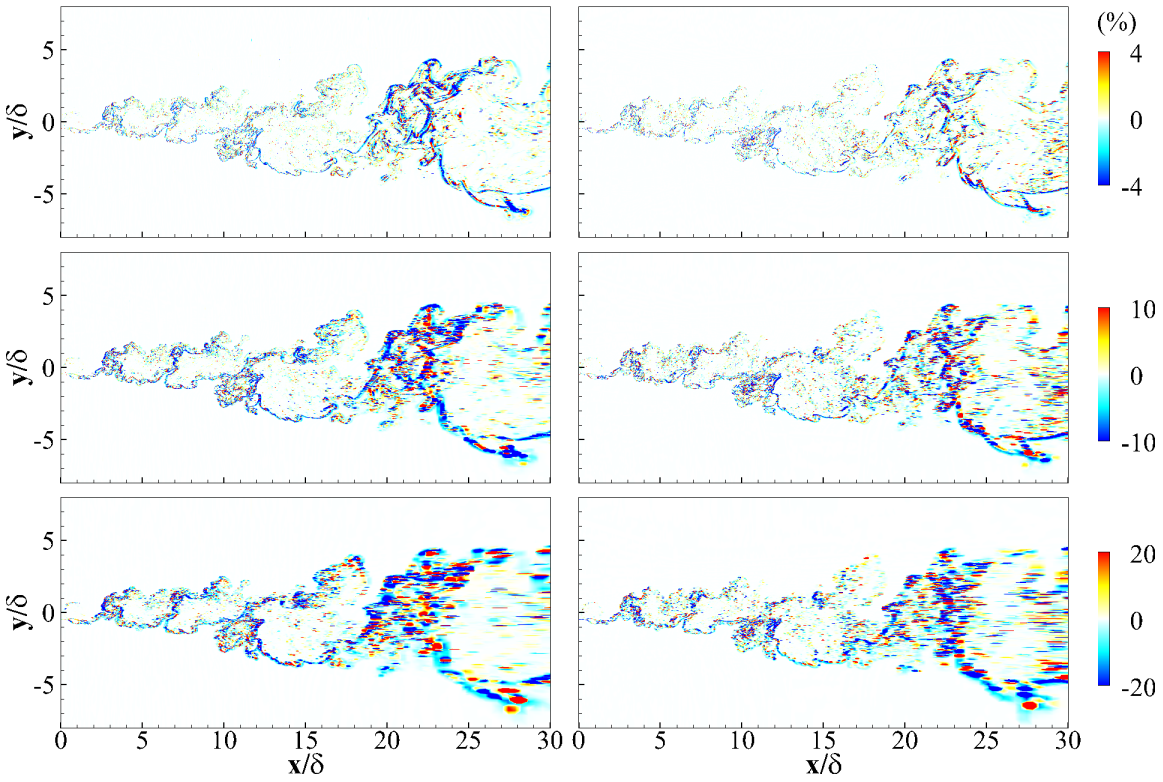

Figure 4.9 – Relative magnitude of residual convective flux terms associated with the subgrid density in the filtered CH_4 species conservation equation at different filter widths (row-wise) (non-reacting). x-derivative flux (left) and y-derivative flux (right).

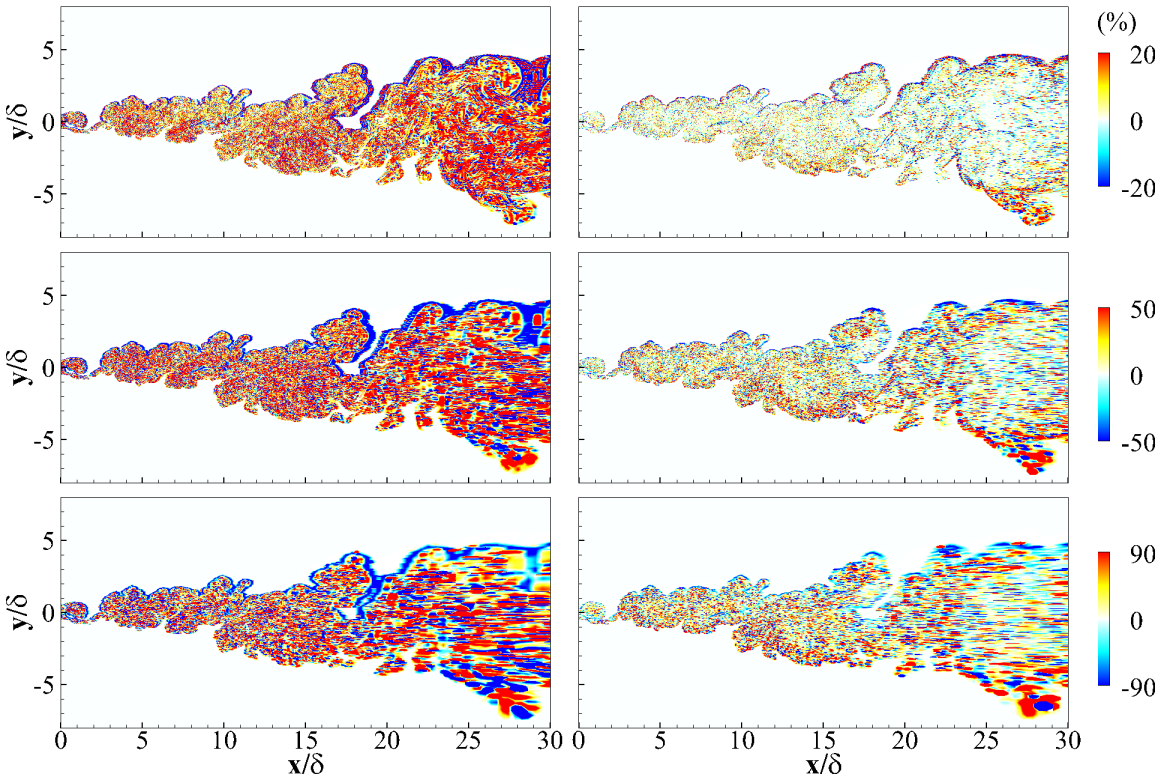

Figure 4.10 – Relative magnitude of subgrid species diffusive flux terms in the filtered CH_4 species conservation equation at different filter widths (row-wise) (non-reacting). x-derivative flux (left) and y-derivative flux (right).

4.4 Differences between Favre- and Reynolds-filtered variables

In most LES formalisms, Favre-filtered variables are considered within the theoretical framework for the velocities, temperature (or enthalpy) and the species mass fractions. This definition was introduced to simplify the mathematical structure of the filtered equations for compressible flows, and to avoid the introduction of additional residual terms for the time derivative terms that would require closure. Favre-filtering is a density-weighted filtering operator. As a result, a Favre-filtered quantity is biased towards the corresponding values of the quantity of the denser species based on the distribution at

the subgrid level. This issue might not be so serious for weakly compressible flows with low subgrid density variations. However, for flows with strong small-scale density stratifications and/or gradients, Favre-filtered quantities are expected to differ vastly from the corresponding Reynolds-filtered quantities. This applies for supercritical turbulent mixing flows which are characterized by large density gradients at different length scales.

In LES, Favre-filtered variables are used to compute the resolved flow quantities such as the viscous stresses, diffusive fluxes, and all thermodynamic and transport properties. In the previous section, it was revealed that the subgrid diffusive fluxes are of considerable magnitude. In Section 2.3.4, a decomposition of the subgrid diffusive fluxes was introduced that showed contributions resulting from the differences between Favre- and Reynolds-filtered variables, and the corresponding errors accrued due to computation of thermodynamic and transport properties. It is therefore important to quantify the differences between Favre-filtered and Reynolds-filtered primitive variables as a first step to understand the major contributions to the subgrid diffusive fluxes.

Figure 4.11 presents the comparison between Favre-filtered (y-axis) and Reynolds-filtered (x-axis) velocity (row 1), temperature (row 2) and CH_4 mass fraction (row 3) at different filter widths (column wise). The difference between Favre-filtered and Reynolds-filtered velocities are minimal, even though slight differences become noticeable with increasing filter width. The reason that the differences are negligible could be due to the weak correlation between density and velocity. Within the mixing layer, the velocity mixing happens much more rapidly than the scalar mixing as a result of which the velocities between the two species components are indistinguishable at the subgrid level. Therefore, the density-weighting has no impact on the filtered velocities. On the other hand, the

differences between the Favre-filtered and Reynolds-filtered temperature and species mass fractions are considerable, and the differences become more significant with increasing filter width. This can be attributed to the fact that the density, temperature, and mixture composition are strongly coupled through the non-linear equation of state. Moreover, the impeded scalar mixing at high pressures results in a non-uniform distribution of temperature and species mass fractions at the subgrid level. As a result, the Favre-filtered temperature and species mass fractions are biased towards those of the denser species within the subgrid mixture, i.e., O_2. The corresponding state values for O_2 are lower than those of CH_4. This is the reason why the Favre-filtered temperature and CH_4 mass fraction are underpredicted. The mass fraction of O_2 would be overpredicted for the same reason. Figure 4.12 quantifies the relative difference between the Favre-filtered and Reynolds-filtered temperature and CH_4 mass fractions at different filter widths. The relative difference for a primitive variable is defined as

$$\varepsilon_{\boldsymbol{Q}} = \frac{\bar{\boldsymbol{Q}} - \tilde{\boldsymbol{Q}}}{\bar{\boldsymbol{Q}}} \tag{4.1}$$

The relative difference in filtered temperature is mostly within 3-5% at $\Delta_f = 2$, although the errors are higher in some cells. With increasing filter width, the errors increase and peak errors about 10-15% or more are observed at $\Delta_f = 10$. The relative error in species mass fraction follows a similar trend with respect to increasing filter width. However, the relative error in mass fraction is almost 2-3 times higher than those for temperature. This could be a contributing factor for the increased significance of the subgrid diffusive fluxes

through the residual term $J_{kj}^{sgs(2)}$ arising from the difference between the Favre- and Reynolds-filtered mass fractions.

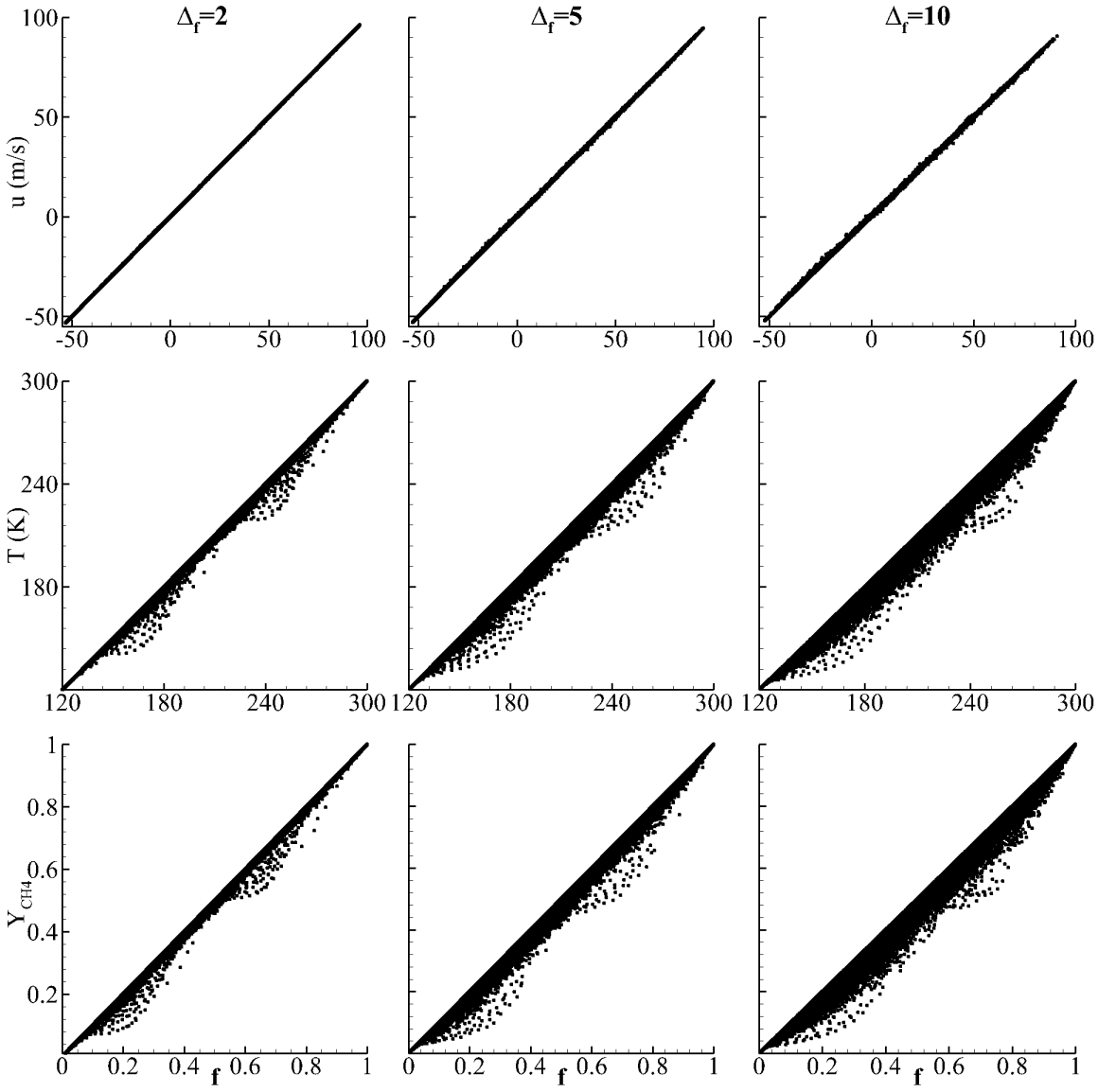

Figure 4.11 – Comparison between Reynolds-filtered (x-axis) and corresponding Favre-filtered state variables (y-axis) at different filter widths (non-reacting).

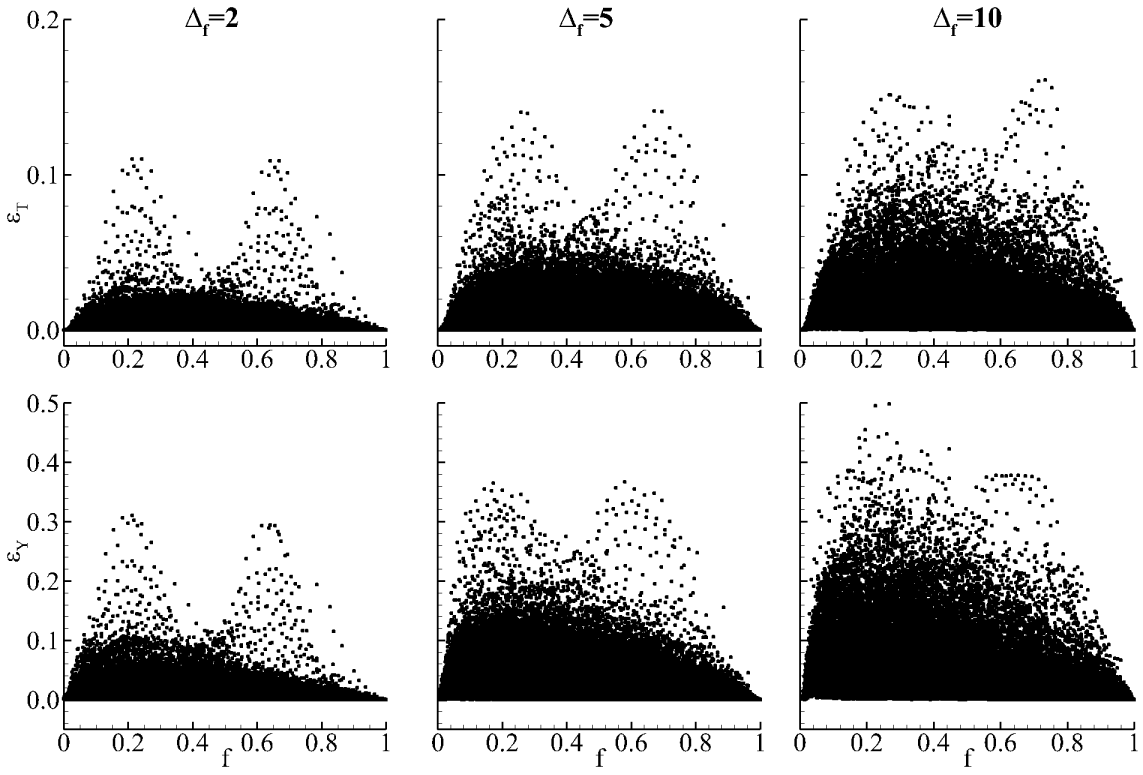

Figure 4.12 – Relative difference between Reynolds-filtered and Favre-filtered state variables at different filter widths as a function of mixture fraction (non-reacting).

4.5 Error in representation of filtered thermodynamic and transport properties

In current LES formalisms, the filtered thermodynamic and transport coefficients are represented as their values computed through the state relations using the Favre-filtered temperature and species mass fractions. The omission of subgrid correlations within the non-linear thermodynamic and transport property evaluation schemes, and the differences between the Favre-filtered and Reynolds-filtered quantities are expected to have ramifications for the represented filtered quantity. The resulting deviations contribute to the additional subgrid terms as discussed in Section 2.3.4.

Figure 4.13 and Figure 4.14 show the distributions of relative errors in the representation of different filtered thermodynamic and transport coefficients. The transport coefficients are considered in the form in which they appear in the governing terms. For example, in the diffusive flux term ρD_k is relevant than D_k itself. Similarly, in the energy equation ρh and $\rho h_k D_k$ quantities are relevant. The relative error of a secondary quantity $\phi(\boldsymbol{Q})$ is defined in terms of the difference between the exact filtered quantity and the corresponding term represented in terms of the Favre-filtered state variables.

$$\varepsilon_\phi = \frac{\overline{\phi(\boldsymbol{Q})} - \phi(\widetilde{\boldsymbol{Q}})}{\overline{\phi(\boldsymbol{Q})}} \tag{4.2}$$

The relative error in filtered density is mostly within 10% at Δ_f = 2 and increases with filter width showing around 20-40% peak errors at Δ_f = 10. The error is mostly negative implying that the density computed using the Favre-filtered temperature and species mass fractions overpredicts the true filtered density. This can be explained by the choice of Favre-filtered state variables. The temperature and mixture composition states of the local mixture are biased to those of O_2. This causes the computed density to be biased to that of O_2, which being higher results in overprediction of the filtered density. Note also that the density is a monotonically decreasing as a function of the mixture fraction and temperature for this case. In contrast, the behavior is slightly different for the dynamic viscosity and thermal conductivity, which are non-monotonic functions of temperature within the range of temperatures considered. These quantities decrease with temperature in the liquid-like state and increase with temperature in the gas-like state. The error distributions of these properties exhibit both positive and negative values in different

regions and the magnitudes of the error are relatively lower within 5-10%. In general, the computed properties are complex functions of the instantaneous species concentrations, temperature, and pressure, and the individual species properties. It is not easy to obtain a monotonic error distribution for certain quantities. The overall magnitudes of the errors of all properties, however, increase with filter width.

The specific enthalpy and species diffusivity of oxygen are much lower than that of methane, and the corresponding filtered values are also under-estimated. However, the overall trend for the transport coefficients that are considered in Figure 4.14 namely ρD_{CH4}, ρh and $\rho h_{CH4} D_{CH4}$ depend on the combined trend of both density and the other properties and the associated correlations among the properties. The error distributions of ρh closely follow the trend of density errors, even though the trend of enthalpy is completely opposite (see for reference [153]). The error distribution of the ρD_{CH4} shows significant errors with peak errors as high as 30-50% at the larger filter widths. This is considered an important contributor to the increased significance of the subgrid species diffusive fluxes. The trend of the errors in the $\rho h_{CH4} D_{CH4}$ quantity is more complex owing to different behaviors of the three individual properties. The errors of this quantity are also high, like the ρD_{CH4} quantity.

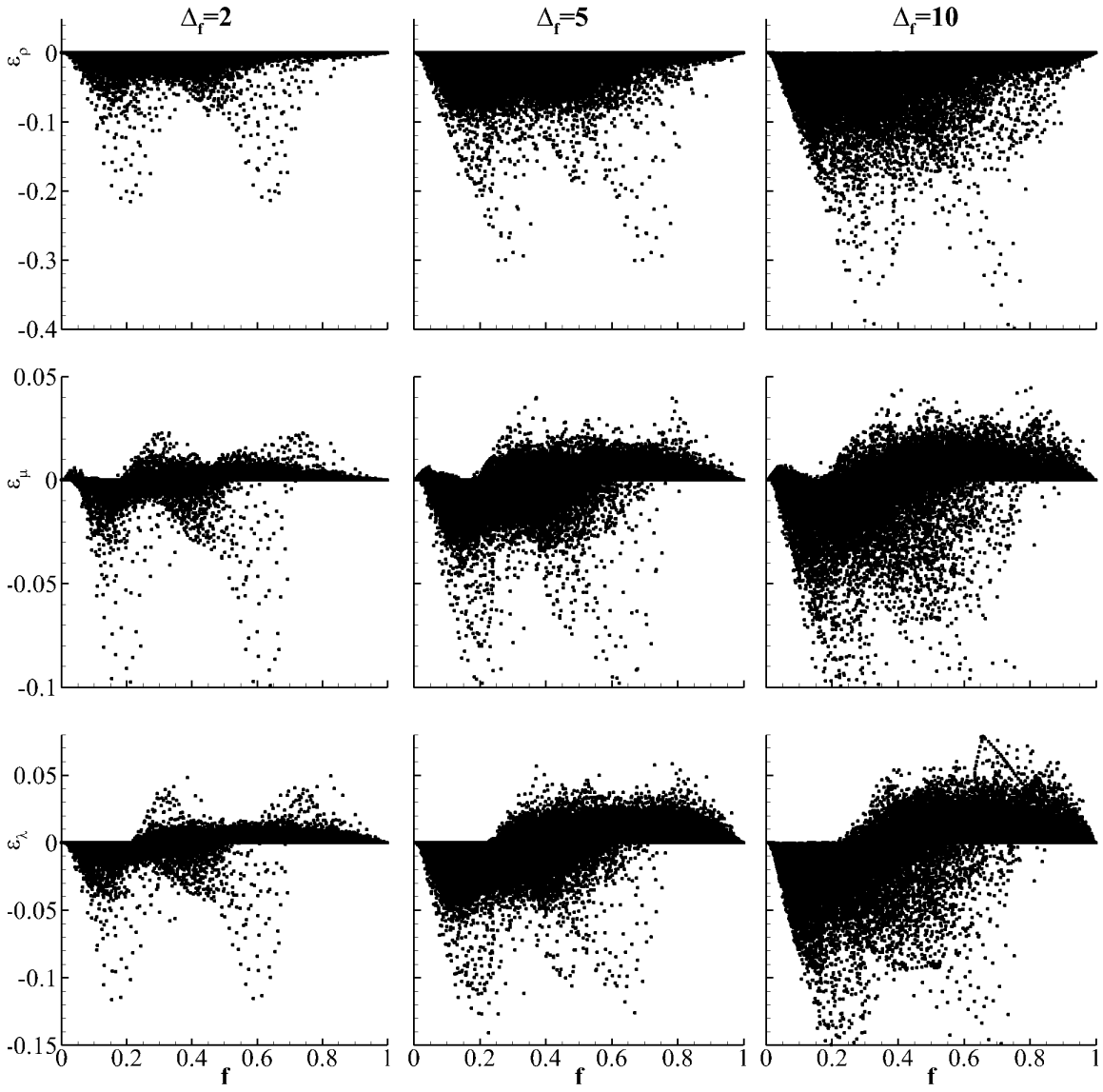

Figure 4.13 – Relative error in representation of filtered density, dynamic viscosity, and thermal conductivity (row-wise top to bottom) at different filter widths (column-wise) as a function of mixture fraction (non-reacting).

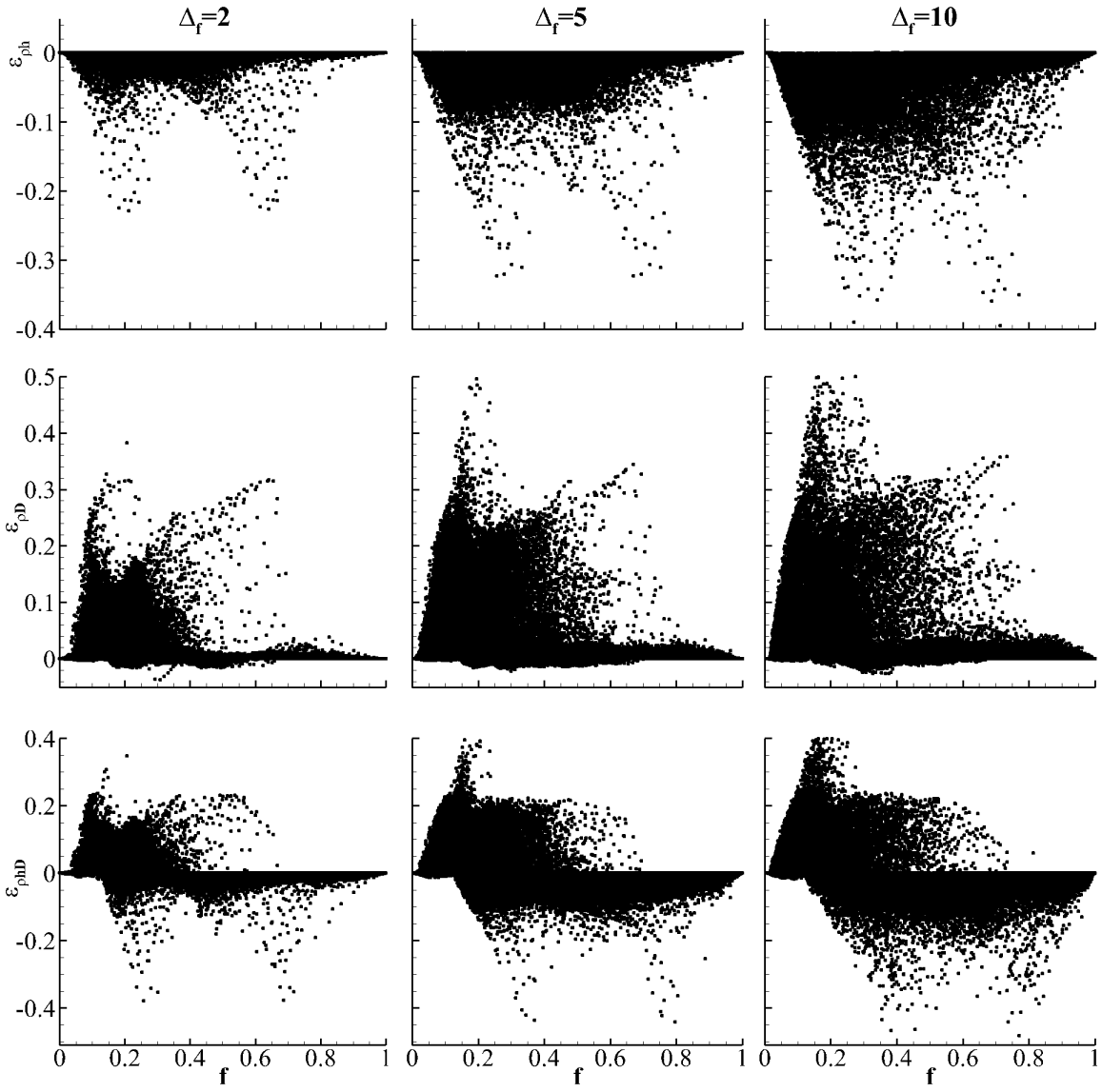

Figure 4.14 – Relative error in representation of enthalpy, mass diffusivity, and thermal diffusivity due to species flux (row-wise top to bottom) at different filter widths (column-wise) as a function of mixture fraction (non-reacting).

4.6 Summary

A quantitative *a priori* investigation of the terms in the governing filtered equations was undertaken for the case of a non-reacting binary-species mixing layer system. Based

on the order of magnitude analysis, the significant terms were identified. In addition to the conventional resolved and subgrid flux terms, two sets of terms are found to be important. These are the residual convective flux terms associated with the subgrid density and enthalpy, and the subgrid viscous and diffusive flux terms in the momentum, energy, and species conservation equations. The magnitudes of the residual convective flux terms are comparable to the leading order terms in the respective equations, and often greater than the conventional subgrid fluxes. The subgrid viscous and diffusive fluxes, although much smaller in magnitude with respect to the overall set of terms, are relevant in magnitude with respect to their corresponding resolved diffusive flux terms. In particular, the subgrid species diffusive fluxes in the filtered species conservation equations was found to be significant and important to account for. The relevance of these subgrid terms increase with filter width, enforcing the need to model these terms in practical LES applications.

Differences between Favre-filtered and Reynolds-filtered state variables were quantified. The deviations between Favre-filtered and Reynolds-filtered temperature and species mass fractions were found to be considerable and increasing with filter width. The resulting errors in representation of filtered thermodynamic and transport properties were also analyzed. Substantial errors were found for the density, mass diffusivity, and enthalpy terms, which increase with filter width. These errors are contributing factors for the increased significance of the subgrid density-related fluxes and the subgrid diffusive fluxes. It is concluded that these subgrid flux terms are relevant at practical LES resolutions and therefore must be accounted for at these operating conditions. *A posteriori* tests are required to ascertain the degree to which the inclusion or exclusion of these terms affect the evolution and dynamics of the resolved scale motion.

CHAPTER 5. REACTING MULTI-COMPONENT STUDIES

5.1 Overview

This chapter extends the study done in Chapter 4 for the case of a reacting multi-species mixing layer system at supercritical pressures. The interactions among turbulent mixing of multiple species, thermodynamics, chemical reactions, and heat release result in highly stratified distributions of temperature, species composition and associated thermodynamic quantities at different turbulent length scales. The interest here is to understand how the subgrid scale interactions affect the representation of the filtered terms in the governing LES equations. There have been very limited multi-species mixing [172, 173] and reacting DNS case studies at supercritical pressures [149, 174] and LES modeling issues are yet to be investigated under these conditions.

The modeling approach for the reacting DNS simulation is described in the Section 3.3. The spatio-temporal data obtained from the DNS simulation is postprocessed to obtain the various filtered and subgrid terms in the LES framework described in Chapter 2. The order of magnitude of each term is quantified through the L^2 norm metric to identify the terms in the governing equations that are important for modeling. The modeling discrepancies associated with the Favre-filtered representation of primitive state variables, and the subsequent computation of the filtered thermodynamic and transport quantities for multi-component mixtures are investigated in detail. The analyses are performed at different filter widths to determine modeling requirements for practical LES applications.

5.2 Flow field description

Figure 5.1 shows the instantaneous flowfield distributions of density, temperature, and OH species mass fraction, along with a simulated shadowgraph visualization for the reacting case. Fine scale turbulent flame structures are adequately captured in the DNS results. The flame is anchored in the recirculation zone immediately downstream of the splitter plate. It then spreads as the vortices roll up and develop downstream. The predicted scalar dissipation rate in the near field of the splitter plate is too small to quench the flamelets, so the flame is stabilized at the LOX post. Since the flame is mixing- and diffusion-controlled, the flame structure correlates strongly with the mixing layers. The combustion process introduces large temperature gradients, and thus induces rapid thermodynamic variations. The distributions of species mass fractions and density display shedding of unburnt oxygen from the liquid oxygen stream due to the shear stress from the hot combustion products, resulting in broad expansion of the flame. The unburnt oxygen ligaments continue to mix with methane in the outer region and form a secondary flame, which persists for a short time before the oxygen parcels are completely depleted through reaction with rich mixtures. It then either merges with larger flame structures through vortex rolling/pairing or disappears by dilution into the low temperature fuel stream. The secondary flame is also observed in Singla et al. [175], but through a different mechanism. Here, the secondary flame is formed from large scale mixing of fuel and oxidizer, whereas in Singla's experiments droplet penetration accounts for the secondary flame. As the flame is convected downstream, multiple pairings of vortices modify the flame structure to a big multi-fold plume. The small flame structures then mix with cold reactants and lose energy. The flame generally continues to follow the oxygen stream and remains close to the high-

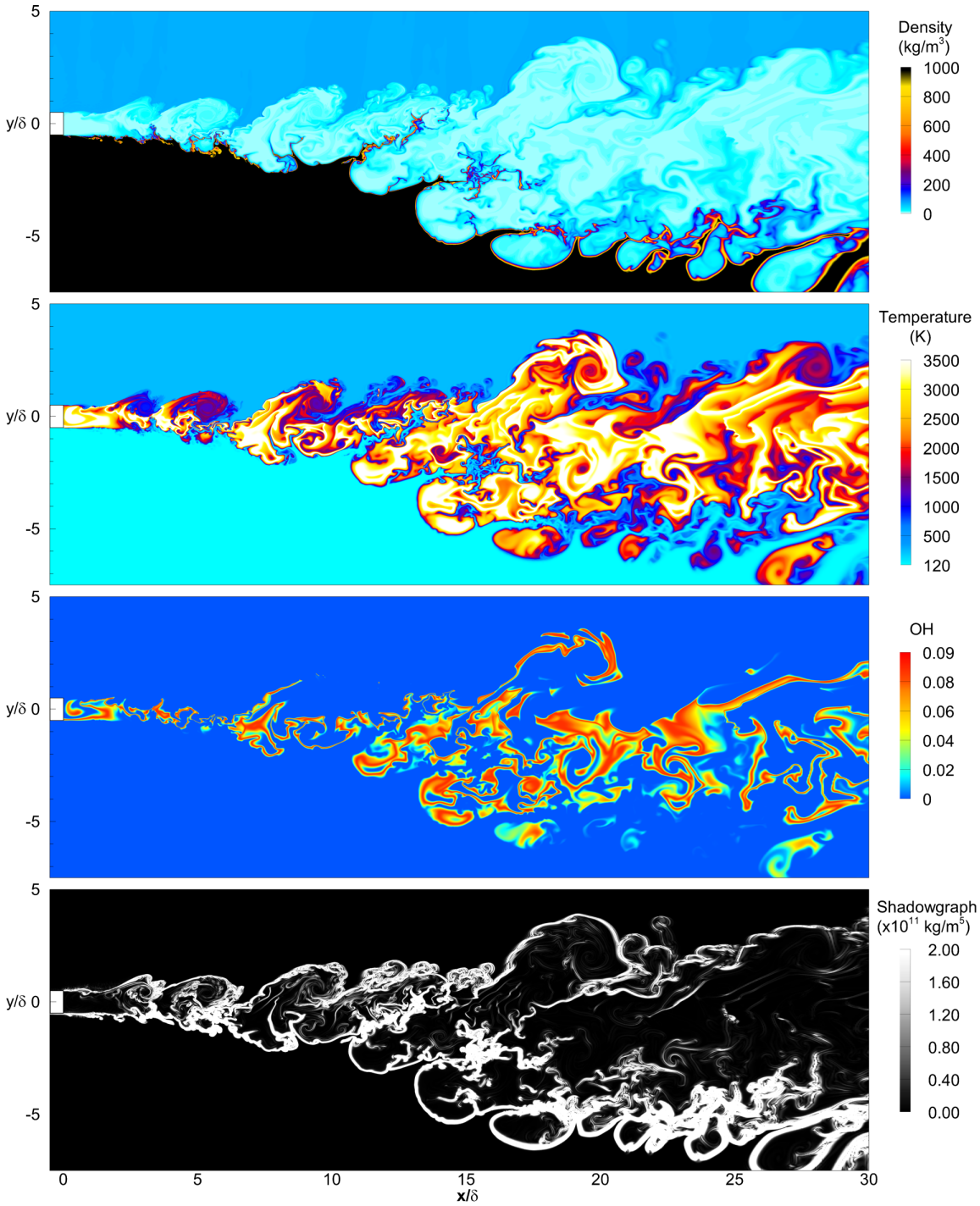

Figure 5.1 – Instantaneous visualizations of the reacting flowfield: distributions of density, temperature, OH mass fraction, and second derivative of density (shadowgraph) (top to bottom).

density oxygen. A small fraction of LOX is heated to form gaseous oxygen, which is sufficient to react with the methane entrained by turbulent mixing.

5.3 Order of magnitude analysis of terms in the filtered equations

5.3.1 Total mass conservation equation

Table 5.1 presents the order of magnitude of terms in the filtered total mass conservation (continuity) equation. The trends are comparable to those observed for the non-reacting case. The resolved convective mass fluxes are the leading order terms, and their magnitudes decrease slightly with filter width. The residual fluxes associated with the subgrid density show a slight increase. These terms are two orders of magnitude smaller at $\Delta_f = 2$, and at $\Delta_f = 10$ they are just one order of magnitude smaller. The relative magnitude of the subgrid fluxes, which is the ratio of the instantaneous subgrid fluxes to the corresponding resolved fluxes, increase from about 3-5% at $\Delta_f = 2$ to about 13% at $\Delta_f = 10$. Figure 5.2 shows the distribution of the relative magnitudes of the residual fluxes at different filter widths. The relative magnitudes are slightly higher compared to the non-reacting case and appear distributed over a wider region, implying an increased significance of subgrid contributions. The terms appear most significant at the flame interface between the hot mixing layer stream and the pure LOX stream. In the flame region, there are rapid variations of density by over three orders of magnitude. The resulting error in the representation of filtered quantities, such as density, result in the amplification of the associated subgrid fluxes in the governing equation. The subgrid contributions are also prominent in the vicinity of the secondary flame. This occurs

between the unburnt cold methane stream and the hot product zone. The density variations in this region are also considerable, although not as prominent as the LOX interface since the methane is already in a gas-like supercritical state. The significance of the subgrid fluxes increase with the filter width.

From a physical perspective, the magnitudes of subgrid contributions depend upon the non-linear behavior of the thermodynamics coupled with the turbulent fluctuations in a local flow region. For example, the subgrid contributions are zero away from the mixing layer even though it is supercritical since the subgrid thermodynamic fluctuations are negligible. In this study, the operating pressure is almost twice the critical pressure of the individual species as well the resultant mixture. For a different operating pressure, where the reduced pressure is close to 1 or only slightly above, the thermodynamic non-linearities could be much higher. The subgrid contributions could then be expected to be higher.

On the other hand, subgrid contributions are found even in the hot product gas regions in the reacting case where the behavior of gases is close to ideal. The contributions are, although, much smaller than those seen in the supercritical regions. In the ideal (hot) gas regions, there are terms associated with the temperature-species mass fraction covariances in the EOS which provide subgrid contributions [105]. These are observed in local regions within the hot mixing layer where the compressibility factor is close to 1. Within the flame there also exist local regions of unreacted and reacted mixtures, leading to subgrid fluctuations in the thermodynamic behavior. The subgrid terms are significant in these regions. The largest subgrid terms are, however, found in the supercritical regions between the pure LOX/CH4 and the hot product streams across which there are strongest thermodynamic variations.

Table 5.1 – Order of magnitude of terms in the filtered continuity equation at different filter widths (reacting), unit: x10^{8} kg m^{-3}s^{-1}.

Δ_f	$\frac{\partial}{\partial x}(\rho(\widetilde{\boldsymbol{Q}})\tilde{u})$	$\frac{\partial}{\partial y}(\rho(\widetilde{\boldsymbol{Q}})\tilde{v})$	$\frac{\partial}{\partial x}(\rho^{sgs}\tilde{u})$	$\frac{\partial}{\partial y}(\rho^{sgs}\tilde{v})$
2	1.27	6.42e-1	4.45e-2	4.15e-2
5	8.40e-1	5.45e-1	7.32e-2	5.84e-2
10	5.24e-1	4.35e-1	7.30e-2	5.30e-2

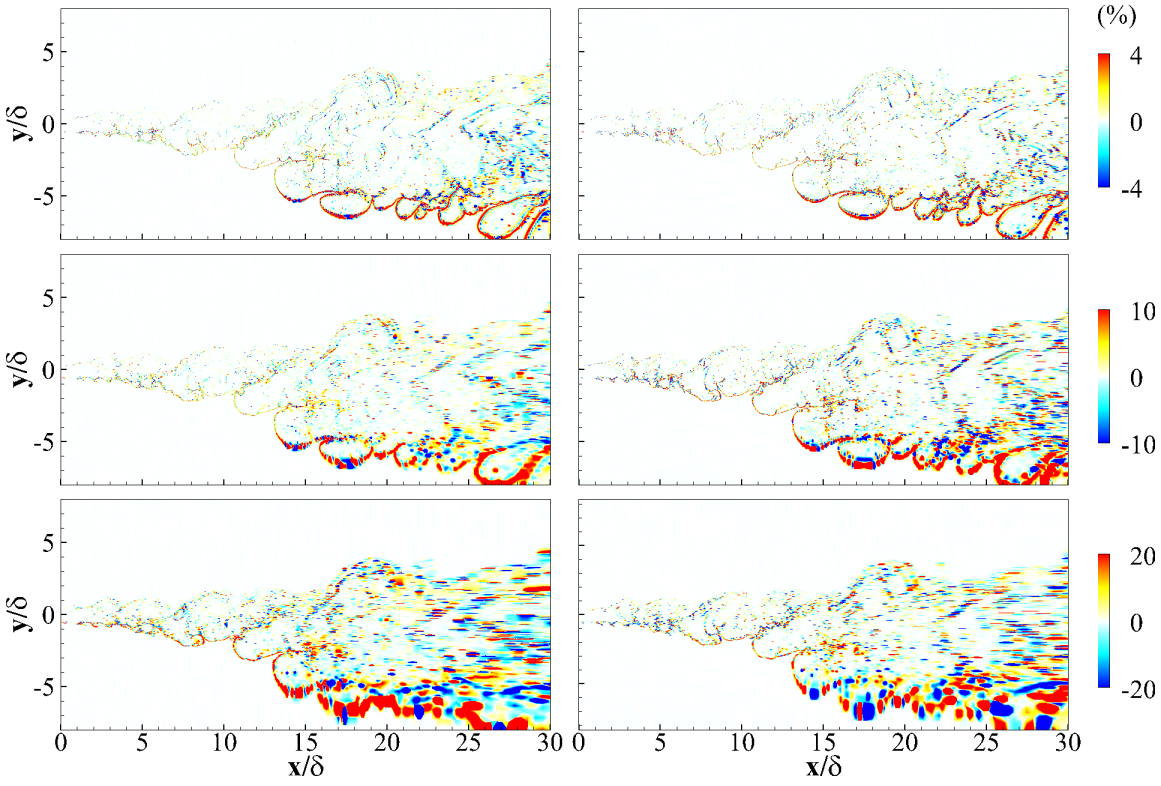

Figure 5.2 – Relative magnitude of residual flux terms associated with the subgrid density in the filtered continuity equation at different filter widths (row-wise) (reacting). x-derivative flux (left) and y-derivative flux (right).

5.3.2 Momentum equations

The order of magnitude of terms in the filtered x- and y-momentum equations are given in Table 5.2 and Table 5.3 respectively. A major difference in the rank of significance of terms is that the pressure gradient is the leading order term in the reacting case. The pressure gradient term is of the same order as the convective flux terms in the x-momentum equation and one order higher than the convective fluxes in the y-momentum equation. The conventional subgrid fluxes are 3-4 orders of magnitude smaller than the resolved convective fluxes and slightly smaller than those obtained in the non-reacting case. This implies that the grid is still over-resolved at these filter widths due to the relatively larger Kolmogorov scales in the reacting case. The residual convective fluxes associated with the subgrid density are, however, significant in magnitude and greater than the conventional subgrid fluxes, similar to the trend observed in the non-reacting case. Figure 5.3 shows the relative magnitude of these residual convective fluxes with respect to the corresponding resolved fluxes. The qualitative trends are identical to those observed for the residual convective fluxes in the continuity equation. The relative magnitudes increase with filter width, implying the need to account for this term for coarse resolution LES simulations.

The magnitudes of the resolved viscous flux terms are slightly higher than the non-reacting case, which can be attributed to the increased viscosity in the high temperature regions. The order of magnitude of the subgrid viscous flux terms decrease slightly with filter width in contrast to the non-reacting case. However, the relative magnitude of the subgrid viscous fluxes with respect to the corresponding resolved viscous fluxes increase with filter width as shown in Figure 5.4. The relative magnitudes are higher and more prominent in the reacting case compared to the non-reacting case.

Table 5.2 – Order of magnitude of terms in the filtered x-momentum equation at different filter widths (reacting), unit: x10^8 kg $m^{-2}s^{-2}$.

Δ_f	$\frac{\partial}{\partial x}(\rho(\widetilde{\boldsymbol{Q}})\tilde{u}\tilde{u})$	$\frac{\partial}{\partial y}(\rho(\widetilde{\boldsymbol{Q}})\tilde{u}\tilde{v})$	$\frac{\partial \tau_{xx}^{sgs}}{\partial x}$	$\frac{\partial \tau_{xy}^{sgs}}{\partial y}$
2	29.11	11.07	3.85e-2	1.46e-1
5	18.96	9.55	3.47e-2	9.39e-2
10	11.55	7.92	4.73e-2	1.57e-1

Δ_f	$\frac{\partial \bar{p}}{\partial x}$	$\frac{\partial}{\partial x}(\rho^{sgs}\tilde{u}\tilde{u})$	$\frac{\partial}{\partial y}(\rho^{sgs}\tilde{u}\tilde{v})$
2	21.35	0.81	0.48
5	16.36	1.25	0.72
10	9.74	1.25	0.68

Δ_f	$\frac{\partial \sigma_{xx}(\widetilde{\boldsymbol{Q}})}{\partial x}$	$\frac{\partial \sigma_{xy}(\widetilde{\boldsymbol{Q}})}{\partial y}$	$\frac{\partial \sigma_{xx}^{sgs}}{\partial x}$	$\frac{\partial \sigma_{xy}^{sgs}}{\partial y}$
2	3.75e-2	1.22e-1	1.14e-2	4.26e-2
5	1.94e-2	7.03e-2	7.05e-3	3.08e-2
10	8.92e-3	4.00e-2	5.66e-3	2.21e-2

Table 5.3 – Order of magnitude of terms in the filtered y-momentum equation at different filter widths (reacting), unit: x10^8 kg $m^{-2}s^{-2}$.

Δ_f	$\frac{\partial}{\partial x}(\rho(\widetilde{\boldsymbol{Q}})\tilde{u}\tilde{v})$	$\frac{\partial}{\partial y}(\rho(\widetilde{\boldsymbol{Q}})\tilde{v}\tilde{v})$	$\frac{\partial \tau_{xy}^{sgs}}{\partial x}$	$\frac{\partial \tau_{yy}^{sgs}}{\partial y}$
2	5.24	3.53	2.69e-2	3.51e-1
5	3.80	2.87	2.50e-2	1.89e-1
10	2.56	2.24	3.67e-2	2.95e-1

Δ_f	$\frac{\partial \bar{p}}{\partial y}$	$\frac{\partial}{\partial x}(\rho^{sgs}\tilde{u}\tilde{v})$	$\frac{\partial}{\partial y}(\rho^{sgs}\tilde{v}\tilde{v})$
2	67.18	0.14	0.22
5	64.38	0.20	0.25
10	57.12	0.20	0.21

Δ_f	$\frac{\partial \sigma_{xy}(\widetilde{\boldsymbol{Q}})}{\partial x}$	$\frac{\partial \sigma_{yy}(\widetilde{\boldsymbol{Q}})}{\partial y}$	$\frac{\partial \sigma_{xy}^{sgs}}{\partial x}$	$\frac{\partial \sigma_{yy}^{sgs}}{\partial y}$
2	3.76e-2	1.89e-1	9.76e-3	1.19e-1
5	2.02e-2	9.80e-2	7.31e-3	3.30e-2
10	1.00e-2	7.42e-2	4.77e-3	1.80e-2

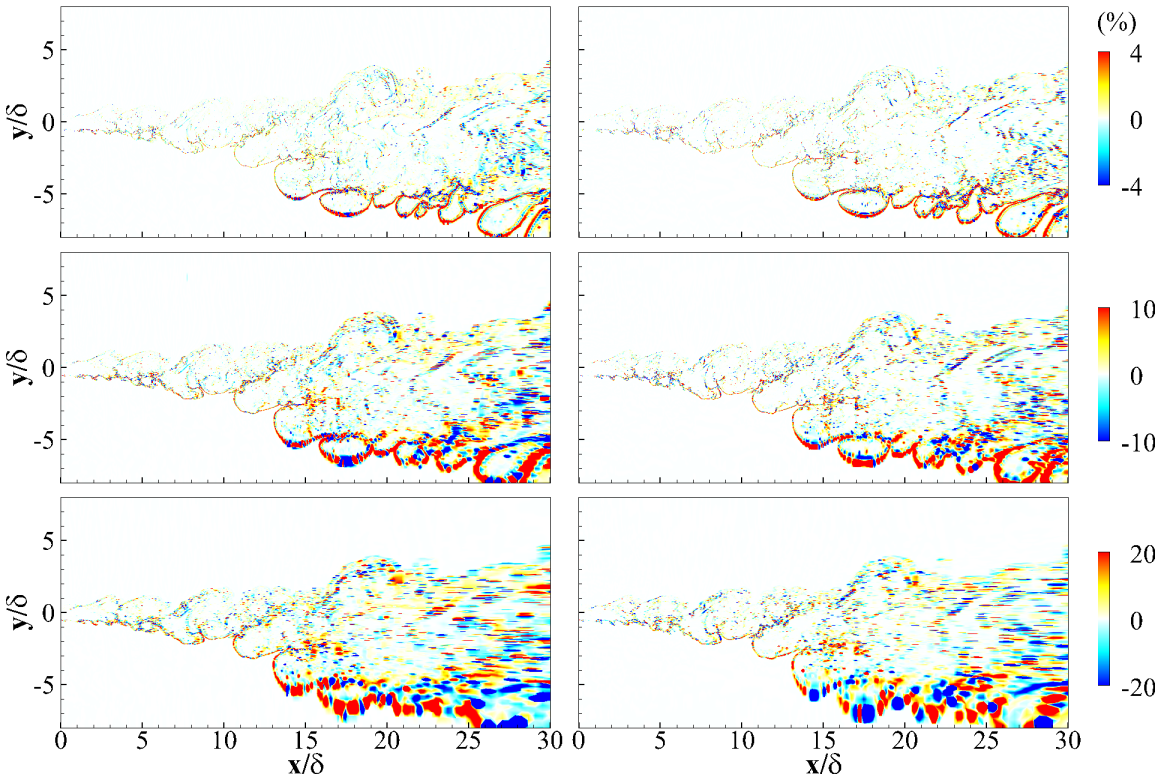

Figure 5.3 – Relative magnitude of residual convective flux terms associated with the subgrid density in the filtered x-momentum equation at different filter widths (row-wise) (reacting). x-derivative flux (left) and y-derivative flux (right).

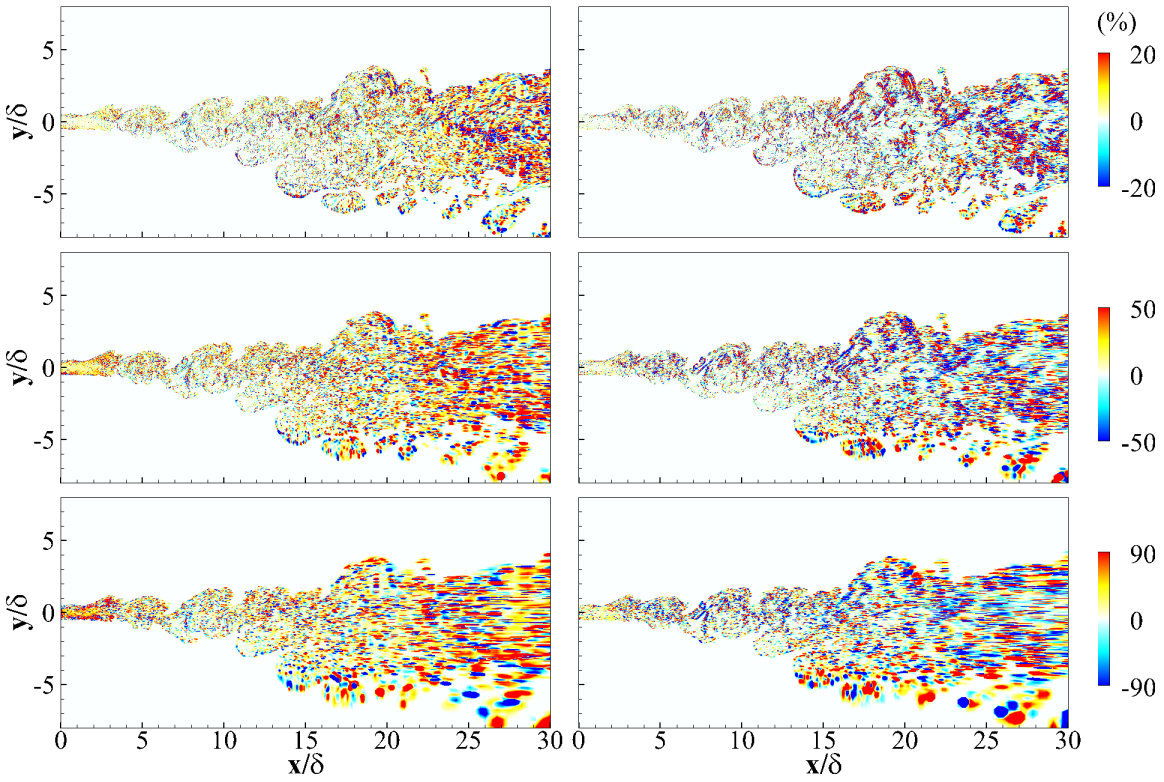

Figure 5.4 – Relative magnitude of subgrid viscous flux terms in the filtered x-momentum equation at different filter widths (row-wise) (reacting). x-derivative flux (left) and y-derivative flux (right).

5.3.3 Total energy conservation equation

The order of magnitude of terms in the filtered energy equation at different filter widths are shown in Table 5.4. The leading order terms are the resolved convective enthalpy fluxes as also observed in the non-reacting case. The magnitudes of the resolved convective fluxes decrease, while the magnitudes of the conventional subgrid enthalpy fluxes increase with filter width. However, the magnitudes of the conventional subgrid enthalpy fluxes are much smaller in magnitude than the resolved enthalpy fluxes. The increased turbulent length scales results in over-resolution even at the largest filter widths

considered. On the other hand, the magnitudes of the residual fluxes associated with the subgrid enthalpy are significant even at these highly resolved conditions. This implies that the errors associated with neglecting these terms are expected to be much larger in typical LES simulations where the conventional subgrid fluxes account for roughly 10% of the total filtered fluxes. The relative magnitudes of these terms are shown in Figure 5.5 and it is seen that the significance of these terms are enhanced compared to the non-reacting case.

The next set of terms of significance are the diffusive heat flux terms. The magnitudes of the resolved diffusive heat fluxes are much larger compared to the non-reacting case. This is due to the increased temperature and species gradients in the turbulent flame and product zones resulting in increased conductive and species diffusive fluxes. The corresponding subgrid diffusive heat fluxes are also considerable in magnitude as shown in Figure 5.6. Note that the colorbar legends are adjusted to provide an appropriate representation over the entire flowfield, and do not represent the maximum/minimum values within the flow field. The peak contributions of the subgrid fluxes are found to be as high as 100-200% in some cells, suggesting that the resolved heat fluxes provide a very inaccurate representation of the actual filtered heat fluxes.

The resolved kinetic energy fluxes are much smaller in magnitude than the leading terms and the associated subgrid terms are even smaller by 1-2 orders of magnitude. Therefore, it might be justifiable to neglect these subgrid terms. The same argument can be extended for the subgrid viscous diffusion terms which are about seven orders of magnitude smaller than the leading convective flux terms.

Table 5.4 – Order of magnitude of terms in the filtered energy equation at different filter widths (reacting), unit: x10^{12} kg $m^{-1}s^{-3}$.

Δ_f	$\frac{\partial}{\partial x}(\rho(\widetilde{\boldsymbol{Q}})h(\widetilde{\boldsymbol{Q}})\tilde{u})$	$\frac{\partial}{\partial y}(\rho(\widetilde{\boldsymbol{Q}})h(\widetilde{\boldsymbol{Q}})\tilde{v})$	$\frac{\partial Q_x^{sgs}}{\partial x}$	$\frac{\partial Q_y^{sgs}}{\partial y}$
2	138.02	85.89	1.47e-1	1.72
5	98.61	78.26	2.41e-1	8.37e-1
10	67.49	68.28	3.16e-1	8.91e-1

Δ_f	$\frac{\partial}{\partial x}(\rho(\widetilde{\boldsymbol{Q}})\tilde{u}_i\tilde{u}_i\tilde{u})$	$\frac{\partial}{\partial y}(\rho(\widetilde{\boldsymbol{Q}})\tilde{u}_i\tilde{u}_i\tilde{v})$	$\frac{\partial \mathcal{J}_x^{sgs}}{\partial x}$	$\frac{\partial \mathcal{J}_y^{sgs}}{\partial y}$
2	5.90e-2	2.55e-2	3.85e-4	6.97e-4
5	4.14e-2	2.30e-2	3.31e-4	5.15e-4
10	2.60e-2	1.98e-2	4.90e-4	8.78e-4

Δ_f	$\frac{\partial H^{sgs}\tilde{u}}{\partial x}$	$\frac{\partial H^{sgs}\tilde{v}}{\partial x}$	$\frac{\partial}{\partial x}(\rho^{sgs}\tilde{u}_i\tilde{u}_i\tilde{u})$	$\frac{\partial}{\partial y}(\rho^{sgs}\tilde{u}_i\tilde{u}_i\tilde{v})$
2	2.10	2.24	1.09e-3	6.43e-4
5	3.48	3.13	1.59e-3	8.26e-4
10	3.61	3.00	1.53e-3	7.79e-4

Table 5.4 continued

Δ_f	$\frac{\partial q_x(\widetilde{\boldsymbol{Q}})}{\partial x}$	$\frac{\partial q_y(\widetilde{\boldsymbol{Q}})}{\partial y}$	$\frac{\partial q_x^{sgs}}{\partial x}$	$\frac{\partial q_y^{sgs}}{\partial y}$
2	4.48	22.33	1.52	8.15
5	2.00	11.40	1.43	6.46
10	1.22	6.06	1.06	4.31

Δ_f	$\frac{\partial}{\partial x}\left(\tilde{u}\sigma_{xx}(\widetilde{\boldsymbol{Q}}) + \tilde{v}\sigma_{xy}(\widetilde{\boldsymbol{Q}})\right)$	$\frac{\partial}{\partial y}\left(\tilde{u}\sigma_{xy}(\widetilde{\boldsymbol{Q}}) + \tilde{v}\sigma_{yy}(\widetilde{\boldsymbol{Q}})\right)$	$\frac{\partial \mathcal{D}_x^{sgs}}{\partial x}$	$\frac{\partial \mathcal{D}_y^{sgs}}{\partial y}$
2	1.61e-4	5.12e-4	6.29e-5	2.98e-4
5	7.65e-5	2.92e-4	3.04e-5	1.17e-4
10	3.09e-5	1.71e-4	2.09e-5	7.94e-5

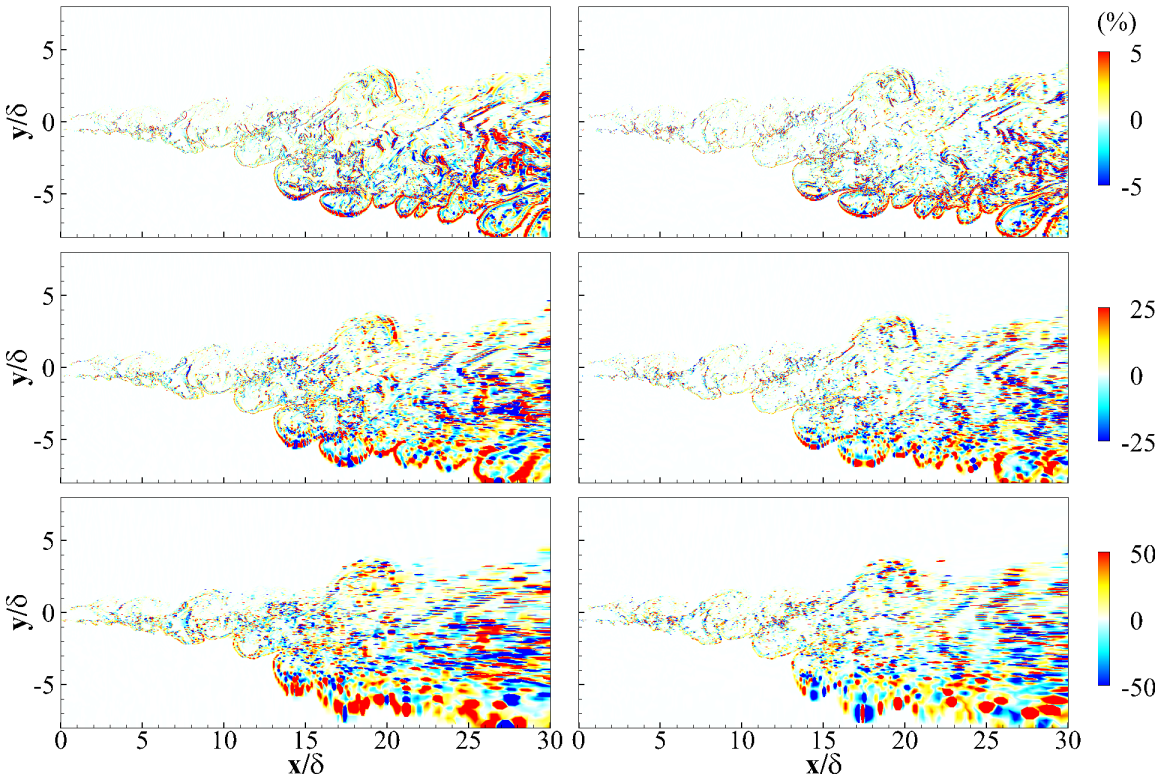

Figure 5.5 – Relative magnitude of residual convective flux terms associated with the subgrid enthalpy in the filtered energy equation at different filter widths (row-wise) (reacting). x-derivative flux (left) and y-derivative flux (right).

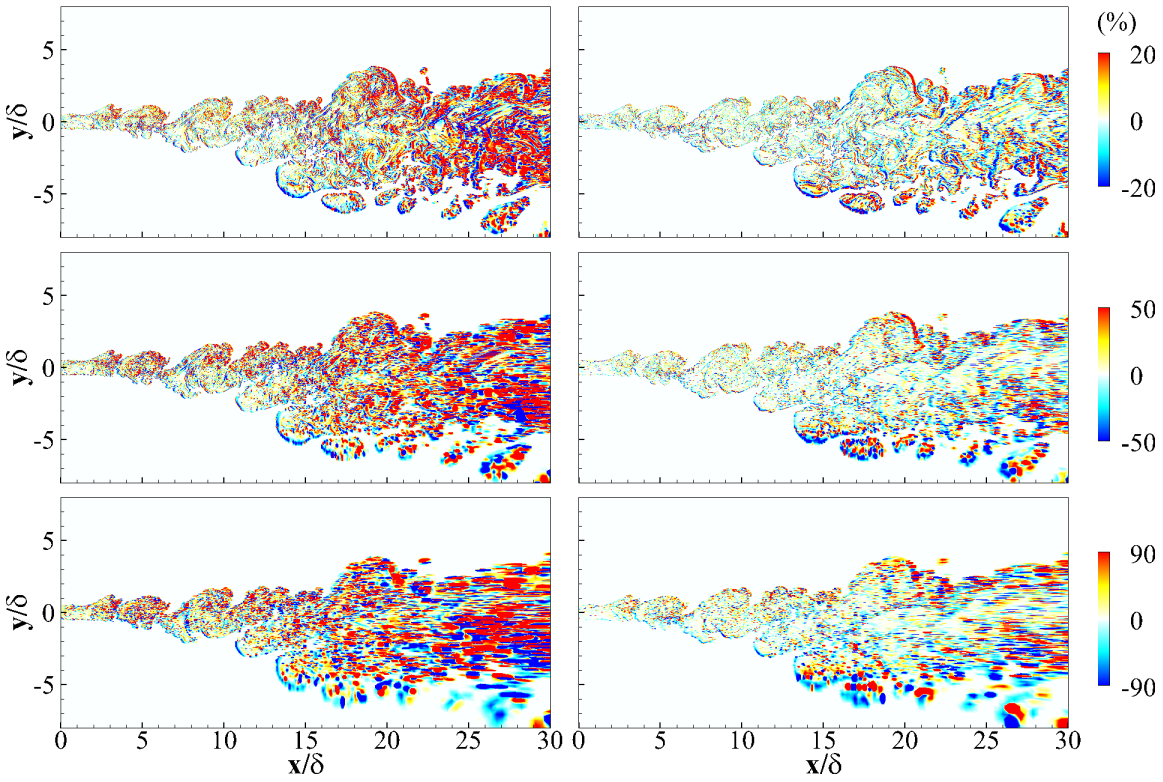

Figure 5.6 – Relative magnitude of subgrid diffusive heat flux terms in the filtered energy equation at different filter widths (row-wise) (reacting). x-derivative flux (left) and y-derivative flux (right).

5.3.4 Species mass conservation equations

For the filtered species mass conservation equations, two representative species are studied for discussion – a reaction product CO_2 and a reaction intermediate OH. The order of magnitudes of terms in their respective filtered mass conservation equations are presented in Table 5.5 and Table 5.6. Note that the reaction rate terms are not reported in this study. For both species, the resolved convective fluxes are the leading terms, and their corresponding subgrid species fluxes are roughly one order of magnitude lower. The residual flux terms associated with the subgrid density are significant in the CO_2 mass

conservation equation but are the least significant terms in the OH conservation equation. The relative magnitude of the residual CO_2 species mass fluxes associated with the subgrid density with respect to the corresponding resolved fluxes are presented in Figure 5.7. These terms attain peak significance in the flame regions close to the LOX stream. Slightly lower magnitudes are also observed in the secondary flame regions close to the methane stream and within the core of the mixing layer where the flame is convoluted by the large-scale structures with local pockets of unreacted species. The distributions for the OH flux terms follow a similar qualitative trend but with a much lower magnitude.

For both species, the resolved and subgrid diffusive fluxes are significantly enhanced owing to the increased species gradients and mass diffusivity in the flame and product regions. The order of magnitude of these terms are comparable to those of the conventional subgrid fluxes. The relative magnitude distributions of the subgrid diffusive fluxes to the resolved diffusive fluxes are shown in Figure 5.8. The figure shows that the subgrid diffusive fluxes are significant especially at larger filter widths and cannot be neglected. Studies on multi-species supercritical mixing layers have suggested the presence of uphill diffusion [173, 176]. Accurate modeling of the filtered diffusive fluxes including subgrid contributions is thus imperative to capture these complex physical phenomena for an accurate representation of species mixing, reactions and heat release in combustion systems.

Table 5.5 – Order of magnitude of terms in the filtered CO_2 species mass conservation equation at different filter widths (reacting), unit: x10^5 kg $m^{-3}s^{-1}$.

Δ_f	$\frac{\partial}{\partial x}(\rho(\widetilde{\boldsymbol{Q}})\tilde{Y}_{CO2}\tilde{u})$	$\frac{\partial}{\partial y}(\rho(\widetilde{\boldsymbol{Q}})\tilde{Y}_{CO2}\tilde{v})$	$\frac{\partial \Phi_{CO2,x}^{sgs}}{\partial x}$	$\frac{\partial \Phi_{CO2,y}^{sgs}}{\partial y}$
2	6.98	5.12	9.79e-2	7.59e-1
5	5.16	4.49	1.60e-1	5.00e-1
10	3.65	3.86	2.11e-1	6.32e-1

Δ_f	$\frac{\partial}{\partial x}(\rho^{sgs}\tilde{Y}_{CO2}\tilde{u})$	$\frac{\partial}{\partial y}(\rho^{sgs}\tilde{Y}_{CO2}\tilde{v})$
2	1.79e-1	1.76e-1
5	2.70e-1	2.38e-1
10	2.58e-1	2.23e-1

Δ_f	$\frac{\partial}{\partial x}J_{CO2,x}(\widetilde{\boldsymbol{Q}})$	$\frac{\partial}{\partial y}J_{CO2,y}(\widetilde{\boldsymbol{Q}})$	$\frac{\partial}{\partial x}J_{CO2,x}^{sgs}$	$\frac{\partial}{\partial x}J_{CO2,y}^{sgs}$
2	3.77e-1	1.55	1.09e-1	4.38e-1
5	1.30e-1	7.87e-1	7.98e-2	3.41e-1
10	4.90e-2	4.06e-1	4.19e-2	2.05e-1

Table 5.6 – Order of magnitude of terms in the filtered OH species mass conservation equation (reacting), unit: x10^5 kg $m^{-3}s^{-1}$.

Δ_f	$\frac{\partial}{\partial x}(\rho(\widetilde{\boldsymbol{Q}})\tilde{Y}_{OH}\tilde{u})$	$\frac{\partial}{\partial y}(\rho(\widetilde{\boldsymbol{Q}})\tilde{Y}_{OH}\tilde{v})$	$\frac{\partial \Phi_{OH,x}^{sgs}}{\partial x}$	$\frac{\partial \Phi_{OH,y}^{sgs}}{\partial y}$
2	2.73	1.60	2.52e-2	1.10e-1
5	1.84	1.36	3.71e-2	1.10e-1
10	1.22	1.10	4.10e-2	1.49e-1

Δ_f	$\frac{\partial}{\partial x}(\rho^{sgs}\tilde{Y}_{OH}\tilde{u})$	$\frac{\partial}{\partial y}(\rho^{sgs}\tilde{Y}_{OH}\tilde{v})$
2	6.67e-3	5.19e-3
5	1.49e-2	2.17e-2
10	2.22e-2	3.21e-2

Δ_f	$\frac{\partial}{\partial x}J_{OH,x}(\widetilde{\boldsymbol{Q}})$	$\frac{\partial}{\partial y}J_{OH,y}(\widetilde{\boldsymbol{Q}})$	$\frac{\partial}{\partial x}J_{OH,x}^{sgs}$	$\frac{\partial}{\partial x}J_{OH,y}^{sgs}$
2	4.07e-1	1.55	1.27e-1	2.46e-1
5	1.30e-1	7.78e-1	8.52e-2	2.31e-1
10	4.64e-2	3.97e-1	4.21e-2	1.72e-1

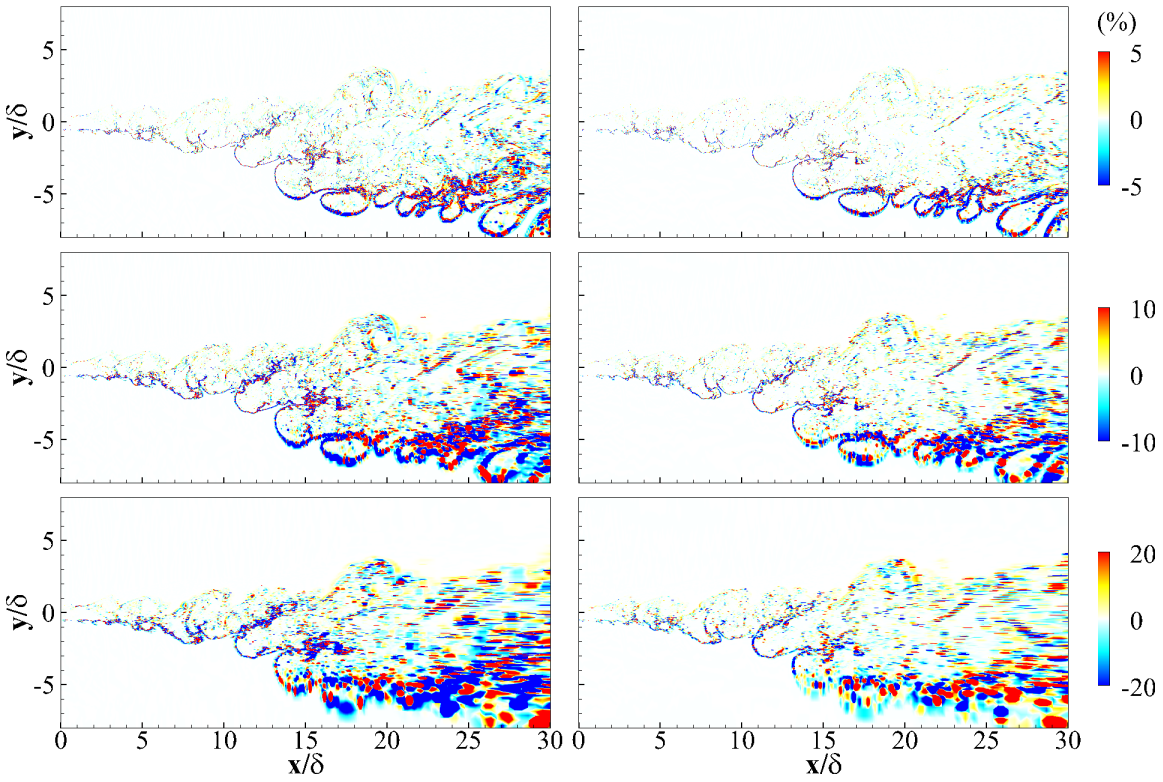

Figure 5.7 – Relative magnitude of residual convective flux terms associated with the subgrid density in the filtered CO_2 mass conservation equation at different filter widths (row-wise) (reacting). x-derivative flux (left) and y-derivative flux (right).

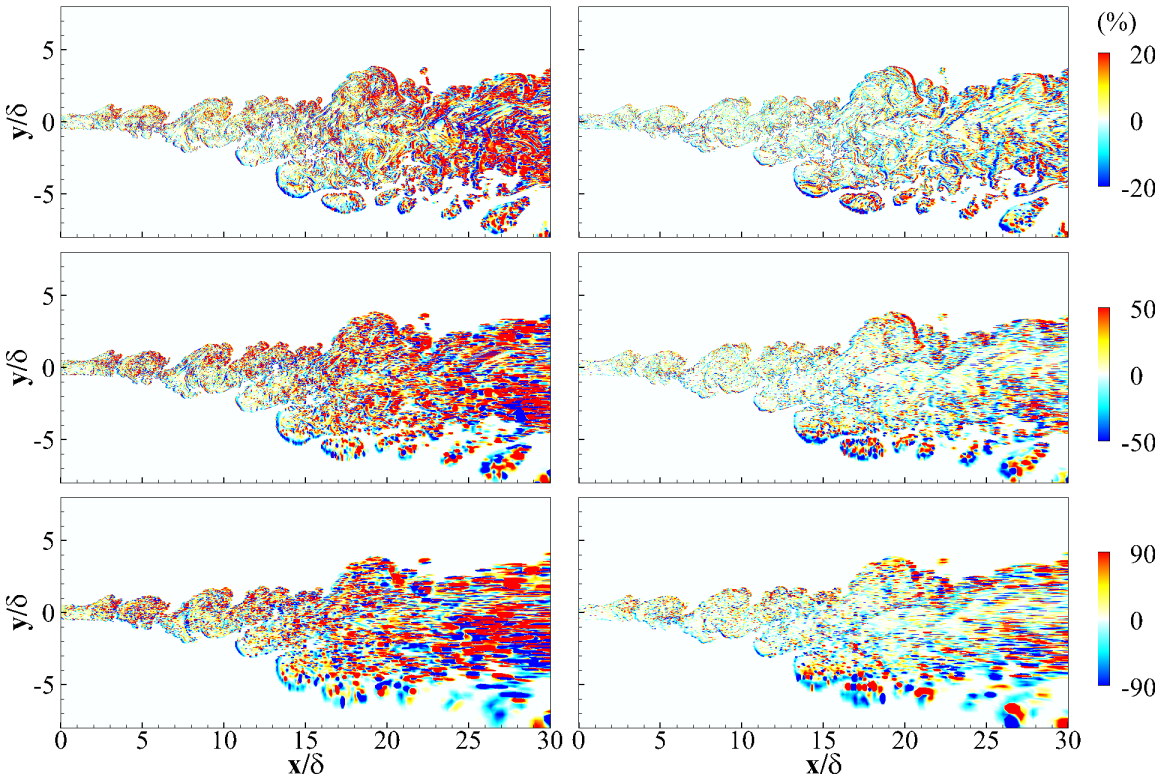

Figure 5.8 – Relative magnitude of subgrid diffusive heat flux terms in the filtered CO_2 conservation equation at different filter widths (row-wise) (reacting). x-derivative flux (left) and y-derivative flux (right).

5.4 Differences between Favre- and Reynolds-filtered state variables

The use of Favre-filtered state variables to compute Reynolds-filtered quantities contributes to the new set of subgrid fluxes. To quantify these contributions to the subgrid fluxes, the deviations between Favre- and Reynolds-filtered variables are investigated in Figure 5.9. The deviations between the two filtered velocities are minimal, similar to the non-reacting case. In contrast, significant deviations are seen for the temperature and species mass fractions, which appear to be greater than those seen in the non-reacting case. Deviations of temperature as high as 500-1000 K are found at the large filter widths. The

chemical reactions coupled with the turbulent mixing result in substantial variations of chemical composition and temperature at different scales across the mixing layer. The strong temperature variations at the small scales arise from local pockets of unreacted and reacted species. The resulting variations in density at the subgrid scales skew the Favre-filtered variables towards the values corresponding to the denser species at the subgrid level. In this case, the density of the unburnt mixture is much higher and the corresponding temperature and Y_{CO2} are lower compared to the burnt mixture. Therefore, the Favre-filtered temperature and Y_{CO2} are lower than the corresponding Reynolds-filtered quantities.

The relative differences between the Favre and Reynolds-filtered temperature and species mass fractions are quantified in Figure 5.10. Unlike the non-reacting case, where the relative errors are highest in the intermediate mixture fraction regions in the core of the mixing layer, the peak errors for the reacting case are obtained at the extreme lean (just above 0) and extreme rich (just below 1) mixture fractions. These regions correspond respectively to the primary and secondary flames, which form the interfaces of the unburnt LOX and methane streams with the hot reacted products in the mixing layer. Strong variations in density occur across these interfaces which are further enhanced by turbulent mixing. The relative errors at the LOX/product interface are higher than at the methane/product interface owing to larger density variations across the LOX/product interface. Peak errors in these regions are as high as 50-75% at moderate and large filter widths. These deviations partially explain the increased significance of the subgrid diffusive fluxes.

The large discrepancies between Reynolds-filtered and Favre-filtered temperatures and species mass fractions are expected to have important consequences for the representation of the filtered reaction rate in the conventionally used quasi-laminar chemistry model [177-179], where the filtered reaction rate is modeled as the reaction rate computed in terms of Favre-filtered state variables. These issues need further investigation.

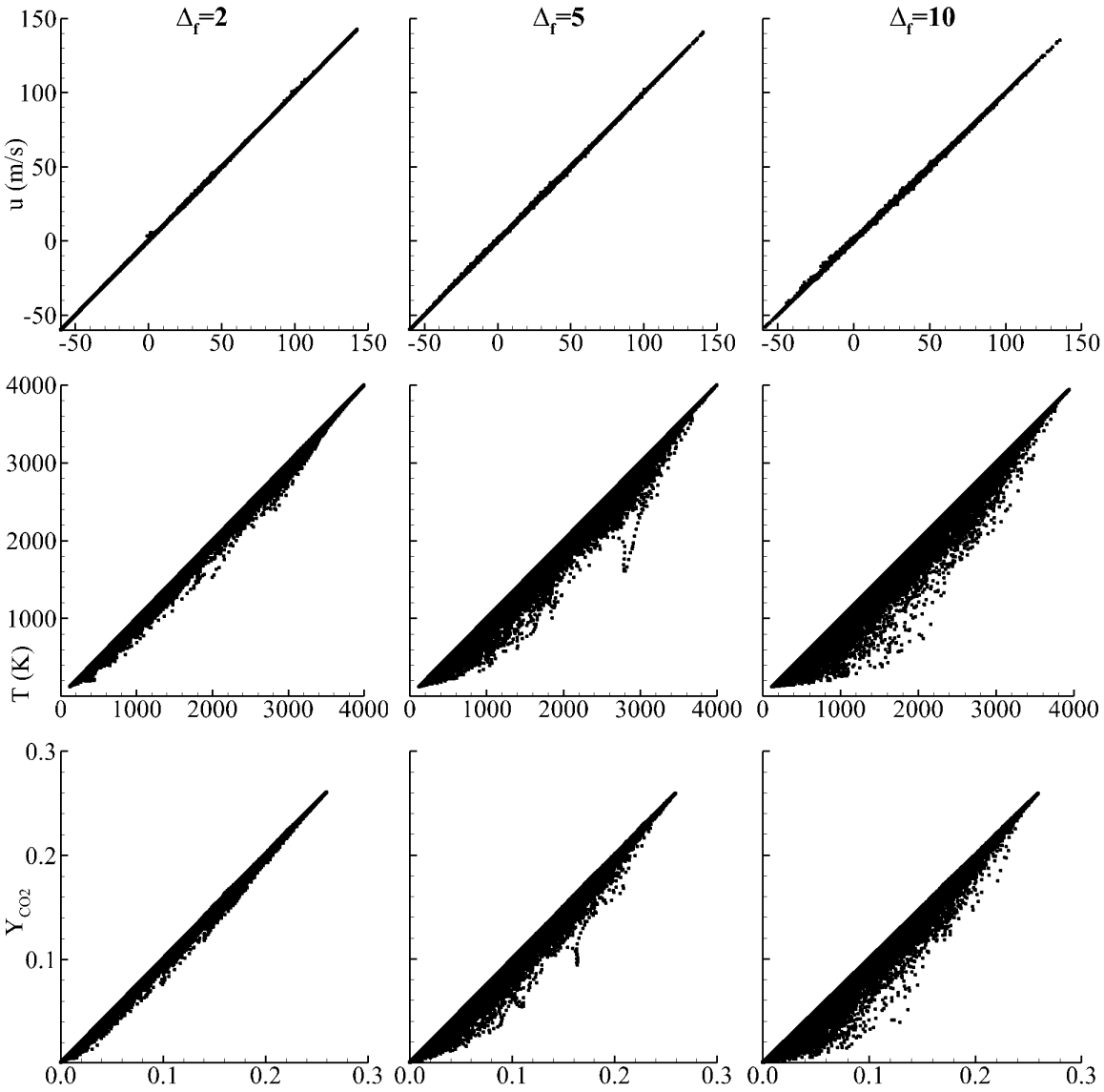

Figure 5.9 – Comparison between Reynolds-filtered (x-axis) and corresponding Favre-filtered (y-axis) state variables at different filter widths (reacting).

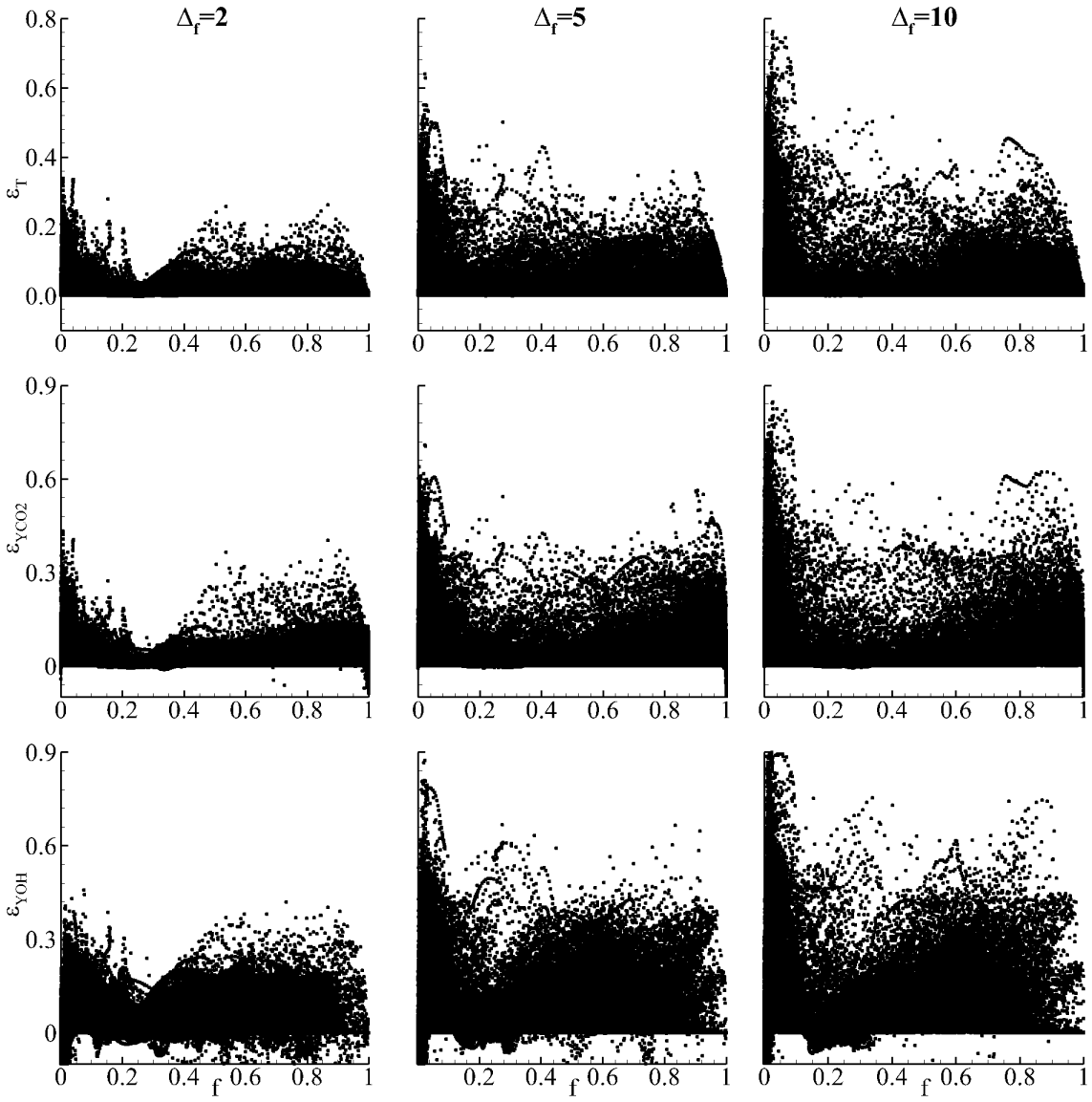

Figure 5.10 – Relative difference between Reynolds-filtered and Favre-filtered state variables at different filter widths as a function of mixture fraction (reacting).

5.5 Errors in representation of filtered thermodynamic and transport properties

The differences between Reynolds-filtered and Favre-filtered primitive state variables lead to associated differences between the filtered thermodynamic and transport

co-coefficients and the corresponding quantities evaluated using Favre-filtered state variables. Figure 5.11 and Figure 5.12 show the distributions of the relative error of relevant coefficients at different filter widths as a function of mixture fraction. The relative error is computed according to Equation 4.2. The distributions of the errors are quantitatively and qualitatively different and more complex than their counterparts in the non-reacting flow. First, the errors are significantly larger for most quantities than those observed for the non-reacting case, especially for the molecular viscosity and thermal conductivity. Second, the errors are prominent over a wide region in the mixture fraction space. The peak errors in the reacting case occur in the leanest mixture fraction regions which correspond to the interface between the LOX stream and the hot mixture in the mixing layer where the properties variations at the small scales are the highest.

In the non-reacting flow, the variation of temperature is relatively smaller, whereas chemical heat release broadens the range of variation for temperature in the reacting case. The local mixture composition and temperature also vary rapidly in the reacting flowfield in accordance with the turbulent mixing and coupled interactions with flame structures. The thermodynamic and transport properties are a non-linear function of temperature and species concentrations, and this dependence is more complex for multi-species reacting flows. Each species component has a unique thermodynamic behavior which could be very different from those of the other components. The thermodynamic properties of the resulting mixture are determined by the instantaneous species composition through the non-linear mixing laws. The critical points of the mixture could also be significantly different from those of the constituent species, and the mixture could undergo transition from ideal gas to supercritical fluid and vice-versa in the flame regions. The rapid variation

of thermodynamic state variables in conjunction with the non-linear thermodynamic and transport property relationships gives rise to significant variation of these quantities at various length scales. The first moments of the primitive state variables cannot accurately represent the thermodynamic status of the fluid parcel enclosed by the LES filter. Neglecting the contributions of these turbulence-chemistry-thermodynamic interactions at the subgrid scales, therefore contribute to complex deviations between exact filtered and approximated representations. This issue is recognized for the reaction rate terms [178, 180-182] but largely neglected for other dependent quantities. The magnitude of errors shown in this work reinforces the need to account for subgrid scale effects in the thermodynamic and transport property calculations for multi-component real-fluid mixtures.

The error in the filtered density in the intermediate mixture fractions are smaller compared to the non-reacting case. This can be attributed to the fact that at high temperatures, the mixture exhibits close to ideal behavior where the equation of state is more linear. The compressibility factor Z of the hot gases are close to one, thereby removing the effect of subgrid fluctuations of Z on the filtered density. Errors due to the subgrid fluctuations in the temperature and species mass fractions. Large errors also occur close to the LOX interface, and these errors contribute to significance of the new set of residual convective flux terms that are associated with the subgrid density.

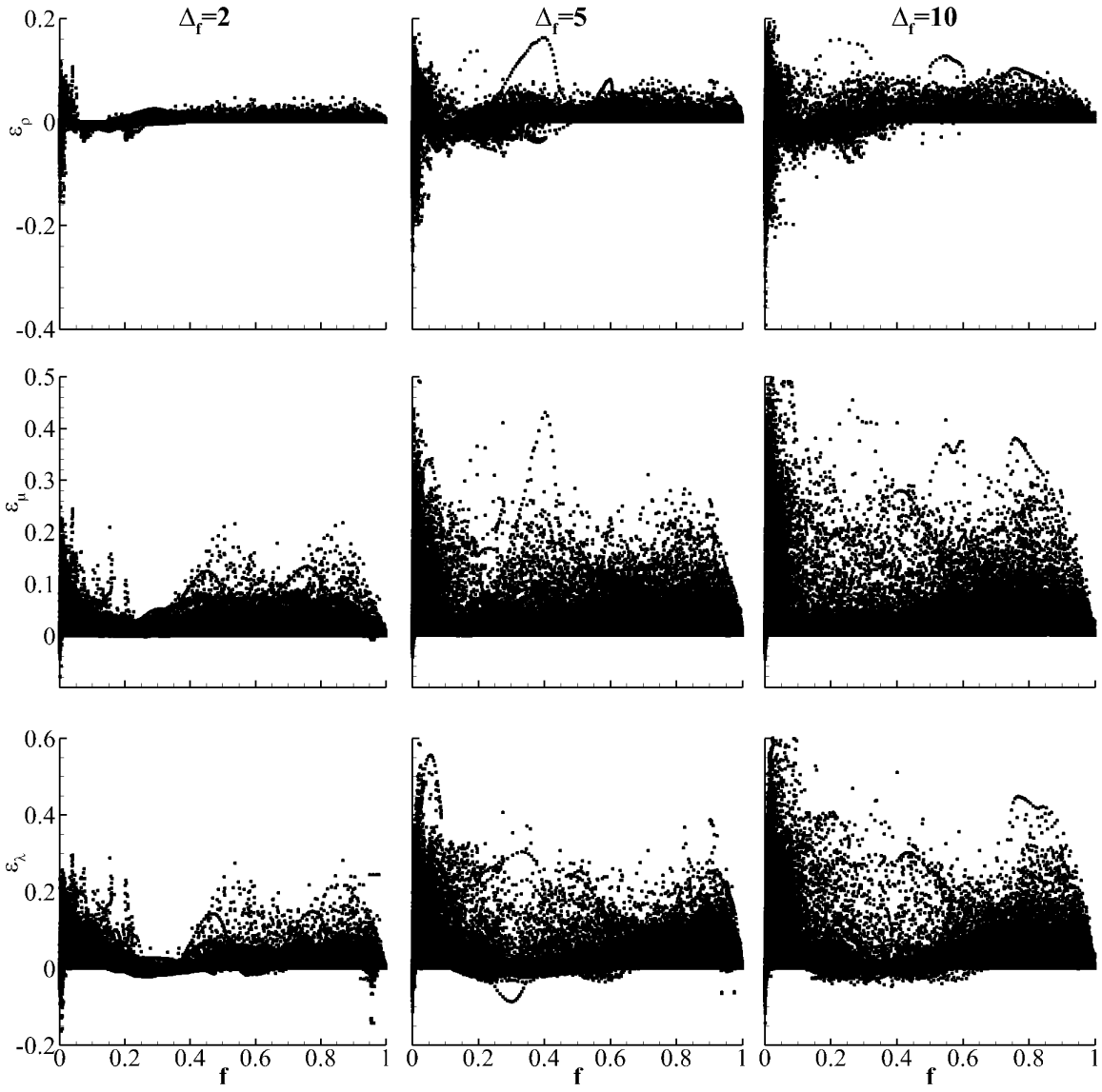

Figure 5.11 – Relative error in representation of filtered density, dynamic viscosity, and thermal conductivity (row-wise top to bottom) at different filter widths (column-wise) as a function of mixture fraction (reacting).

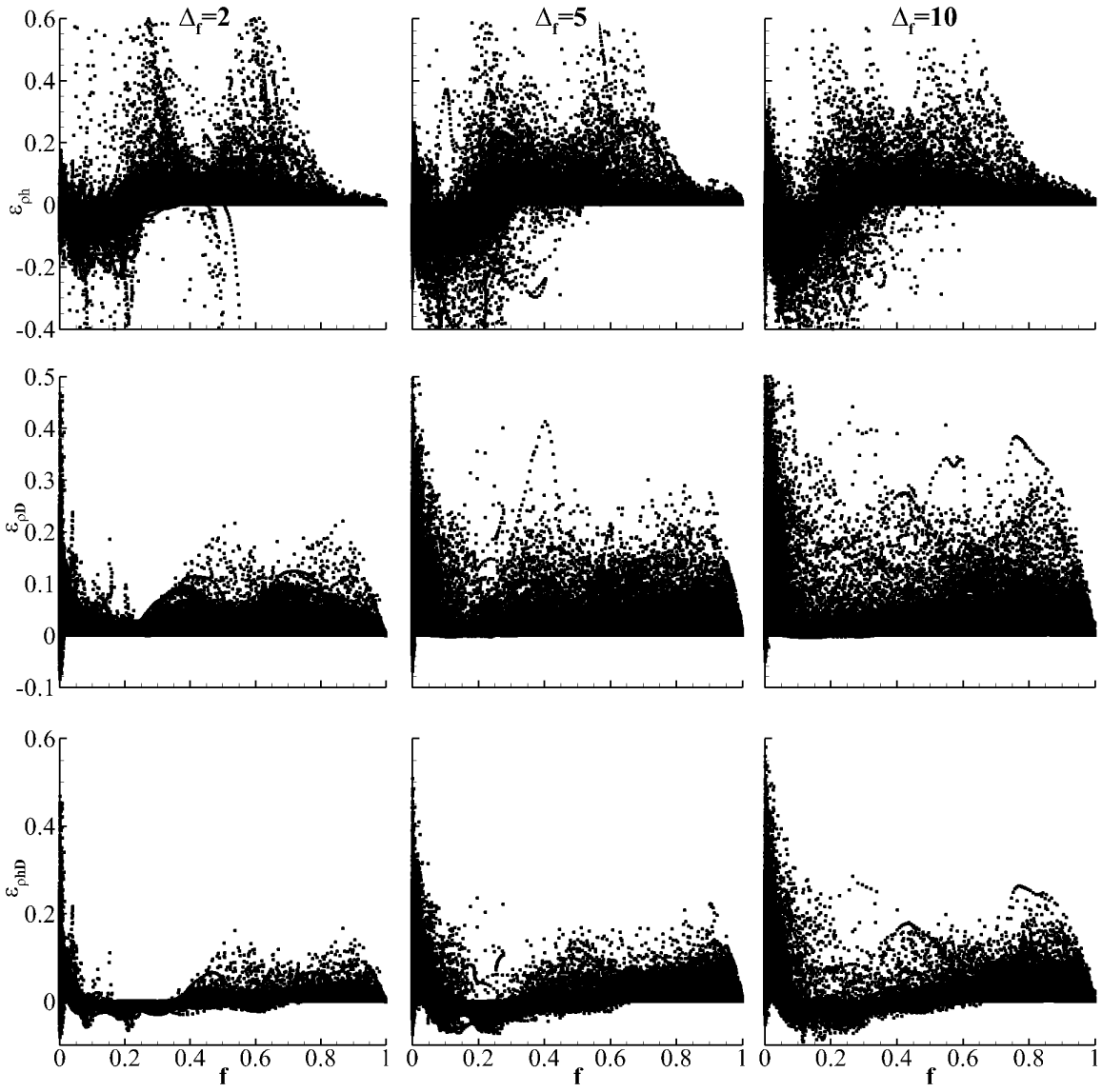

Figure 5.12 – Relative error in representation of enthalpy, mass diffusivity, and thermal diffusivity due to species flux (row-wise top to bottom) at different filter widths (column-wise) as a function of mixture fraction (reacting).

5.6 Summary

A priori analyses of the subgrid terms in the filtered conservation equations for LES are performed for the case of a multi-species reacting flow system at supercritical pressure.

It is found that the conventional subgrid fluxes are lower in magnitude than the values for the non-reacting case. However, the residual convective fluxes associated with the subgrid density and enthalpy are still substantial in magnitude and relevant with respect to the leading resolved convective fluxes, especially at high filter widths. Additionally, the resolved diffusive heat and species fluxes are found to be higher in magnitude compared to the non-reacting case, owing to the increased diffusivity and thermal/species gradients. These resolved terms and the corresponding subgrid diffusive fluxes are found to be significant in the corresponding to the energy and species mass conservation equations. It is recognized that modeling of the filtered diffusive fluxes in the LES formulation should necessarily account for the subgrid contributions for accurate modeling of molecular diffusion and mixing in reacting flow systems.

Differences between the Favre-filtered and Reynolds-filtered temperature and species mass fractions are shown to be substantial especially in the flame interfaces close to the unburnt mixtures. The errors in the representation of filtered thermodynamic and transport properties are also quantified. It is shown that the errors in density are relatively smaller while those of the other transport coefficients are significant increased compared to the non-reacting case. These errors are contributing factors for the subgrid diffusive flux terms, underscoring the importance of modeling these subgrid effects.

CHAPTER 6. A PRIORI ASSESSMENT OF CONVENTIONAL SUBGRID SCALE MODELS

6.1 Overview

The subgrid terms that are important to account for in the filtered equations have been identified in Chapters 4 and 5. Models have been investigated and applied for a subset of these terms. These terms are the conventional subgrid fluxes originating from the filtered convective flux terms, namely the subgrid stresses τ_{ij}^{sgs}, the subgrid enthalpy fluxes Q_j^{sgs} and the subgrid species fluxes Φ_{kj}^{sgs}. The definitions of these terms were introduced in Section 2.3.3. *A priori* assessment of models for these terms is performed in this chapter. Two representative modeling approaches are identified as candidates for the study - the dynamic Smagorinsky/eddy-diffusivity model (DSM) [53, 64, 146] and the dynamic mixed model (DMM) [67, 147, 148]. The model formulations are described in Section 2.4.

There are three primary objectives of this study. Before attempting to model the remaining set of subgrid terms, it is first useful to investigate the existing subgrid modeling approaches to determine if the underlying principles of these approaches can be extended to other terms. The second objective of this study is to evaluate the accuracy of existing models under supercritical conditions to determine their validity and accuracy under these conditions. These subgrid models were originally developed for application to incompressible turbulent flows. The extension and application of these models for compressible flows have been investigated in past studies [65, 67, 81]. However, limited studies exist for turbulent supercritical mixing. Selle et al. [99] have conducted *a priori*

analysis of different constant-coefficient models for the subgrid fluxes using temporal mixing layer data. Taskinoglu and Bellan [107, 183] investigated dynamic models in conjunction with subgrid corrections for the pressure and heat flux terms. The focus of their studies was to evaluate the influence of the new subgrid corrections rather than the conventional models. These studies are limited to temporal mixing configurations at low Reynolds numbers. Similar studies for high Reynolds number inhomogeneous flows and supercritical reacting flows are lacking [184, 185]. The final objective of this study is to quantify the performance of different models at different LES resolutions. This is required to establish guidelines and recommendations for LES resolutions for practical applications where validation data is not easily available.

The DNS data described in Chapter 4 and Chapter 5 for the non-reacting and reacting cases are used to compute the exact values of the subgrid fluxes on LES grids of different filter widths. The corresponding modeled fluxes are computed purely based on the filtered (or Favre-filtered depending upon the definition) state variables (density, velocity, enthalpy, species mass fractions) on the LES grid level. This is done in a manner consistent with the procedure in an LES simulation, without using any information from the DNS data. The test-filtering for the dynamic model evaluation is performed at a filter width which is twice the LES filter width [53]. The grid-filtering for the scale-similarity term is performed at the same filter width as the LES grid. The numerical implementation of grid and test-filtering are extended from the approach of Zang et al. [147]. While Zang et al. [147] use linear interpolation to numerically evaluate the filters on uniform grids, the current study follows a quadratic interpolation based on Lagrange polynomials using a 9-point stencil around the LES cell to account for the presence of non-uniform cells.

6.2 Assessments of models for the non-reacting case

6.2.1 Subgrid stresses (velocity-velocity covariances)

The subgrid stresses τ_{ij}^{sgs} represent subgrid covariances between velocity components. The dynamic Smagorinsky model is used to model the deviatoric components of the subgrid stress tensor, while the isotropic components are either combined with the pressure term or modeled separately using the Yoshizawa model [63]. In this study, the assessments are done only for the deviatoric subgrid stress tensor. Figure 6.1 shows the comparison of the distributions of the subgrid stress component τ_{xy}^{sgs} from different models at three different filter widths. The top row shows the subgrid stress field computed from the DNS, which are considered the true (exact) values. The middle and bottom rows show the corresponding field distributions modeled by the dynamic Smagorinsky and mixed models. With increasing filter width, the magnitudes of the subgrid stresses increase as more information is contained within the filter scale. Qualitatively both models capture the overall pattern of the subgrid stress distribution. However, the dynamic Smagorinsky model underpredicts the magnitudes of the subgrid stress. The magnitudes of the subgrid stress predicted by the dynamic mixed model are much closer to the exact values obtained from the DNS. The results for the other subgrid stress components provide similar trends and are not shown here.

To quantify the accuracy of the model predictions, the correlation coefficient between exact and model predicted values is used as a metric. This is a widely used measure for *a priori* quantification of model accuracies [56, 78, 81]. The correlation coefficients for the various subgrid stress components modeled using the dynamic

Smagorinsky and dynamic mixed models are computed at different filter widths and presented in Table 6.1. The dynamic mixed model shows significantly higher correlations than the dynamic Smagorinsky model for all three components. The correlations for the $\tau_{xx}^{sgs,d}$ term are lower than the other two terms for both models. The correlation coefficients decrease with increasing filter width implying a reduction in model accuracy at coarser grid resolutions. Both these models are founded on the principle of scale-similarity, either for dynamic evaluation of the model-coefficient as in the dynamic Smagorinsky model, or for direct evaluation of the stress component through the scale-similarity in the mixed model. The notion of scale-similarity is strictly valid only in the inertial length scale regime where the turbulent energy transfer is in equilibrium. This imposes limits on the filter widths or grid resolution that can be considered acceptable for high-fidelity LES simulations.

The performance of the dynamic mixed model even at higher filter widths is higher than that of the dynamic Smagorinsky model at low filter widths. From a fundamental viewpoint, the subgrid stress tensor is modeled in terms of the resolved strain through a scalar eddy-viscosity in the Smagorinsky and other eddy-viscosity based modeling approaches. This enforces the alignment of the principal axes of the subgrid stress and strain rate tensors, which is not necessarily true for complex flows. The inclusion of the scale-similarity term relaxes this assumption and significantly increases the correlation of the subgrid stresses [55]. From another perspective, the mixed model directly computes the resolved Leonard stress component of the subgrid stress tensor, requiring less contribution from the eddy-viscosity term. It was also found in this study that the scale-similarity model without the eddy-viscosity component in fact provides a higher correlation coefficient.

However, it has been shown that this model by itself does not provide the necessary subgrid scale dissipation to the flow [55] and is therefore not considered in practice. The better performance of the dynamic mixed model at higher filter widths renders support for its use in practical LES applications.

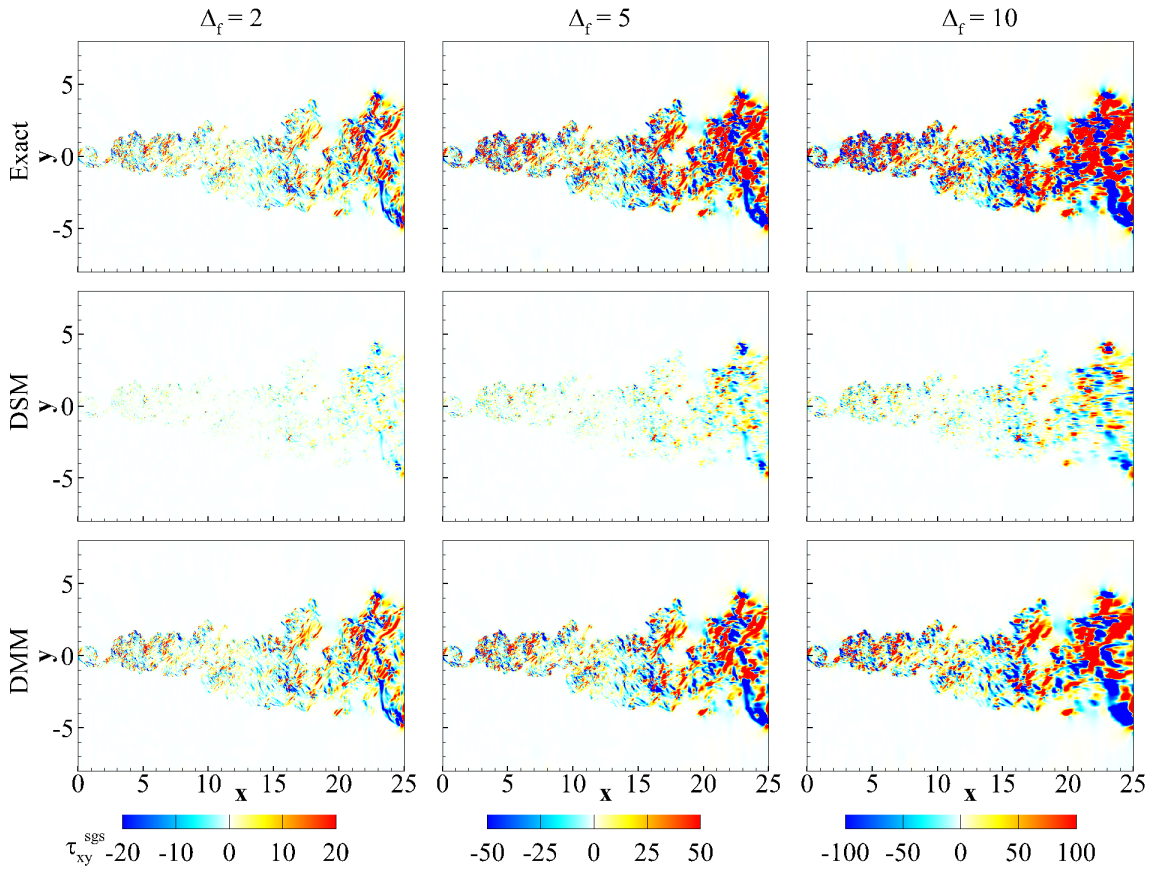

Figure 6.1 – Comparison of τ_{xy}^{sgs} distributions obtained from DNS (top row), and those modeled with dynamic Smagorinsky (middle) and dynamic mixed models (bottom) at different filter widths (column wise) (non-reacting case).

Table 6.1 – Correlation coefficients between exact and modeled subgrid stresses at different filter widths (non-reacting case).

	DSM			DMM		
Δ_f	**2**	**5**	**10**	**2**	**5**	**10**
$\tau_{xx}^{sgs,d}$	0.17	0.15	0.14	0.59	0.53	0.39
τ_{xy}^{sgs}	0.33	0.27	0.26	0.97	0.84	0.66
$\tau_{yy}^{sgs,d}$	0.30	0.27	0.25	0.94	0.83	0.69

6.2.2 Subgrid enthalpy and species fluxes (velocity-scalar covariances)

The subgrid enthalpy and species fluxes represent the interactions between the velocity and scalar fields at the subgrid level, known as the subgrid velocity-scalar covariances. The term scalar here refers to enthalpy (or temperature) and species mass fractions. These terms are modelled as gradient diffusive terms following an eddy-diffusivity approach, analogous to the eddy-viscosity hypothesis. In the dynamic eddy-diffusivity framework, the subgrid heat/species diffusivities are modelled in terms of the eddy-viscosity and turbulent Prandtl/Schmidt numbers. Detailed formulations are provided in Section 2.4.1. In the mixed model, the scale-similarity terms provide the Leonard contributions to the subgrid fluxes.

Figure 6.2 and Figure 6.3 show the subgrid enthalpy flux Q_x^{sgs} and the subgrid CH_4 species flux $\Phi_{CH4,x}^{sgs}$ distributions obtained from DNS (exact) and the model predictions at different filter widths. The qualitative trends of the two model predictions compare reasonably well with the exact subgrid fluxes. The dynamic eddy-diffusivity model slightly underpredicts the magnitude of the subgrid fluxes. As the filter width increases, the differences between the model and exact subgrid fluxes become more evident, especially in the far-field mixing regions where large scale vortical structures are present.

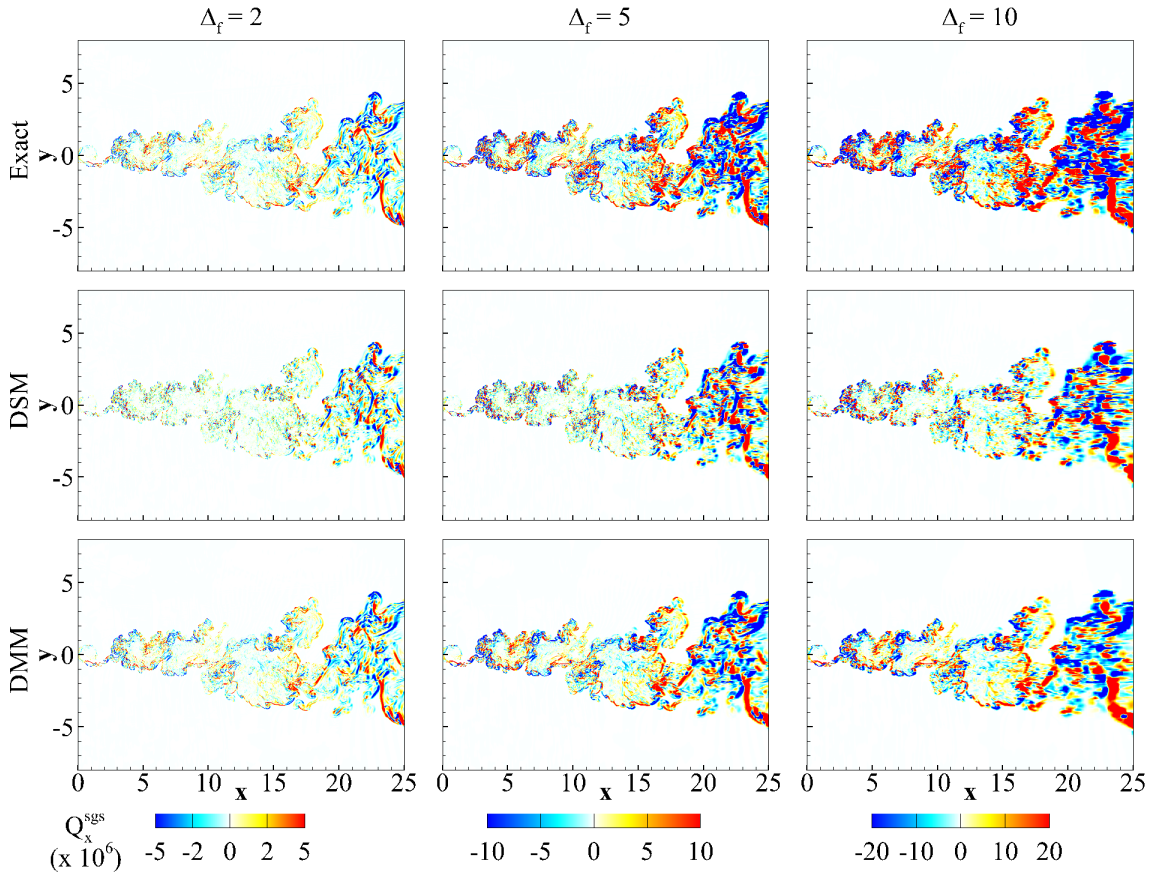

Figure 6.2 – Comparison of Q_x^{sgs} distributions obtained from DNS (top row), and those modeled with dynamic Smagorinsky (middle) and dynamic mixed models (bottom) at different filter widths (column wise) (non-reacting case).

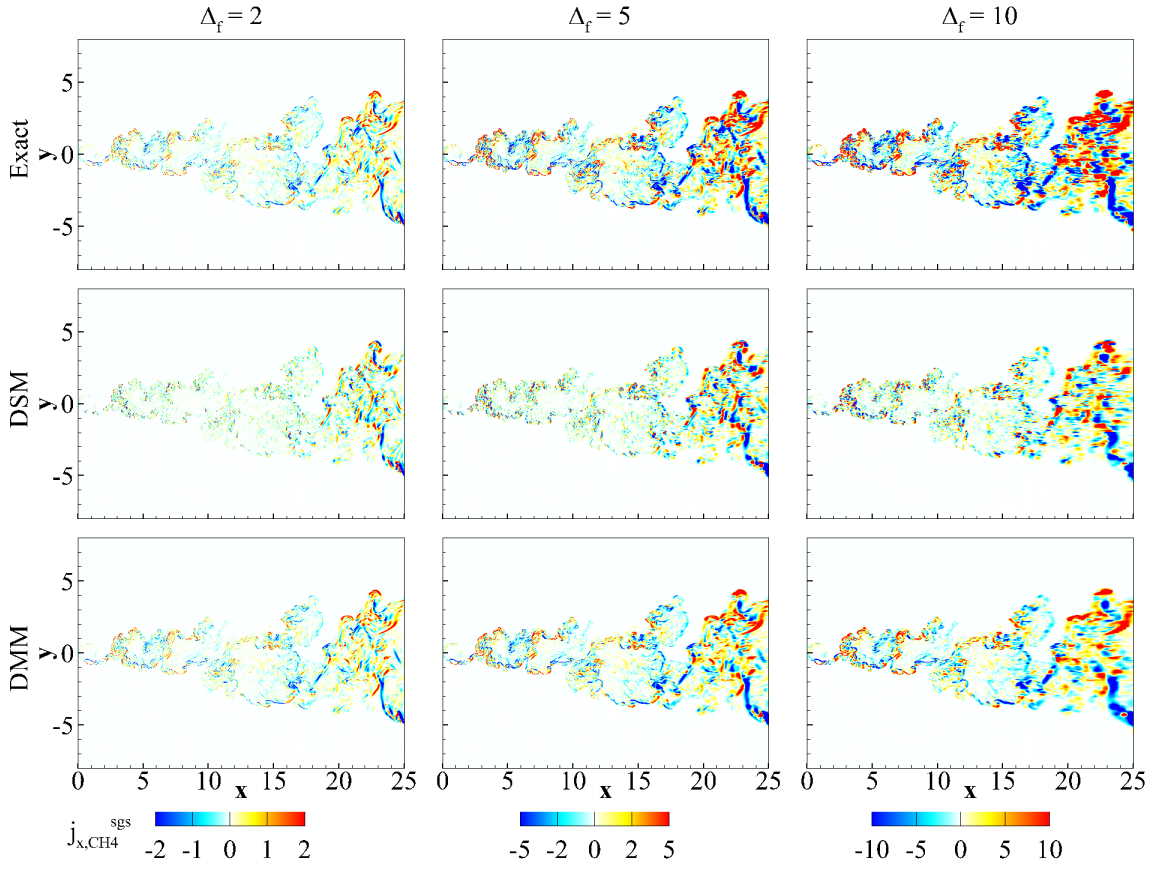

Figure 6.3 – Comparison of $\Phi_{x,CH4}^{sgs}$ distributions obtained from DNS (top row), and those modeled with dynamic Smagorinsky (middle) and dynamic mixed models (bottom) at different filter widths (column wise) (non-reacting case).

Table 6.2 presents the correlation coefficients of the two model predictions for the different subgrid flux components at different filter widths. The trends are similar to those identified for the subgrid stresses. The dynamic mixed model shows significantly higher correlations for all flux components than the dynamic eddy-diffusivity model. The correlations of both models decrease with increase in filter width. However, the correlation of the dynamic mixed model at the largest filter width is still greater than the correlation of the dynamic eddy-diffusivity model at the smallest filter width. At higher filter widths,

the correlations for the subgrid velocity-scalar covariances are also seen to be lower than those of the subgrid velocity-velocity covariances. The correlations of the dynamic eddy-diffusivity model at moderate and high filter widths are too low suggesting that may not be appropriate for application at these resolutions.

Table 6.2 – Correlation coefficients between exact and modeled subgrid enthalpy and species fluxes at different filter widths (non-reacting case).

	DSM			DMM		
$\boldsymbol{\Delta_f}$	**2**	**5**	**10**	**2**	**5**	**10**
$\boldsymbol{Q_x^{sgs}}$	0.19	0.14	0.13	0.95	0.78	0.59
$\boldsymbol{Q_y^{sgs}}$	0.37	0.14	0.04	0.93	0.73	0.49
$\boldsymbol{\Phi_{CH4,x}^{sgs}}$	0.19	0.14	0.14	0.95	0.78	0.59
$\boldsymbol{\Phi_{CH4,y}^{sgs}}$	0.36	0.14	0.11	0.93	0.73	0.49

6.3 Assessments of models for the reacting case

6.3.1 Subgrid stresses (velocity-velocity covariances)

The exact and modeled deviatoric components of the subgrid stresses are computed using the DNS and filtered DNS data respectively for the reacting case. Figure 6.4 shows the distributions of the τ_{xy}^{sgs} component computed at different filter widths. The distribution

of the subgrid stress is qualitatively and quantitatively different than those observed in the non-reacting case. Qualitatively, the peak subgrid stresses in the reacting case are found to occur in the peripheral regions of the mixing layer corresponding to the primary and secondary flame branches. In the non-reacting case, the peak subgrid stresses occur within the core of the mixing layer. Quantitatively, the magnitudes of the subgrid stresses in the reacting case are lower by almost a factor of 5 compared to the non-reacting case. The reason for this can be attributed partly to the increase in the smallest turbulent length scales due to heat release accompanied by increase in kinematic viscosity. The dynamic mixed model predictions compare reasonably well with the exact subgrid stresses, while the dynamic Smagorinsky shows significantly underpredicted values.

The correlation coefficients of the modeled subgrid stress components are presented in Table 6.3. The correlation coefficients are reduced compared to the non-reacting case, especially for the dynamic Smagorinsky model at high filter widths. The performance of the dynamic mixed model is still reasonable, and better than that of the dynamic Smagorinsky model. The findings support the use of the dynamic mixed model at reasonable grid resolutions for LES of reacting flows at supercritical conditions.

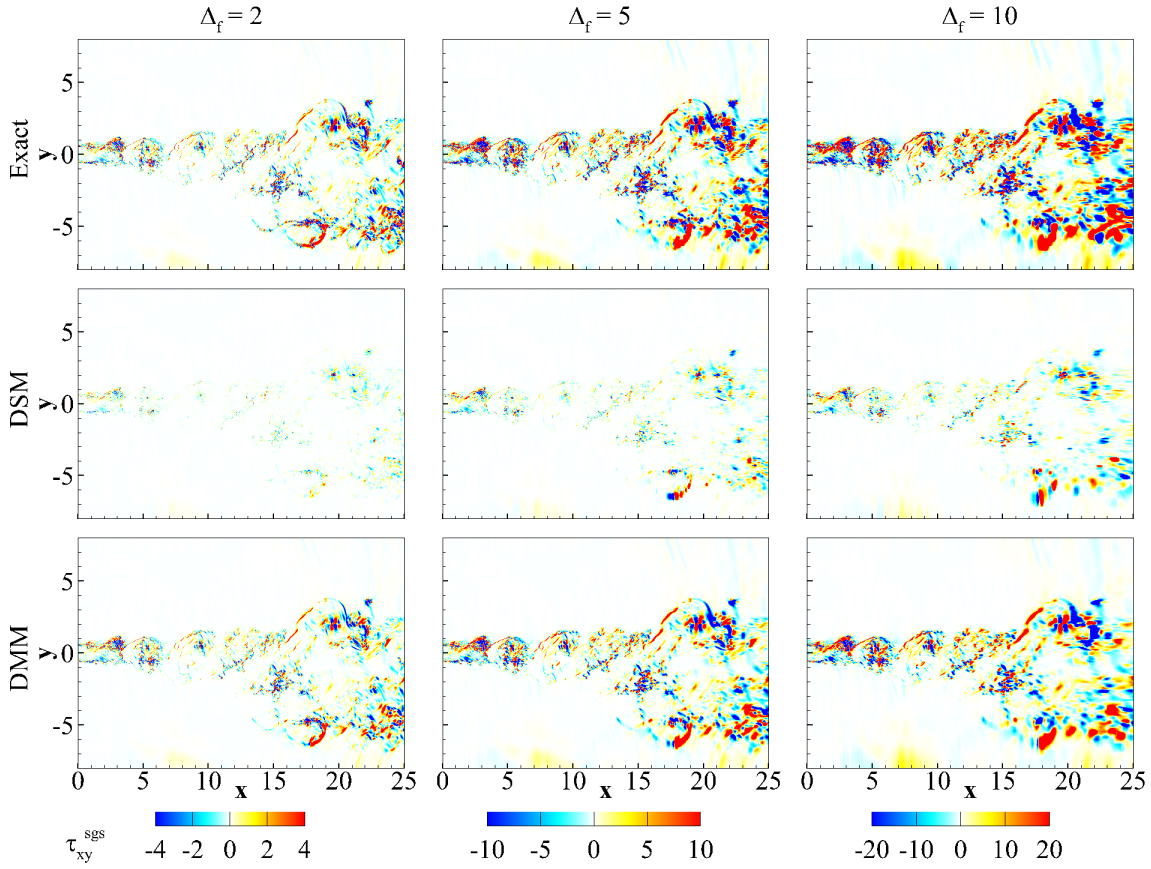

Figure 6.4 – Comparison of τ_{xy}^{sgs} distributions obtained from DNS (top row), and those modeled with dynamic Smagorinsky (middle) and dynamic mixed models (bottom) at different filter widths (column wise) (reacting case).

Table 6.3 – Correlation coefficients between exact and modeled subgrid stresses at different filter widths (reacting case).

	DSM			DMM		
Δ_f	**2**	**5**	**10**	**2**	**5**	**10**
$\tau_{xx}^{sgs,d}$	0.24	0.17	0.03	0.47	0.28	0.17
τ_{xy}^{sgs}	0.21	0.14	0.03	0.70	0.55	0.31
$\tau_{yy}^{sgs,d}$	0.30	0.22	0.09	0.73	0.65	0.37

6.3.2 Subgrid enthalpy and species fluxes (velocity-scalar covariances)

Figure 6.5 and Figure 6.6 show the distributions of the exact and modeled subgrid enthalpy flux Q_x^{sgs} and the subgrid CH_4 diffusive flux $\Phi_{CH4,x}^{sgs}$. The dynamic mixed model predictions show a qualitatively good correlation to the exact subgrid fields. The dynamic eddy-diffusivity models on the other hand show very poor comparison. Apart from the evident underprediction of the dynamic eddy-diffusivity modeled fluxes, it is found upon careful observation that the predicted signs of the subgrid fluxes are also opposite to those the exact subgrid fluxes in several regions. Such negatively correlated regions are found especially in the downstream flame region close to the LOX stream. Studies on reacting flows at low pressures have identified the presence of counter gradient scalar transport especially at larger filter widths [186, 187]. It is questionable whether the classical gradient

diffusion hypothesis can be assumed to model subgrid scale fluxes under these conditions. The correlation coefficients of the model predictions presented in Table 6.4 also show that the correlations for the dynamic eddy-diffusivity models are significantly lowered and close to zero at higher filter widths. The dynamic mixed models on the other hand still show a reasonable correlation. The strength of this model can be ascribed to the scale-similarity term which does not assume gradient diffusion hypothesis. The dynamic mixed model also maintains a reasonable accuracy at high filter widths.

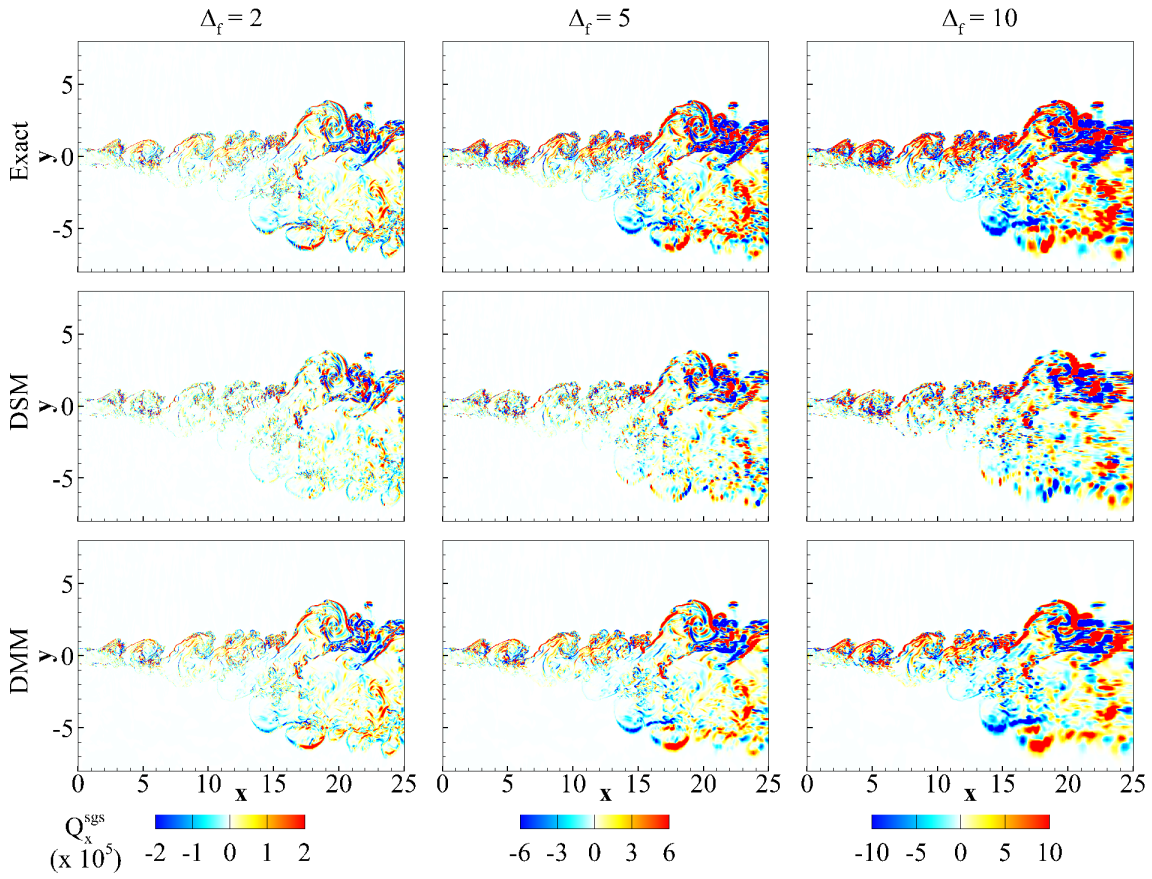

Figure 6.5 – Comparison of Q_x^{sgs} distributions obtained from DNS (top row), and those modeled with dynamic Smagorinsky (middle) and dynamic mixed models (bottom) at different filter widths (column wise) (reacting case).

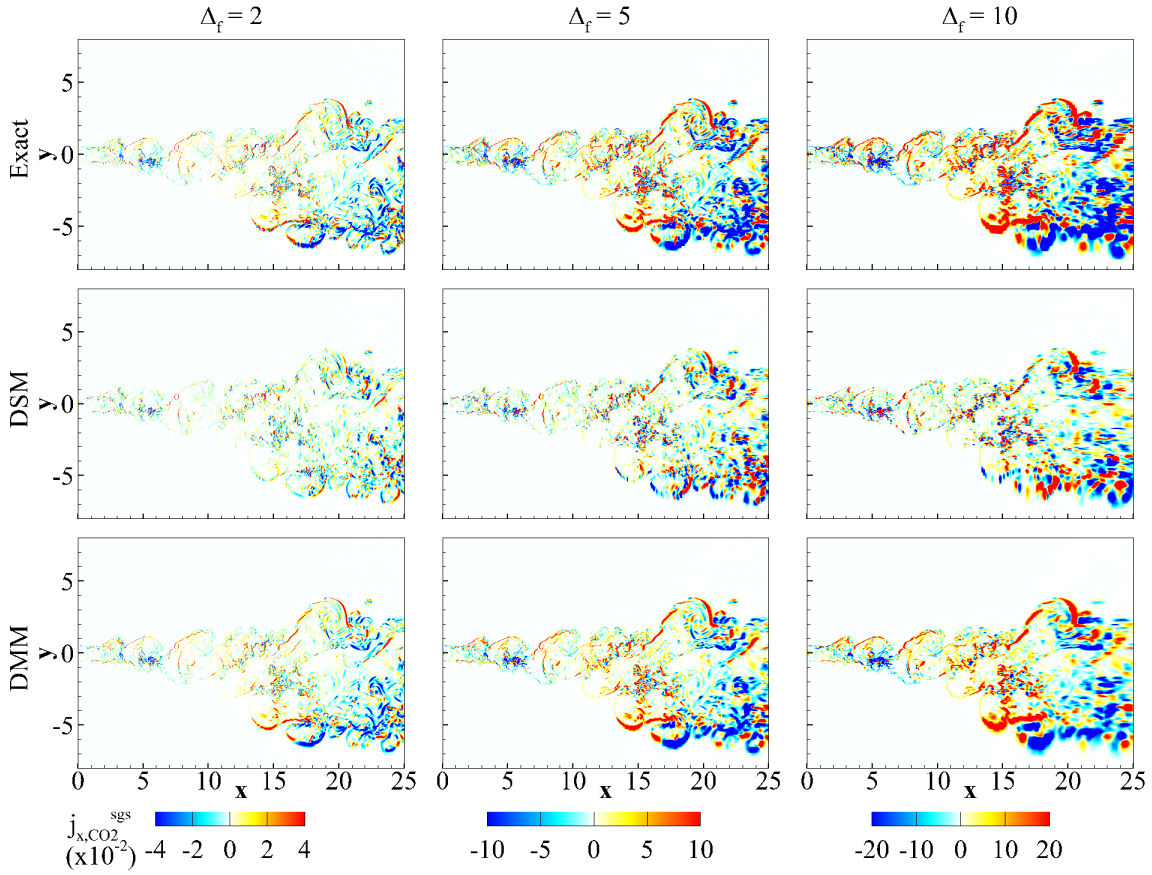

Figure 6.6 – Comparison of $\Phi_{CH4,x}^{sgs}$ distributions obtained from DNS (top row), and those modeled with dynamic Smagorinsky (middle) and dynamic mixed models (bottom) at different filter widths (column wise) (reacting case).

Table 6.4 – Correlation coefficients between exact and modeled subgrid enthalpy and species fluxes at different filter widths (reacting case).

	DSM			DMM		
Δ_f	**2**	**5**	**10**	**2**	**5**	**10**
Q_x^{sgs}	0.10	0.05	0.01	0.62	0.57	0.49
Q_y^{sgs}	0.12	0.10	0.01	0.54	0.38	0.30
$\Phi_{CH4,x}^{sgs}$	0.05	0.09	0.03	0.59	0.42	0.40
$\Phi_{CH4,y}^{sgs}$	0.09	0.09	0.03	0.50	0.35	0.24

6.4 Summary

A priori assessment of two representative SGS models for the conventional subgrid fluxes are undertaken using the DNS data generated for the non-reacting and reacting supercritical mixing layer cases. For the non-reacting case, the predictions from both models correlate reasonably with the exact subgrid fluxes. The dynamic mixed model performs significantly better than the dynamic Smagorinsky/eddy-diffusivity model. The latter is found to underpredict the magnitude of the subgrid fluxes. The performance of models decreases with filter widths, indicating that resolution limits must be considered for high-fidelity simulations. The dynamic mixed model provides reasonable performance even at high filter widths than the dynamic Smagorinsky model at low filter widths. For

LES of complex flows requiring affordable grid resolutions, the choice of dynamic mixed model would be advantageous to balance computational cost and accuracy.

For the reacting case, the performance of the dynamic Smagorinsky/eddy-diffusivity models are drastically reduced. The model predictions exhibit opposite trends at higher filter widths for the subgrid scalar fluxes. The dynamic mixed models provide reliable predictions with reasonable correlations for all the subgrid fluxes. The key strengths of the dynamic mixed model include the relaxation of the gradient diffusion assumption which enables the model to accurately capture complex physics, and the ability to achieve higher correlations at moderate and high filter widths. Based on this study, the dynamic mixed model is recommended over the eddy-viscosity/diffusivity-based models for practical reacting flows simulations requiring a tractable grid resolution. The reduced performance of the models in the reacting case compared to the non-reacting case also warrant further investigation to refine the physical basis of these models and adequately replicate complex phenomena at the subgrid scales.

CHAPTER 7. SUBGRID SCALE MODELING OF THE EQUATION OF STATE FOR SUPERCRITICAL MIXING

7.1 Overview

In Chapter 4 and Chapter 5, the subgrid density and subgrid enthalpy terms were identified as important contributing terms in the filtered equations that need to be accounted for. In particular, the subgrid density resulting from the filtered equation of state (EOS) appears in all the filtered conservation equations. There have been a few investigations on the relevance of the subgrid equation of state term for supercritical mixing. Selle et al. [99] found that the subgrid pressure term resulting from the filtered EOS is an important modeling consideration in supercritical mixing layers. They proposed a modeling approach for this term based on a Taylor series expansion, which showed moderate performance for a low filter width but the performance was poor at a higher filter width. Taskinoglu and Bellan [107] refined this approach and conducted *a posteriori* evaluation of their model in conjunction with the other models for the SGS convective flux terms. Borghesi and Bellan [100] have investigated a scale-similarity approach for modeling the subgrid pressure term and tested in a preliminary study [188]. Using 1D laminar premixed and non-premixed flamelets, Ribert et al. [104] investigated the subgrid EOS contributions for low- and high-pressure methane flames. They reported that the subgrid terms associated with the EOS were more prominent for CH_4-O_2 flames at high pressures where a real-fluid EOS is used. Lapenna and Creta [103] examined the errors in the modeling of the filtered EOS and other thermodynamic quantities using DNS of temporal mixing layers of transcritical and supercritical nitrogen jets. They proposed a presumed-PDF approach that showed good

improvement over the current no-model approach. A limitation of these works is that they considered temporal mixing layers at relatively low Reynolds numbers, which do not provide a complete description of turbulent flows at realistic conditions.

In this study, the DNS database developed in Chapter 4 is utilized to understand the role of subgrid turbulence effects in the filtered real-fluid EOS, and to investigate modeling approaches for subgrid closure that can be applied to practical LES simulations. Prior modeling approaches proposed in literature [105, 106] are investigated and refined in this work. In addition, novel modeling approaches are explored by extending the conventional dynamic and scale-similarity approaches. *A priori* analyses of the models are conducted and the performance, strengths and limitations of the models are discussed in detail.

7.2 No-model approach and the subgrid density

In the no-model approach, which is the currently used representation of the filtered EOS, the filtered density is directly evaluated using the filtered pressure $\bar{p}$, and the Favre-filtered temperature and species mass fractions $\left(\tilde{T}, \tilde{Y}_k\right)$ as

$$\rho\left(\widetilde{\boldsymbol{Q}}\right) = \frac{\bar{p}}{Z\left(\widetilde{\boldsymbol{Q}}\right)R\left(\widetilde{\boldsymbol{Q}}\right)\tilde{T}} \tag{7.1}$$

Using the DNS data, the subgrid density can be computed as

$$\rho^{sgs} = \rho\left(\widetilde{\boldsymbol{Q}}\right) - \overline{\rho(\boldsymbol{Q})} \tag{7.2}$$

Figure 7.1 shows the spatial distribution of the subgrid density for a filter factor $\Delta_f = 5$. This filter factor corresponds to an LES grid that is 5 times coarser than the DNS in each direction, which is appropriate for LES simulations. The subgrid density distribution qualitatively follows the turbulent mixing layer, with the magnitude of the terms peaking at the interface between the mixing layer and the LOX stream. In these regions, turbulence is generated through shear and the gradients of flow properties are highest, especially those of the scalar fields (temperature and species mass fraction). The oxygen stream is initially at a temperature of 120 K, which is below its critical temperature of 154.6 K, and hence the stream is in a pseudo-liquid state. Upon contact with the warmer gaseous methane stream, the LOX undergoes a process called pseudo-boiling [19] and transitions to a supercritical state. Within this transcritical regime there is a steep variation of density as a function of temperature and mixture composition. The turbulent scalar mixing results in a locally inhomogeneous mixture with varied thermodynamic states. These two effects in combination result in steep density gradients at the small scales that are filtered out in LES. The subgrid density is representative of the effect of density variations at the subgrid scales on the resolved density. Since density (or equivalently mass) is coupled with the other transport equations, the subgrid density plays an important role in representing the underlying convective transport of momentum, energy, and species fluxes at the subgrid level.

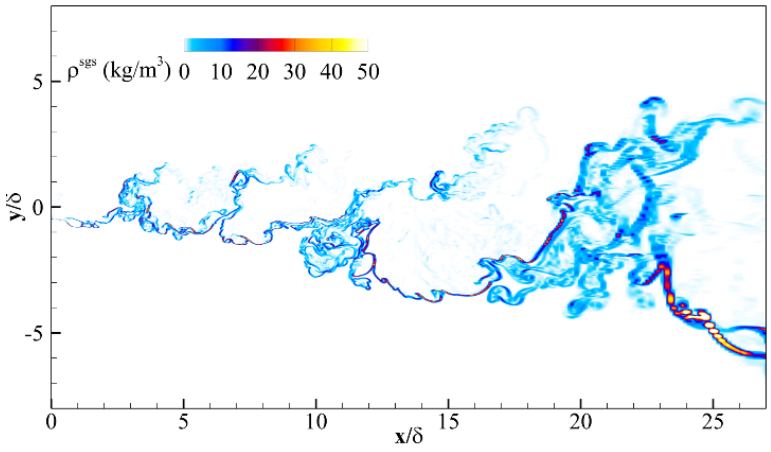

Figure 7.1 – Spatial distribution of the subgrid density computed using the DNS data, $\Delta_f = 5$.

The subgrid density is always positive for this case, implying that the modeled filtered density $\rho(\widetilde{\boldsymbol{Q}})$ is higher than the exact filtered density $\overline{\rho(\boldsymbol{Q})}$. This is also depicted in Figure 7.2 which shows a comparison between the exact filtered density and the modeled filtered density. In the no-model approach, the filtered density is computed using Favre-filtered variables. The Favre-filtering operator is a density-weighted filtering operator, implying that the filtered quantities are biased toward the denser species. Thus, the thermodynamic states represented by the Favre-filtered variables $(\tilde{T}, \tilde{Y}_k)$ are skewed towards the denser species, and the properties evaluated from these variables should also be closer to those of the denser species. In this case, the denser species is O_2, so the Favre-filtered primitive state variables $(\tilde{T}, \tilde{Y}_k)$ and the modeled filtered density are biased toward those of O_2. Bias toward the denser species naturally produces an overprediction of the modeled filtered density. Figure 7.3 shows the distribution of relative error in the modeled filtered density as a function of the mixture fraction. The relative error is defined as the subgrid density divided by the exact filtered density. The contribution of subgrid density

is low in the extreme rich and lean regions, where the effects of subgrid mixing and variation in scalar fields are minimum, and peaks in the intermediate mixture fraction regions, where the species mixing due to turbulence is in effect.

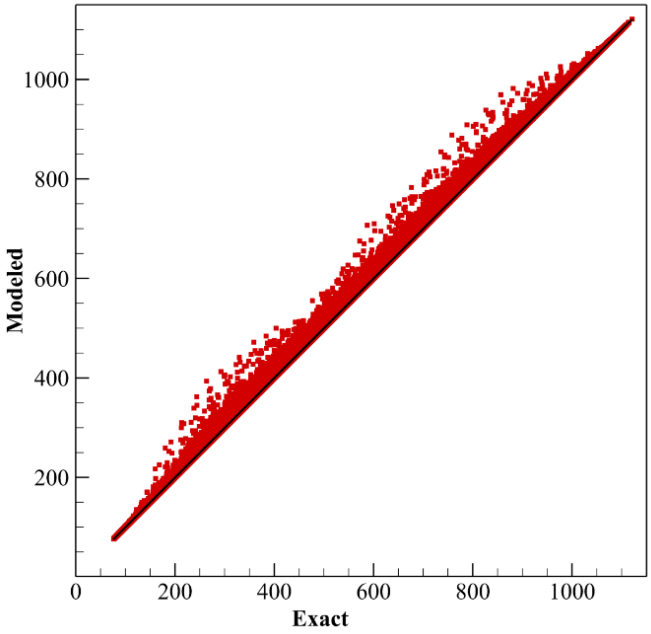

Figure 7.2 - Comparison of DNS-filtered density with filtered density evaluated using the no-model approach, $\Delta_f = 5$.

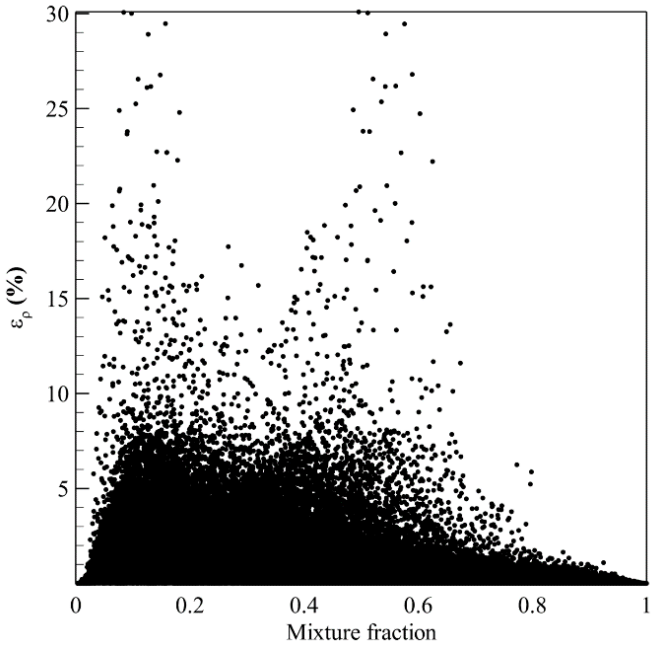

Figure 7.3 - Distribution of relative error (in percentage) in computed filtered density in the mixture fraction space, $\Delta_f = 5$.

7.3 Evaluation of filtered density in terms of Reynolds-filtered quantities

Considering the bias associated with the Favre-filtering operator, it would be natural to consider the representation of the filtered EOS in terms of Reynolds-filtered state variables. Ribert et al. [105] investigated a similar approach for computing the filtered pressure in the ideal gas EOS, by evaluating the EOS in terms of Reynolds-filtered species mass fractions instead of Favre-filtered mass fractions. The approach was proposed and analyzed for ideal, multi-component mixtures, and reasonable improvement was found. In this section, the extension of this approach for real-fluid, multi-component mixtures is investigated.

It is important to bear in mind the difference in complexities between the ideal-gas and real-fluid EOS; the non-linearities in the thermodynamic behavior of individual species and the resultant mixture are different, and the filtered EOS involves covariances of three variables (Z, T, Y_k) in the case of real-fluids (Equation (2.27)) instead of two variables (T, Y_k) in the case of ideal-gas EOS. In Ribert et al. [105], the filtered EOS was represented in terms of the Favre-filtered temperature and the Reynolds-filtered species mass fractions $(\tilde{T}, \bar{Y}_k)$. However, for the real-fluid EOS the inclusion of the compressibility factor Z, which itself is a function of the thermodynamic state, complicates the representation of an equivalent expression. An alternate representation is proposed in which the filtered density is modeled in terms of all Reynolds-filtered primitive variables. The model designated as the Reynolds-filtered model (RFM) can be expressed as

$$\overline{\rho(\boldsymbol{Q})} \approx \rho(\overline{\boldsymbol{Q}}) \tag{7.3}$$

where $\overline{\boldsymbol{Q}} = (\bar{p}, \bar{u}_i, \bar{T}, \bar{Y}_k)$ represents the set of Reynolds-filtered primitive variables. It should be noted that these quantities are not usually directly computed in LES. For *a priori* evaluation of the approach, we compute them from the DNS data. The representation in Equation (7.6) is not exact and a subgrid term must still be included. The goal here is to first evaluate if the approximation in Equation (7.6) provides an improvement over the current approximation for the filtered density.

7.4 Dynamic Gradient Model

Following the idea of functional modeling for the subgrid fluxes, such as the Smagorinsky model [50] or the Clark model [57], an analogous model of the subgrid density in terms of the gradients in the flow field is sought. The DNS data indicates that the subgrid density is prominent in regions of strong mixing where the gradients of scalar fields are large, suggesting a possible correlation between these quantities. Based on this observation and the physical significance of this quantity as discussed in Section 7.2 , a model form for the subgrid density is hypothesized which can be expressed as a function of the resolved gradients of density, temperature, and/or species mass fractions. To validate this hypothesis, the correlations of the subgrid density with gradients of density, temperature and species mass fraction are computed using the filtered DNS data. It is found that density gradient has the highest correlation coefficient (around 65%) with subgrid density, while temperature and species mass fraction gradients have about 39% and 30% correlations respectively. The pressure variation in the flow field is less than 1% of the reference pressure, and the density variation corresponding to this pressure variation is negligible. The effect of pressure gradient is not expected to contribute significantly to the subgrid term here and is not included in our modeling approach, but naturally it would need to be included for flows involving strong pressure gradients, such as shocks.

Based on the high correlation, a model form analogous to the Smagorinsky model is proposed where the subgrid density is expressed as a function of the local density gradient magnitude and the local LES filter size through a model coefficient C as

$$\rho^{sgs} = C\bar{\Delta}\left|\nabla\rho(\widetilde{\boldsymbol{Q}})\right| = C\bar{\Delta}\,\rho_g(\widetilde{\boldsymbol{Q}}) \tag{7.4}$$

Here the notation $\rho_g(\boldsymbol{Q}) = |\nabla\rho(\boldsymbol{Q})|$ is used as a shorthand to represent the magnitude of the density gradient, and $\bar{\Delta}$ denotes the local filter (grid) scale. The model expression above can also be derived following arguments of dimensional analysis or by filtering a Taylor series expansion of density around the LES computed density and truncating second order terms. Model forms including the gradients of the temperature and species mass fractions were also investigated, but the difference from the baseline model was found to be minimal [189].

The model coefficient in Equation (7.4) can be evaluated from the DNS data using a least-square error minimization as in linear regression analysis, by minimizing the square of the difference between the exact and modeled subgrid term. The value of C was computed using flow fields at different time instants and considering data from different subsets of the domain that included only the core of the mixing layer, and the value was consistently found to be close to $C \approx 21.6$. Using this coefficient value, the model correlation with the exact value is found to be around 65%. For perspective, the Smagorinsky model has been shown to have a correlation of 20% or less for the subgrid stresses and energy fluxes, while that of dynamic models is about 60-70% [81]. In sum, the proposed model for the EOS offers reasonable performance, while also being tractable in an LES simulation.

A priori analysis of the model performance was reported in a previous work [189]. Improvement in accuracy of the filtered density was achieved over the no-model approach,

especially in the peak error region near the stoichiometric mixture fraction, where the gradients and turbulent mixing are the highest. The subgrid density was, however, over-predicted in regions away from the mixing layer, where the subgrid density is negligible. This trend is attributable to the use of a globally determined model coefficient that does not consistently represent the subgrid scale physics in different regions of the flowfield, especially in regions of low turbulent mixing. The same limitation has been recognized with the constant-coefficient Smagorinsky model in transitional and near-wall regions. Another limitation of this modeling approach is in the generalizability of the model coefficient. Since physical reasoning cannot be presented for this value at this point, it must be assumed that the value of the coefficient for a different species mixture and different operating conditions might be different. It is speculated that the value of this coefficient might be dependent on the thermodynamic behavior of the species mixture through the EOS, but this point needs further investigation.

To overcome the limitations of the constant-coefficient model, a dynamic modeling approach for the model coefficient is sought. Using the gradient model (Equation (7.4)) as a baseline, a dynamic model can be derived following Germano's approach [53]. Dynamic models derived using Germano's identity have demonstrated reasonable success as compared to constant-coefficient models in providing a more physical representation of subgrid scale physics and reproducing the correct limiting behavior in different flow regions. In a dynamic model, the scale-similarity assumption is applied to evaluate the model coefficient locally in space and time according to the local filtered flow features. The scale-similarity hypothesis assumes that the structure of turbulence and the interscale processes between the smallest resolved scale (grid-filter scale) and the slightly larger

scales (test-filter scale) are similar to those between the smallest resolved scale and the largest unresolved scale. An explicit filtering operation is applied to the LES solution at a slightly larger scale than the grid-filter width, called the test-filter scale, producing a test-filtered field. The model coefficient is then obtained by relating the subgrid term at the grid-filtered (LES) and the test-filtered solutions, at each point in space and time.

Considering subgrid density as the unclosed term of interest,

$$\rho^{sgs} = \rho(\widetilde{\boldsymbol{Q}}) - \overline{\rho(\boldsymbol{Q})} \approx C\bar{\Delta}\,\rho_g(\widetilde{\boldsymbol{Q}}) \tag{7.5}$$

At the test-filtered level,

$$\rho^{sgs,t} = \rho\left(\widehat{\widetilde{\boldsymbol{Q}}}\right) - \widehat{\overline{\rho(\boldsymbol{Q})}} \tag{7.6}$$

where the top-hat symbol represents a filtered quantity at the test-filtered level. We then define the Leonard term as

$$\begin{aligned} \mathcal{L}_\rho = \rho^{sgs,t} - \widehat{\rho^{sgs}} &= \left(\rho\left(\widehat{\widetilde{\boldsymbol{Q}}}\right) - \widehat{\overline{\rho(\boldsymbol{Q})}}\right) - \left(\widehat{\rho(\widetilde{\boldsymbol{Q}})} - \widehat{\overline{\rho(\boldsymbol{Q})}}\right) \\ &= \rho\left(\widehat{\widetilde{\boldsymbol{Q}}}\right) - \widehat{\rho(\widetilde{\boldsymbol{Q}})} \end{aligned} \tag{7.7}$$

This can be expressed in terms of the gradient model approximation, following the principle of scale similarity, as

$$\rho^{sgs,t} - \widehat{\rho^{sgs}} = C\hat{\bar{\Delta}}\,\rho_g\left(\widehat{\widetilde{\boldsymbol{Q}}}\right) - \widehat{\overbrace{C\bar{\Delta}\,\rho_g(\widetilde{\boldsymbol{Q}})}}$$

$$= C\hat{\bar{\Delta}}\,\rho_g\left(\hat{\tilde{\boldsymbol{Q}}}\right) - C\bar{\Delta}\,\widehat{\rho_g(\tilde{\boldsymbol{Q}})} = C\bar{\Delta}\left[\frac{\hat{\bar{\Delta}}}{\bar{\Delta}}\,\rho_g\left(\hat{\tilde{\boldsymbol{Q}}}\right) - \widehat{\rho_g(\tilde{\boldsymbol{Q}})}\right] \tag{7.8}$$

$$= C\bar{\Delta}\mathcal{M}_\rho$$

where $\mathcal{M}_\rho = \frac{\hat{\bar{\Delta}}}{\bar{\Delta}}\,\rho_g\left(\hat{\tilde{\boldsymbol{Q}}}\right) - \widehat{\rho_g(\tilde{\boldsymbol{Q}})}$.

Each of the terms in the expressions for $\mathcal{L}_\rho$ and $\mathcal{M}_\rho$ can be evaluated at the test-filter level using the LES resolved flow variables. Combining Equations (7.7) and (7.8), and following Lilly's least-squares approach [146], the coefficient in the gradient model can be obtained as

$$C\bar{\Delta} = \frac{\langle \mathcal{L}_\rho \mathcal{M}_\rho \rangle}{\langle \mathcal{M}_\rho \mathcal{M}_\rho \rangle} \tag{7.9}$$

The angular brackets indicate an averaging operation, which is usually done to avoid unphysical oscillation of the model coefficient. For the dynamic eddy-viscosity models for the subgrid convective fluxes, a summation over the tensor or vector components, along with spatial averaging in homogeneous directions, is adopted to overcome this issue [53, 146] whenever a homogeneous direction is present. In this case, due to lack of homogeneity in the flow and due to the coefficient ascribed to a scalar quantity, such a procedure cannot be adopted. An alternative is to use a dynamic localization procedure [190] or local averaging [147]. In this case, we perform a local averaging over the adjacent neighboring cells, following the approach by Zang et al. [147] With the dynamic formulation, the gradient model generalizes to

$$\rho^{sgs} = \frac{\langle \mathcal{L}_\rho \mathcal{M}_\rho \rangle}{\langle \mathcal{M}_\rho \mathcal{M}_\rho \rangle} \left| \nabla \rho(\widetilde{\boldsymbol{Q}}) \right| \tag{7.10}$$

The dynamic gradient model (DGM) formulated in Equation (7.10) is parameter-free, except for the choice of the ratio between the grid- and test-filtered levels $\hat{\bar{\Delta}}/\bar{\Delta}$. A choice of test-filter width which is twice the grid filter width, i.e. $\hat{\bar{\Delta}} = 2\bar{\Delta}$, which is widely used for dynamic models of the subgrid fluxes [53, 147], is adopted in the present study. For the *a priori* study, the test-filtering is applied only on the filtered LES solution, as would be done in an LES simulation. For the test-filtering, a discrete box filter is used, employing trapezoidal rule and quadratic interpolation of variables within the test-filter volume. The procedure accounts for the presence of non-uniform and non-orthogonal cells. With the modeled subgrid density, the filtered density is then evaluated from Equation (7.2) as $\overline{\rho(\boldsymbol{Q})} = \rho(\widetilde{\boldsymbol{Q}}) - \rho^{sgs}$.

7.5 Scale-Similarity Model

The principle of scale-similarity was introduced by Bardina [55] and has been applied to directly model the subgrid stress tensor [56]. Cook and Riley [70] have also used this principle to model the subgrid scalar variance. Following this principle, a model for the subgrid density is formulated as

$$\rho^{sgs} \approx C_{ss} \left(\rho\left(\widehat{\widetilde{\boldsymbol{Q}}}\right) - \widehat{\rho(\widetilde{\boldsymbol{Q}})} \right) \tag{7.11}$$

where the quantities in the model are evaluated at the test-filter level based on the resolved variables at the LES grid level. This represents the subgrid density between the test-filter and grid-filter levels. The model coefficient C_{ss} can be taken to be unity for the sake of simplicity, as done by Cook and Riley [70]. For $C_{ss} = 1$, it is interesting to note that the scale-similarity model is the same as the term $\mathcal{L}_\rho$ in the dynamic gradient model. In fact, when the density gradients at the grid-scale and test-filter scale are equal, $\mathcal{M}_\rho$ would be equal to $\rho_g(\widetilde{\boldsymbol{Q}})$, and the subgrid density computed with the scale-similarity model would be equal to that computed by the dynamic gradient model.

A more rigorous method is to compute the model coefficient in a dynamic manner. For this, the model is modified such that the test filter is equal to the LES filter, similar to Bardina's model for the subgrid stress [55].

$$\rho^{sgs} \approx C_{ds}\left(\rho\left(\widetilde{\widetilde{\boldsymbol{Q}}}\right) - \overline{\rho(\widetilde{\boldsymbol{Q}})}\right) \tag{7.12}$$

Following the dynamic modeling approach, the model term $\mathcal{M}_\rho$ can be written as

$$\mathcal{M}_\rho^s = C_{ds}\left\{\left(\rho\left(\widehat{\widetilde{\widetilde{\boldsymbol{Q}}}}\right) - \widehat{\overline{\rho\left(\widetilde{\widetilde{\boldsymbol{Q}}}\right)}}\right) - \widehat{\left(\rho\left(\widetilde{\widetilde{\boldsymbol{Q}}}\right) - \overline{\rho(\widetilde{\boldsymbol{Q}})}\right)}\right\} \tag{7.13}$$

and the Leonard term is as given in Equation (7.7). The dynamic scale-similarity model is formulated as

$$\rho^{sgs} = \frac{\langle \mathcal{L}_\rho \mathcal{M}_\rho^s \rangle}{\langle \mathcal{M}_\rho^s \mathcal{M}_\rho^s \rangle}\left(\rho\left(\widetilde{\widetilde{\boldsymbol{Q}}}\right) - \overline{\rho(\widetilde{\boldsymbol{Q}})}\right) \tag{7.14}$$

where the test-filtering and spatial averaging procedures as in the dynamic gradient model are adopted. In this paper, we report the results from the scale-similarity model with $C_{ss} = 1$. The dynamic scale-similarity model was also evaluated, and the differences were found to be minimal.

7.6 Presumed filtered density function approach

The filtered density function (FDF) is an analog of the probability density function (PDF), and is used in LES to represent the PDF of the subgrid scale fluctuations [131]. Closure of subgrid terms using the FDF approach has been explored in several studies, including for conserved scalars in combustion problems [74, 191, 192]. Recently, Lapenna and Creta [103] investigated the application of a presumed beta-PDF for the evaluation of filtered density and specific heat under transcritical and supercritical conditions. Using DNS of temporal N_2 jets, they showed good comparison of the DNS-extracted PDF to the presumed beta-PDF. In their studies they considered relatively low Reynolds number jets and a single species, with the density computed as a function of the temperature alone. In *a posteriori* studies of reacting flows [106], they implemented the EOS evaluation within the flamelet model framework. The density was evaluated based on the mixture fraction and its variance, which uniquely determine the species composition and temperature for a given value of scalar dissipation rate.

Here the presumed-FDF approach is investigated for the CH4-LOX mixing case, with corrections for two discrepancies identified with the original approach by Lapenna and Creta [103]. First, with the assumption of adiabatic mixing, the relation between

temperature and species composition is not linear. Moreover, the DNS data suggests that the fluctuations in temperature and species composition does not necessitate a unique mapping between the two quantities, since the governing transport processes are different. Therefore, fluctuations in both scalar quantities must be considered separately for the determination of the filtered density at a given computational cell. It is assumed that the fluctuations in the temperature and mixture fraction are statistically independent, and therefore the joint FDF of the density can be represented as the product of the marginal FDFs with respect to the temperature and mixture fraction z. That is, $P(T, f) = P(T)P(f)$. The subgrid scale fluctuations in pressure are neglected since these fluctuations are much less than 1%, and the effect of these fluctuations on the density is negligible. However, for other cases involving larger subgrid pressure fluctuations, their effect may need to be accounted for.

Second, it is noted that the presumed beta-PDF form for the scalars should be attributed to the subgrid scale Favre-FDF (not the FDF) when the moments of the scalars are expressed as Favre-filtered quantities [193]. The Favre-filtered FDF $\tilde{P}(\psi)$ is a density-weighted form of the FDF $P(\psi)$ [194] representing the density-weighted subgrid fluctuation. The Favre-FDF is used to evaluate a Favre-filtered quantity

$$\tilde{\phi}(\psi) = \int_{-\infty}^{\infty} \phi(\psi')\tilde{P}(\psi'|\psi)d\psi' \tag{7.15}$$

From the definition of Favre-filtering, $\bar{\rho}\widetilde{\rho^{-1}} = \overline{\rho\rho^{-1}} = 1$. Therefore, the consistent way to evaluate the filtered density is

$$\bar{\rho} = \frac{1}{\widetilde{\rho^{-1}}} = \left[\int_0^1 \int_0^\infty \frac{1}{\rho(T,f)} \tilde{P}(T,f) dT df \right]^{-1} \tag{7.16}$$

The joint scalar Favre-FDF $\tilde{P}(T,f)$ is assumed to be the product of the marginal Favre-FDFs of the two scalars. Here, the species composition is considered in terms of the mixture fraction f, which for the LOX-CH_4 mixing case corresponds to the mass fraction of CH_4.

Each of the marginal Favre-FDF forms is presumed to follow a beta-PDF distribution given as

$$\tilde{P}_{beta}(\xi) = \frac{\Gamma(\alpha+\beta)}{\Gamma(\alpha)\Gamma(\beta)} \xi^{\alpha-1}(1-\xi)^{\beta-1} \tag{7.17}$$

The shape parameters of the pdf (α, β) are computed based on the Favre-filtered mean $(\tilde{\xi})$ and subgrid variance $(\widetilde{\xi''^2})$ of the scalar fields.

$$\alpha = \tilde{\xi}\left(\frac{\tilde{\xi}}{\widetilde{\xi''^2}} - 1\right), \beta = \left(1-\tilde{\xi}\right)\left(\frac{\tilde{\xi}}{\widetilde{\xi''^2}} - 1\right)$$

Since the beta-pdf distribution is defined over the interval [0,1], the temperature is normalized as $T^* = \left(T - T_{o_2}\right)/(T_{CH_4} - T_{o_2})$. The joint Favre-FDF is then given as $\tilde{P}(T^*, f) = \tilde{P}_{beta}(T^*) \times \tilde{P}_{beta}(f)$, and the filtered density is evaluated as

$$\bar{\rho}\left(\tilde{T}, \tilde{f}\right) = \frac{1}{\widetilde{\rho^{-1}}} = \left[\int_0^1 \int_0^1 \frac{1}{\rho(T^*,f)} \tilde{P}(T^*,f) dT^* df \right]^{-1} \tag{7.18}$$

For implementation, the density as a function of the scalar field (T^*, f) is computed and stored on a grid over the interval $(T, f) \in \left[T_{o_2}, T_{CH_4}\right] \times [0,1]$ with $\Delta T = 1\ K$ and $\Delta f = 0.01$. For *a priori* analysis, the filtered and subgrid scalar variance values are computed from the DNS database, and the corresponding FDF and integrals are evaluated at each LES cell to calculate the filtered density according to Equation (7.18).

7.7 *A priori* assessments of model performance

To evaluate the effectiveness and usefulness of the proposed modeling approaches, several different metrics are considered. Figure 7.2 shows a comparison of the filtered densities computed from the DNS database (exact) and those evaluated using the no-model approach, and Figure 7.4 shows the same comparison for the filtered densities evaluated with the modeling approaches described in the previous sub-sections. As discussed in Section 7.2, the filtered density is overpredicted by the no-model approach, in which the density is computed directly using the Favre-filtered temperature and species mass fractions. On the other hand, the density computed based on the Reynolds-filtered variables underpredicts the filtered density. The density computed using Reynolds-filtered variables does not contain information pertaining to the interactions (covariances) between the resolved primitive variables at the subgrid level and therefore, excludes the effect of subgrid mixing in the computed density. The addition of these subgrid effects through a subgrid term might improve the prediction. For example, Ribert et al. [105] use a scale-similarity based model to account for this term. However, an analogous term could also be considered based on the Favre-filtered quantities, as in the scale-similarity model in Section

7.5. This would also eliminate the need for an additional step to compute the Reynolds-filtered variables from the corresponding Favre-filtered variables and therefore reduce the overall computational cost of the model.

The dynamic gradient and scale-similarity models show overall improvements to the modeled filtered density. The subgrid density and the filtered density evaluated with the dynamic gradient model exhibit a slight scatter in the predicted values; the scatter is worse in the absence of spatial averaging. A subgrid model in principle represents the statistical effect of unresolved scales and should only be evaluated in a statistical sense. Non-statistical evaluation of the model coefficient results in over-specification and oscillation of the value in certain regions of the flows, and statistical averaging is thus required. In this study, the local spatial averaging was confined to a three-point stencil in each spatial direction, or a total of 9 cells in the vicinity of an LES cell for 2D. It is possible that this averaging might not be sufficient for the filter size considered. There is also a concern regarding the evaluation of the test-filter across the transcritical interface between the two streams, which presents a sharp density gradient in the mean field. When the filter operator is applied in these regions, information on the density gradient is incorrectly represented as a fluctuation associated with subgrid scale turbulence. This contribution could be more significant than realistic subgrid fluctuations, causing an inconsistency with modeling approaches which inherently assume that all subgrid fluctuations are turbulent in nature. This subject has been broached in the context of compressible flows with shocks [195, 196], but it is still in the preliminary stage and the issues are not fully understood. Test-filtering is found to smear the density gradient, resulting in incorrect prediction of the test-filtered density gradient magnitude, $\widehat{\rho_g(\tilde{Q})}$ in Equation (7.8). The associated errors

feed into the denominator $\mathcal{M}_\rho$ term in the model coefficient, which manifest in the form of oscillations of the model coefficient. The scale-similarity model, on the other hand, does not exhibit this level of scatter, and the overall trend seems to be better than the gradient model. Results using the scale-similarity model with $C_{ss} = 1$ and the dynamic variant were found to exhibit similar performance with nominal differences.

The filtered density modeled using the presumed FDF approach matches very closely with the exact filtered density, with almost negligible deviation. The original formulation by Lapenna and Creta [103] was also compared, and it was found that the results obtained with the model form proposed in Section 7.6 were more accurate, owing to the mathematical consistency of the formulation.

The relative error in the filtered density evaluated with different models is presented as a distribution in the mixture fraction space in Figure 7.5. The relative error is defined as the difference between the modeled and exact filtered densities normalized by the exact filtered density. These are compared with the corresponding distribution for the no-model approach shown in Figure 7.3. The error in the filtered density evaluated with the Reynolds-filtered model is of the same magnitude and qualitative distribution as the no-model approach, with the difference that the error is of the opposite sign due to under-prediction. This is contrary to the findings of Ribert et al. [105] for the filtered ideal gas EOS. The discrepancies are indicative of the complexities associated with the non-linear nature of the real-fluid EOS and the important role of subgrid interaction among turbulent mixing and thermodynamics in the supercritical regime. With the dynamic gradient and scale-similarity models, the magnitudes of the errors are decreased. Most of the cells display an error close to zero with a narrow error margin. The remaining scatter in the

figures represents data from cells where the modeled filtered density is inaccurate. The subgrid density predicted by the models is sometimes over-estimated, causing the modeled filtered density to be lower than the exact value, as seen by the points with negative error. This is attributed to the oscillation of the model coefficient in some cells. The presumed-FDF model shows the most improvement, with the modeling errors confined to less than 2%. The remaining errors could be a result of the numerical errors with the discrete representation of the integral, or deviations from the presumed FDF form, or a combination.

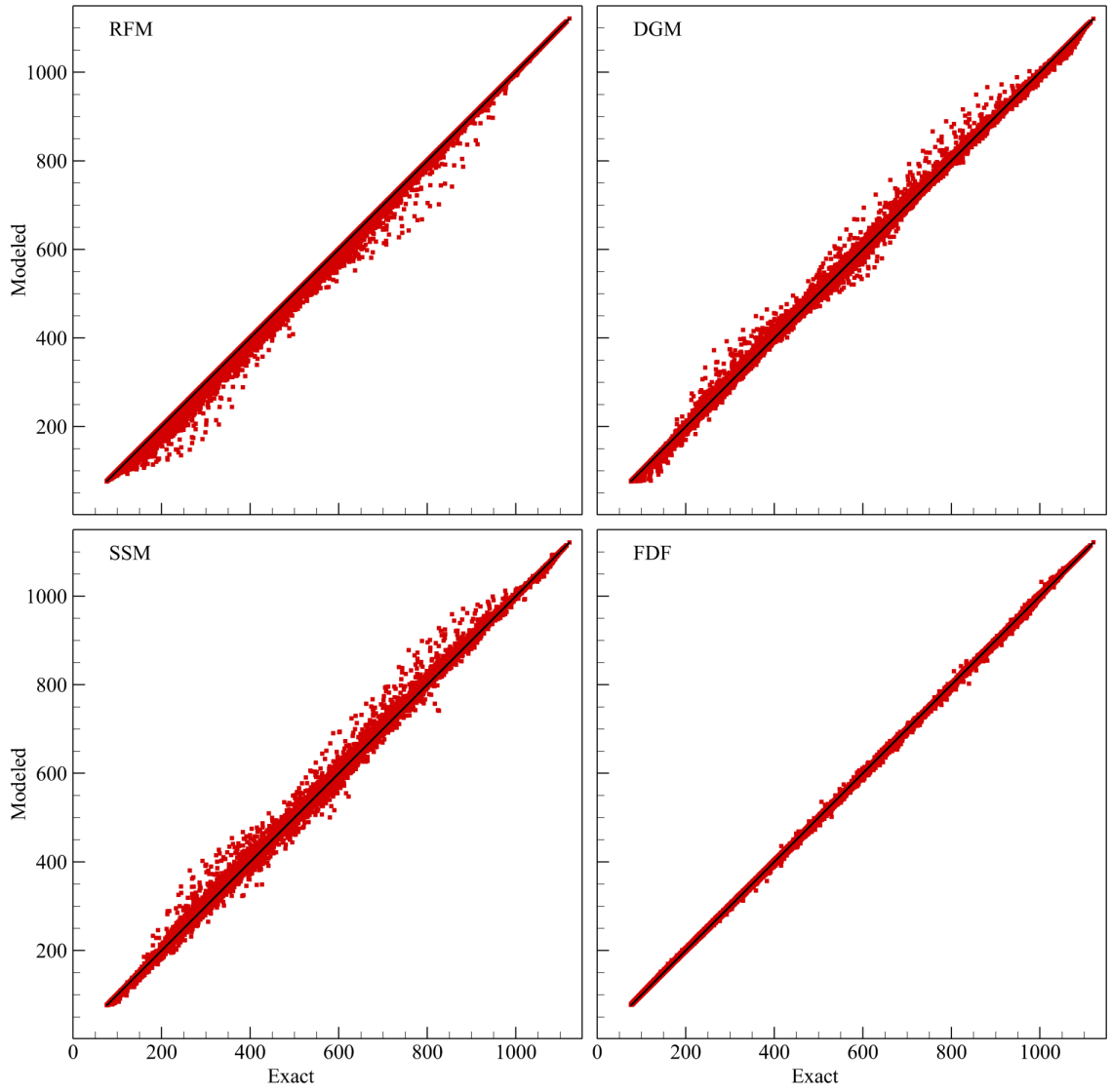

Figure 7.4 - Comparison of DNS-filtered density with filtered density evaluated using different modeling approaches, $\Delta_f = 5$.

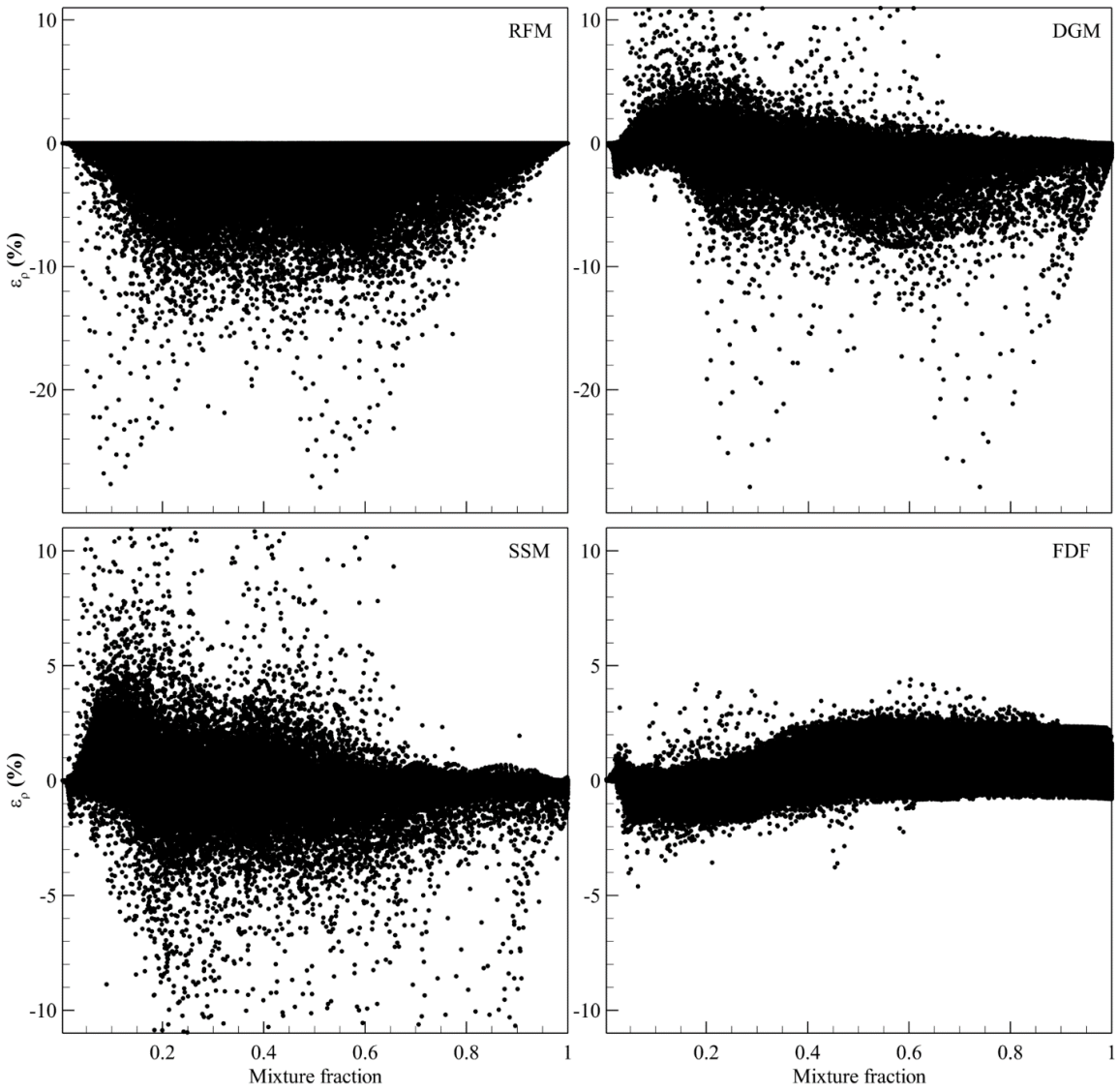

Figure 7.5 - Distribution of relative error (in percentage) in filtered density evaluated from different models as a function of mixture fraction, $\Delta_f = 5$.

The performance of the models are further quantified using two metrics - correlation between the exact subgrid density and the modeled subgrid density, and the L^2 norm of the error in the modeled filtered density. These performance metrics are presented in Table 7.1 for the moderate and coarse filter widths. The correlation coefficient between the exact and modeled terms is computed using the standard relation [81]. For comparison,

the subgrid density for the Reynolds-filtered model and the presumed-FDF model are defined as the difference between the filtered density with the no-model approach $\rho(\widetilde{\boldsymbol{Q}})$ and the filtered density evaluated with the corresponding model. The error in the modeled filtered density is the difference between the exact filtered density (DNS) and the filtered density calculated using a particular model. The L^2 norm of the error is computed over all the cells in the domain and normalized by the total number of cells. With increase in filter width, the modeling errors are increased significantly. All the proposed modeling approaches show improvement over the no-model approach with respect to reduction in the error norm. This performance ranking is consistent with the inferences from the previous metrics. The improvements however become less effective at the coarser resolution. The presumed-FDF approach shows the best performance in terms of the error norm as well as the correlation coefficient of the model prediction. The reduction in error at coarser resolution is also significant compared to the other models. The correlation coefficient of the dynamic gradient model and scale-similarity model are relatively lower but are still comparable to those obtained for the conventional SGS models.

There are advantages and limitations associated with each modeling approach proposed in this work. There remain outstanding issues with the dynamic gradient and scale-similarity modeling approaches regarding the application of test-filtering, and these concerns also apply to the currently used dynamic eddy-viscosity models. However, the overall improvement in the predictions is encouraging for further refinement of these models. A consistent technique for statistical averaging of model parameters and evaluation of the test-filter is expected to improve the dynamic gradient model performance further.

Table 7.1 – Correlation coefficients between the exact and modeled subgrid density, and the L^2 norm of error in the modeled filtered density for different models.

Model	Correlation coefficient		L^2-error	
	$\Delta_f = 5$	10	5	10
No-model			11.3	76.15
Reynolds-filtered	-0.94*	-0.95*	6.76	52.82
Dynamic Gradient	0.78	0.70	4.43	37.39
Scale-similarity	0.75	0.63	4.75	43.39
Presumed FDF	0.97	0.97	1.64	6.44

The presumed-FDF model is a mathematically consistent approach and shows the best performance among all the models investigated in this work. A limitation with this approach, however, is that it requires additional models for estimating the subgrid scale variances of the temperature and species fields. To evaluate these quantities, modeled transport equations must be solved. Alternatively, a scale similarity approach [70] or a scaling law [197] can be used. However, either of those approaches is expected to introduce additional model uncertainties and errors in the framework that are equivalent to the deficiencies in the dynamic model discussed earlier. Furthermore, the evaluation of the integrals in the model imposes additional CPU and memory costs. This is especially relevant for transcritical mixing and combustion cases, where a fine-grained density mapping in the thermodynamic state space is required to account for the strong variations

in the density. This could be partially alleviated by pre-computing and storing the integrals in a tabulated framework, as is done in the use of flamelet models for combustion [198, 199].

7.8 Summary

The inconsistencies and errors associated with the representation of the filtered EOS in the LES framework are investigated in the context of supercritical mixing. It is recognized that the direct evaluation of the filtered density (or pressure) based on the Favre-filtered thermodynamic state variables does not represent the subgrid scale interactions between the thermodynamics and turbulent mixing, resulting in errors in the computed filtered density. The magnitudes of the density-weighted Favre-filtered variables are biased towards those of the denser states at the subgrid level. This results in overprediction of the filtered density computed based on these quantities for the LOX-GCH4 mixing configuration considered in this study. Different modeling approaches were proposed to account for these effects and to obtain an accurate estimate of the filtered density using the real-fluid EOS. The models were evaluated using different performance metrics to assess the accuracy in modeling the filtered density as compared to that obtained from the DNS. The Reynolds-filtered model, in which the EOS is evaluated based on the Reynolds-filtered state variables rather than the Favre-filtered variables, does not provide any improvement over the no-model approach.

Two modeling frameworks are proposed extending the approaches used for modeling the subgrid convective flux terms. First, a gradient model is proposed as a

functional model analogous to the Smagorinsky model. The formulation is based on the qualitative and quantitative correlation of the subgrid density to the resolved density gradient magnitude in the flow. To evaluate the model coefficient, a dynamic modeling procedure is formulated by extending the ideas of Germano's identity, rendering the dynamic gradient model. Likewise, a scale-similarity model is proposed to directly evaluate the subgrid density. Both of these models are found to show improvement in modeling the filtered density and overall reduction in errors. Some errors persist due to unphysical variation of the model coefficient stemming from evaluation of the test-filtering across sharp density gradient regions and lack of sufficient statistical averaging. These issues are known to exist even for compressible, ideal-gas flows and require further refinement. Lastly, a PDF-based approach is proposed, assuming a beta-PDF form of the Favre-FDF to model the subgrid scale fluctuations of the temperature and species composition. This model showed the best correlation of the filtered density with the DNS data and the smallest modeling errors. This approach requires additional information regarding the subgrid variances of the temperature and species mass fractions, which entails supplementary models for these quantities.

While the *a priori* assessments in this work are done using 2D DNS data, the model formulations are founded on physical principles that are well-established in the turbulence modeling literature and are thus expected to be valid even for realistic 3D turbulence. Assessment of the models using 3D DNS data and *a posteriori* LES validations are warranted whenever such studies are computationally feasible.

CHAPTER 8. CONCLUSIONS AND FUTURE WORK

8.1 Conclusions

The overarching goal of this dissertation is to address the deficiencies and uncertainties surrounding the extension of the current large eddy simulation (LES) framework to application of flows at high-pressure, supercritical conditions. The specific objectives identified in Chapter 1 provided a progressive pathway for this endeavor. These objectives are revisited, and a summary of the important milestones and conclusions achieved through this dissertation are outlined as follows.

The first objective of this dissertation was to determine a consistent theoretical framework for the LES of a supercritical multi-species flow. A systematic derivation of the filtered conservation equations that govern the evolution of the large-scale flow is conducted, following a detailed background of the fundamental constitutive relations and the filtering operation adopted in LES. The derived system of equations presented in Chapter 2 is devoid of the usual assumptions and simplifications that are invoked under the low-pressure incompressible or compressible flow regimes and is thus applicable for flows under all thermodynamic regimes. The derived framework highlights the presence of several new unclosed terms that are not considered in the conventional LES framework. These terms represent important effects of the subgrid scale physics on the dynamics of the resolved large scales. The non-ideal, non-linear thermodynamics under these conditions, and their impact on the representation of the filtered convective and diffusive fluxes are discussed from fundamental and mathematical viewpoints. Based on these discussions, it is postulated that the representation of the filtered thermodynamic and transport fluxes are

no longer trivial as is considered under incompressible or weakly compressible flows at low pressure conditions.

The second objective was to quantify the different terms in the derived filtered equations in order to identify the terms that are to be considered relevant for modeling, and those that can be neglected under the conditions of interest. To enable such a study, direct numerical simulations (DNS) are conducted for the case of a spatially evolving mixing layer comprised of co-flowing methane and liquid oxygen streams, at an operating pressure of 100 bar. This fundamental configuration is representative of propellant injection in liquid rocket engines. An important merit of this work that distinguishes it from previous studies, is that it considers a spatially evolving, inhomogeneous turbulent flow at realistic Reynolds numbers corresponding to practical systems. DNS datasets are generated for two cases – 1. a non-reacting binary-species case, and 2. a reacting multi-species case, to investigate the effects of multi-species mixing and heat release on the interactions between turbulence and thermo-chemical processes at the subgrid level, and their combined effect upon the resolved scale flow dynamics.

A priori analyses of the terms in the filtered equations are conducted using the generated DNS datasets. First, an order of magnitude analysis is performed to quantify the various terms and identify the leading terms in the governing equations. The relative magnitudes of the subgrid terms with respect to their corresponding resolved scale terms are then quantified. Parametric analyses are conducted as a function of filter widths to derive useful trends for LES. Based on these analyses, two new sets of subgrid terms are shown to be relevant for the non-reacting and reacting cases. These are the subgrid

convective fluxes associated with the thermodynamic quantities (density and enthalpy), and the subgrid diffusive transport fluxes resulting from the non-ideal transport properties.

In the non-reacting case, the subgrid convective fluxes associated with the subgrid density/enthalpy are found to be comparable in magnitude with respect to the leading order resolved convective fluxes, and even greater than the conventional subgrid fluxes in most cases. The magnitudes of these terms are shown to be highest in the transcritical interface of the mixing layer with the LOX stream, where strong density gradients occur. The subgrid diffusive fluxes are among the lowest order terms in the respective governing equations. However, the magnitudes of these terms are comparable to the resolved diffusive fluxes, especially at higher filter widths. The physical significance of these terms requires further investigation. The differences between Favre-filtered and Reynolds-filtered state variables are quantified. Significant deviations, which increase with filter width, are found for the thermodynamic state variables (temperature and species mass fractions). The associated errors in representation of filtered thermodynamic and transport properties are also shown to be significant especially at coarser resolutions.

In the reacting case, the contributions from the two sets of subgrid terms are increased compared to the non-reacting case. The subgrid terms are found to most significant in the primary and secondary flame regions where large density gradients occur. The deviations between Favre- and Reynolds-filtered thermodynamic state variables, and errors in computation of filtered thermodynamic/transport properties are also increased, and the distribution of these errors are much more complex compared to the non-reacting case.

The third objective of this dissertation was to assess the performance of existing subgrid modeling approaches employed for the conventional subgrid fluxes. The study demonstrates the superior performance of the dynamic mixed model over the dynamic Smagorinsky model. Although the accuracies of both models decrease with increasing filter widths, the performance of the dynamic mixed model at higher filter widths is still better than the performance of the dynamic Smagorinsky model at low filter widths. The dynamic Smagorinsky model is also found to perform worse in the reacting case. It is concluded that the eddy-diffusivity hypothesis is not strictly valid under complex flow conditions. Based on the study, the dynamic mixed model is recommended for practical LES of flows in this regime. It is also considered that deficiencies in the model arise because the existing subgrid models do not incorporate information of non-ideal thermodynamic processes. Model refinements are warranted through future studies.

The final objective of this dissertation was to investigate modeling approaches for the filtered equation of state used to compute the filtered density. Four different modeling approaches for the filtered density are proposed and assessed in an *a priori* study. The representation of the filtered equation of state in terms of Reynolds-filtered state variables does not provide appreciable advantages over the current no-model approach. A dynamic gradient model and scale-similarity model are formulated using the subgrid modeling principles that have been investigated for the subgrid stresses. These models provide good improvements to the computation of the filtered density, with some outstanding issues that require further refinements. The presumed-FDF approach in which a beta-PDF is used to represent the subgrid scale distribution of the scalar field shows the overall best performance with errors less than 2-5% even at coarse filter resolutions.

8.2 Major contributions of this dissertation

The most important contributions from this dissertation are summarized as follows.

1. A consistent theoretical framework of the filtered conservation equations for LES of supercritical mixing and combustion is established. The derived framework is suited for all multi-physics flow regimes and provides a basis for future investigations.
2. Direct numerical simulations of non-reacting and reacting methane-oxygen mixing layers are conducted at realistic operating conditions representative of liquid rocket engine operation. These unique datasets describe high Reynolds number, spatially evolving, inhomogeneous turbulent flows at supercritical conditions, and provide rich information that can be used to derive key insights for refining modeling approaches in this regime.
3. Two new groups of subgrid terms are shown to have important significance to the governing filtered equations in the supercritical regime. The discrepancies associated with the use of Favre-filtered state variables for computation of thermodynamic and transport quantities are quantified. Parametric studies as a function of filter width have broadened the understanding regarding the relevance of these outstanding issues for LES resolutions employed in practice.
4. Assessments of two state-of-the-art turbulence models are conducted for non-reacting and reacting cases. The superiority of tensorial models, such as the scale-similarity model, is demonstrated. It is also shown that resolution requirements are to be considered to ensure model accuracies for high-fidelity simulations, especially for reacting flows. The quantitative trends established in this work offer guidelines for resolution requirements for accurate LES simulations.

5. Modeling approaches for the filtered equation of state are proposed and investigated in an *a priori* sense for the supercritical mixing case. Improved accuracy in the representation of the filtered density is demonstrated. The modeling frameworks are conceived to serve as a foundation for future modeling efforts.

8.3 Recommended directions for future work

The long-term goal of this research is to develop a refined and consistent subgrid modeling framework for LES of supercritical mixing and combustion that accurately represents all relevant complex physico-chemical thermodynamic processes at the subgrid level. Reflecting upon the conclusions reached in this dissertation, and the limitations with the current work, the following directions are recommended for future work in this topic.

8.3.1 Three-dimensional DNS studies

A major limitation with the current work is the use of two-dimensional DNS data. This approximation was considered necessary at the time of this study owing to limitations in availability of computational resources and to enable realization of spatially inhomogeneous flows at realistic Reynolds numbers within the available resources. The conclusions reached from this study are valuable in identifying focal points for future research. Recent studies [99, 101, 102, 171] focusing on the subgrid modeling issues in supercritical turbulent flows at low Reynolds numbers also corroborate these findings. Future studies should focus on realizing three-dimensional DNS simulations for similar operating conditions, whenever such studies are computationally feasible. The data from such a study would be useful to provide more detailed physical insights regarding the

effects and importance of accounting for the subgrid terms. The degree of agreement between results from future three-dimensional studies and the conclusions of this study would possibly render more support for analyses of two-dimensional data for parametric study of the effect of flow conditions on the subgrid contributions.

In addition to the magnitude analysis of the resolved and subgrid fluxes conducted in this work, the directional properties of the fluxes are also relevant to accurately represent the transport phenomena at the subgrid scales, and in turn the resolved scales. Preliminary studies in this dissertation have found that there are differences between the orientations of the resolved and the exact filtered fluxes. These effects are especially relevant for multicomponent mixtures where complex phenomena are encountered, such as countergradient diffusion [22, 176, 186]. These effects have a direct impact on the species mixing, chemical heat release and flow dynamics in reacting flows. Three-dimensional data is essential for investigating such issues.

8.3.2 Subgrid model development

Although there seem to be a lot of new subgrid terms in the derived filtered equations, half of those terms are related to the EOS. The subgrid terms associated with the EOS are also the terms are most relevant in magnitude. These terms can be accounted for by modeling the filtered EOS consistently. The subgrid modeling approaches proposed for the equation of state in Chapter 7 can be used as a starting point but need to be rigorously tested under different flow conditions before they can be incorporated into LES simulations. Further refinements to the modeling approaches are also warranted to resolve outstanding issues pointed out in Chapter 7.

The remaining terms are those associated with the diffusive fluxes. Their magnitudes are small with respect to the leading order of the equations. As a first step, they could possibly be neglected, and emphasis laid on the larger terms associated with the EOS. The need for modeling the subgrid diffusive fluxes also requires further insights through detailed three-dimensional data. It is essential to understand the degree to which these terms affect the physics at the resolved scales, before modeling efforts are undertaken. In principle, scale-similarity approaches could be extended to model the subgrid diffusive fluxes, under the strict criterion that similarity of scales is valid for the range of filter scales and flow regime considered. For example, Martin et al. [81] investigated the scale-similarity approach to model the turbulent diffusion and subgrid viscous diffusion terms for compressible flows. Another potential candidate is the use of approximate deconvolution [58, 200] or inverse filtering methods that can provide an estimate for the unfiltered flow fields, thereby allowing a direct computation of the filtered fluxes.

The benefits of modeling the subgrid terms and the effectiveness of the developed models also need to be verified in *a posteriori* LES studies. Efforts in this direction would require substantial computational resources and time, but is essential before the adoption of the refined framework.

REFERENCES

[1] J. C. Oefelein, "Advances in modeling supercritical fluid behavior and combustion in high-pressure propulsion systems," in *AIAA Scitech 2019 Forum*, 2019, p. 0634.

[2] K. Brun, P. Friedman, and R. Dennis, *Fundamentals and applications of supercritical carbon dioxide (sCO2) based power cycles*. Woodhead publishing, 2017.

[3] V. Yang, "Modeling of supercritical vaporization, mixing, and combustion processes in liquid-fueled propulsion systems," *Proceedings of the Combustion Institute,* vol. 28, no. 1, pp. 925-942, 2000, doi: 10.1016/s0082-0784(00)80299-4.

[4] J. Bellan, "Supercritical (and subcritical) fluid behavior and modeling: drops, streams, shear and mixing layers, jets and sprays," *Progress in Energy and Combustion Science,* vol. 26, no. 4, pp. 329-366, 2000/08/01/ 2000, doi: https://doi.org/10.1016/S0360-1285(00)00008-3.

[5] E. Lemmon, I. H. Bell, M. Huber, and M. McLinden, "NIST Standard Reference Database 23: Reference Fluid Thermodynamic and Transport Properties-REFPROP, Version 10.0, National Institute of Standards and Technology," *Standard Reference Data Program, Gaithersburg,* 2018.

[6] W. Mayer and H. Tamura, "Propellant injection in a liquid oxygen/gaseous hydrogen rocket engine," *Journal of Propulsion and Power,* vol. 12, no. 6, pp. 1137-1147, 1996.

[7] W. O. Mayer *et al.*, "Atomization and breakup of cryogenic propellants under high-pressure subcritical and supercritical conditions," *Journal of Propulsion and Power,* vol. 14, no. 5, pp. 835-842, 1998.

[8] W. Mayer, A. Schik, M. Schaf fler, and H. Tamura, "Injection and mixing processes in high-pressure liquid oxygen/gaseous hydrogen rocket combustors," *Journal of Propulsion and Power,* vol. 16, no. 5, pp. 823-828, 2000.

[9] B. Chehroudi, D. Talley, and E. Coy, "Visual characteristics and initial growth rates of round cryogenic jets at subcritical and supercritical pressures," *Physics of Fluids,* vol. 14, no. 2, pp. 850-861, 2002, doi: 10.1063/1.1430735.

[10] C. Segal and S. A. Polikhov, "Subcritical to supercritical mixing," *Physics of Fluids,* vol. 20, no. 5, p. 052101, 2008, doi: 10.1063/1.2912055.

[11] B. Chehroudi, "Recent Experimental Efforts on High-Pressure Supercritical Injection for Liquid Rockets and Their Implications," *International Journal of Aerospace Engineering,* vol. 2012, pp. 1-31, 2012, doi: 10.1155/2012/121802.

[12] M. Oschwald *et al.*, "Injection of fluids into supercritical environments," *Combustion Science and Technology,* vol. 178, no. 1-3, pp. 49-100, 2006, doi: 10.1080/00102200500292464.

[13] M. Habiballah, M. Orain, F. Grisch, L. Vingert, and P. Gicquel, "Experimental studies of high-pressure cryogenic flames on the mascotte facility," *Combustion Science and Technology,* vol. 178, no. 1-3, pp. 101-128, 2006.

[14] R. N. Dahms and J. C. Oefelein, "On the transition between two-phase and single-phase interface dynamics in multicomponent fluids at supercritical pressures," *Physics of Fluids,* vol. 25, no. 9, p. 092103, 2013, doi: 10.1063/1.4820346.

[15] R. N. Dahms and J. C. Oefelein, "Liquid jet breakup regimes at supercritical pressures," *Combustion and Flame,* vol. 162, no. 10, pp. 3648-3657, 2015, doi: 10.1016/j.combustflame.2015.07.004.

[16] R. N. Dahms and J. C. Oefelein, "Non-equilibrium gas–liquid interface dynamics in high-pressure liquid injection systems," *Proceedings of the Combustion Institute,* vol. 35, no. 2, pp. 1587-1594, 2015, doi: 10.1016/j.proci.2014.05.155.

[17] R. N. Dahms, "Understanding the breakdown of classic two-phase theory and spray atomization at engine-relevant conditions," *Physics of Fluids,* vol. 28, no. 4, p. 042108, 2016, doi: 10.1063/1.4946000.

[18] G. G. Simeoni *et al.*, "The Widom line as the crossover between liquid-like and gas-like behaviour in supercritical fluids," *Nature Physics,* vol. 6, no. 7, pp. 503-507, 2010, doi: 10.1038/nphys1683.

[19] D. T. Banuti, "Crossing the Widom-line – Supercritical pseudo-boiling," *The Journal of Supercritical Fluids,* vol. 98, pp. 12-16, 2015, doi: 10.1016/j.supflu.2014.12.019.

[20] P. E. Lapenna, "Characterization of pseudo-boiling in a transcritical nitrogen jet," *Physics of Fluids,* vol. 30, no. 7, p. 077106, 2018, doi: 10.1063/1.5038674.

[21] R. S. Miller, K. G. Harstad, and J. Bellan, "Direct numerical simulations of supercritical fluid mixing layers applied to heptane–nitrogen," *Journal of Fluid Mechanics,* vol. 436, pp. 1-39, 2001, doi: 10.1017/s0022112001003895.

[22] J. Bellan, "Theory, modeling and analysis of turbulent supercritical mixing," *Combustion Science and Technology,* vol. 178, no. 1-3, pp. 253-281, 2006, doi: 10.1080/00102200500292241.

[23] R. Branam and W. Mayer, "Characterization of cryogenic injection at supercritical pressure," *Journal of Propulsion and power,* vol. 19, no. 3, pp. 342-355, 2003.

[24] A. Roy and C. Segal, "Experimental study of fluid jet mixing at supercritical conditions," *Journal of Propulsion and Power,* vol. 26, no. 6, pp. 1205-1211, 2010.

[25] P. J. Linstrom and W. G. Mallard, "The NIST Chemistry WebBook: A chemical data resource on the internet," *Journal of Chemical & Engineering Data,* vol. 46, no. 5, pp. 1059-1063, 2001.

[26] J. C. Oefelein and V. Yang, "Modeling high-pressure mixing and combustion processes in liquid rocket engines," *Journal of Propulsion and Power,* vol. 14, no. 5, pp. 843-857, 1998.

[27] H. Meng and V. Yang, "A unified treatment of general fluid thermodynamics and its application to a preconditioning scheme," *Journal of Computational Physics,* vol. 189, no. 1, pp. 277-304, 2003, doi: 10.1016/s0021-9991(03)00211-0.

[28] C. Pantano, R. Saurel, and T. Schmitt, "An oscillation free shock-capturing method for compressible van der Waals supercritical fluid flows," *Journal of Computational Physics,* vol. 335, pp. 780-811, 2017, doi: 10.1016/j.jcp.2017.01.057.

[29] H. Terashima and M. Koshi, "Approach for simulating gas–liquid-like flows under supercritical pressures using a high-order central differencing scheme," *Journal of Computational Physics,* vol. 231, no. 20, pp. 6907-6923, 2012/08/15/ 2012, doi: https://doi.org/10.1016/j.jcp.2012.06.021.

[30] H. Terashima and M. Koshi, "Strategy for simulating supercritical cryogenic jets using high-order schemes," *Computers & Fluids,* vol. 85, pp. 39-46, 2013/10/01/ 2013, doi: https://doi.org/10.1016/j.compfluid.2012.09.032.

[31] G. Lacaze, T. Schmitt, A. Ruiz, and J. C. Oefelein, "Comparison of energy-, pressure- and enthalpy-based approaches for modeling supercritical flows," *Computers & Fluids,* vol. 181, pp. 35-56, 2019, doi: 10.1016/j.compfluid.2019.01.002.

[32] T. Schmitt, L. Selle, A. Ruiz, and B. Cuenot, "Large-eddy simulation of supercritical-pressure round jets," *AIAA journal,* vol. 48, no. 9, pp. 2133-2144, 2010.

[33] T. Schmitt, J. Rodriguez, I. Leyva, and S. Candel, "Experiments and numerical simulation of mixing under supercritical conditions," *Physics of Fluids,* vol. 24, no. 5, p. 055104, 2012.

[34] P. C. Ma, Y. Lv, and M. Ihme, "An entropy-stable hybrid scheme for simulations of transcritical real-fluid flows," *Journal of Computational Physics,* vol. 340, pp. 330-357, 2017, doi: 10.1016/j.jcp.2017.03.022.

[35] P. Tudisco and S. Menon, "Numerical Investigations of Phase-Separation During Multi-Component Mixing at Super-Critical Conditions," *Flow, Turbulence and Combustion,* vol. 104, no. 2-3, pp. 693-724, 2020, doi: 10.1007/s10494-019-00101-4.

[36] R. Abgrall and S. Karni, "Computations of compressible multifluids," *Journal of computational physics,* vol. 169, no. 2, pp. 594-623, 2001.

[37] E. P. Bruce, M. P. John, and P. O. C. John, *Properties of Gases and Liquids, Fifth Edition*, Fifth edition. ed. New York: McGraw-Hill Education (in en), 2001.

[38] J. Manin, M. Bardi, L. M. Pickett, R. N. Dahms, and J. C. Oefelein, "Microscopic investigation of the atomization and mixing processes of diesel sprays injected into high pressure and temperature environments," *Fuel,* vol. 134, pp. 531-543, 2014, doi: 10.1016/j.fuel.2014.05.060.

[39] C. Crua, J. Manin, and L. M. Pickett, "On the transcritical mixing of fuels at diesel engine conditions," *Fuel,* vol. 208, pp. 535-548, 2017/11/15/ 2017, doi: https://doi.org/10.1016/j.fuel.2017.06.091.

[40] C. Traxinger, M. Pfitzner, S. Baab, G. Lamanna, and B. Weigand, "Experimental and numerical investigation of phase separation due to multicomponent mixing at high-pressure conditions," *Physical Review Fluids,* vol. 4, no. 7, 2019, doi: 10.1103/physrevfluids.4.074303.

[41] J. Matheis and S. Hickel, "Multi-component vapor-liquid equilibrium model for LES of high-pressure fuel injection and application to ECN Spray A," *International Journal of Multiphase Flow,* vol. 99, pp. 294-311, 2018/02/01/ 2018, doi: https://doi.org/10.1016/j.ijmultiphaseflow.2017.11.001.

[42] L. Qiu and R. D. Reitz, "An investigation of thermodynamic states during high-pressure fuel injection using equilibrium thermodynamics," *International Journal of Multiphase Flow,* vol. 72, pp. 24-38, 2015/06/01/ 2015, doi: https://doi.org/10.1016/j.ijmultiphaseflow.2015.01.011.

[43] L. Jofre and J. Urzay, "Transcritical diffuse-interface hydrodynamics of propellants in high-pressure combustors of chemical propulsion systems," *Progress in Energy and Combustion Science,* vol. 82, p. 100877, 2021/01/01/ 2021, doi: https://doi.org/10.1016/j.pecs.2020.100877.

[44] J. Bellan, *High-pressure Flows for Propulsion Applications*. American Institute of Aeronautics and Astronautics, Incorporated, 2020.

[45] J. Bellan, "Future Challenges in the Modelling and Simulations of High-pressure Flows," *Combustion Science and Technology,* vol. 192, no. 7, pp. 1199-1218, 2020, doi: 10.1080/00102202.2020.1719404.

[46] N. A. Okong'O and J. Bellan, "Direct numerical simulation of a transitional supercritical binary mixing layer: heptane and nitrogen," *Journal of Fluid Mechanics,* vol. 464, pp. 1-34, 2002, doi: 10.1017/s0022112002008480.

[47] T. Poinsot, S. Candel, and A. Trouvé, "Applications of direct numerical simulation to premixed turbulent combustion," *Progress in Energy and Combustion Science,* vol. 21, no. 6, pp. 531-576, 1995.

[48] L. Vervisch and T. Poinsot, "Direct numerical simulation of non-premixed turbulent flames," *Annual review of fluid mechanics,* vol. 30, no. 1, pp. 655-691, 1998.

[49] J. H. Chen, "Petascale direct numerical simulation of turbulent combustion—fundamental insights towards predictive models," *Proceedings of the Combustion Institute,* vol. 33, no. 1, pp. 99-123, 2011.

[50] J. Smagorinsky, "General Circulation Experiments with the Primitive Equations I. The Basic Experiment," *Monthly Weather Review,* vol. 91, no. 3, pp. 99-164, 1963, doi: 10.1175/1520-0493(1963)091<0099:gcewtp>2.3.co;2.

[51] J. W. Deardorff, "A numerical study of three-dimensional turbulent channel flow at large Reynolds numbers," *Journal of Fluid Mechanics,* vol. 41, no. 2, pp. 453-480, 1970, doi: 10.1017/s0022112070000691.

[52] U. Piomelli, W. H. Cabot, P. Moin, and S. Lee, "Subgrid-scale backscatter in turbulent and transitional flows," *Physics of Fluids A: Fluid Dynamics,* vol. 3, no. 7, pp. 1766-1771, 1991, doi: 10.1063/1.857956.

[53] M. Germano, U. Piomelli, P. Moin, and W. H. Cabot, "A dynamic subgrid-scale eddy viscosity model," *Physics of Fluids A: Fluid Dynamics,* vol. 3, no. 7, pp. 1760-1765, 1991, doi: 10.1063/1.857955.

[54] M. Germano, "Turbulence: the filtering approach," *Journal of Fluid Mechanics,* vol. 238, pp. 325-336, 1992.

[55] J. Bardina, "Improved turbulence models based on large eddy simulation of homogeneous, incompressible, turbulent flows," Ph.D. Thesis, Stanford University, 8320678, 1983.

[56] S. Liu, C. Meneveau, and J. Katz, "On the properties of similarity subgrid-scale models as deduced from measurements in a turbulent jet," *Journal of Fluid Mechanics,* vol. 275, no. -1, pp. 83-119, 1994, doi: 10.1017/s0022112094002296.

[57] R. A. Clark, J. H. Ferziger, and W. C. Reynolds, "Evaluation of subgrid-scale models using an accurately simulated turbulent flow," *Journal of Fluid Mechanics,* vol. 91, no. 01, p. 1, 1979, doi: 10.1017/s002211207900001x.

[58] S. Stolz and N. A. Adams, "An approximate deconvolution procedure for large-eddy simulation," *Physics of Fluids,* vol. 11, no. 7, pp. 1699-1701, 1999, doi: 10.1063/1.869867.

[59] S. Stolz, N. A. Adams, and L. Kleiser, "An approximate deconvolution model for large-eddy simulation with application to incompressible wall-bounded flows," *Physics of Fluids,* vol. 13, no. 4, pp. 997-1015, 2001, doi: 10.1063/1.1350896.

[60] P. Sagaut, *Large eddy simulation for incompressible flows: an introduction*. Springer Science & Business Media, 2006.

[61] C. Meneveau and J. Katz, "Scale-Invariance and Turbulence Models for Large-Eddy Simulation," *Annual Review of Fluid Mechanics,* vol. 32, no. 1, pp. 1-32, 2000, doi: 10.1146/annurev.fluid.32.1.1.

[62] U. Piomelli, "Chapter Three - Large-eddy simulations," in *Advanced Approaches in Turbulence*, P. Durbin Ed.: Elsevier, 2021, pp. 83-131.

[63] A. Yoshizawa, "Statistical theory for compressible turbulent shear flows, with the application to subgrid modeling," *Physics of Fluids,* vol. 29, no. 7, p. 2152, 1986, doi: 10.1063/1.865552.

[64] P. Moin, K. Squires, W. Cabot, and S. Lee, "A dynamic subgrid-scale model for compressible turbulence and scalar transport," *Physics of Fluids A: Fluid Dynamics,* vol. 3, no. 11, pp. 2746-2757, 1991, doi: 10.1063/1.858164.

[65] G. Erlebacher, M. Y. Hussaini, C. G. Speziale, and T. A. Zang, "Toward the large-eddy simulation of compressible turbulent flows," *Journal of Fluid Mechanics,* vol. 238, no. -1, pp. 155-185, 1992, doi: 10.1017/s0022112092001678.

[66] J. Bardina, J. Ferziger, and W. Reynolds, "Improved subgrid-scale models for large-eddy simulation," in *13th fluid and plasmadynamics conference*, 1980, p. 1357.

[67] B. Vreman, B. Geurts, and H. Kuerten, "Subgrid-modelling in LES of compressible flow," *Applied Scientific Research,* vol. 54, no. 3, pp. 191-203, 1995, doi: 10.1007/bf00849116.

[68] J. C. Oefelein, R. W. Schefer, and R. S. Barlow, "Toward validation of large eddy simulation for turbulent combustion," *AIAA journal,* vol. 44, no. 3, pp. 418-433, 2006.

[69] H. Pitsch, "Large-Eddy Simulation of Turbulent Combustion," *Annual Review of Fluid Mechanics,* vol. 38, no. 1, pp. 453-482, 2006, doi: 10.1146/annurev.fluid.38.050304.092133.

[70] A. W. Cook and J. J. Riley, "A subgrid model for equilibrium chemistry in turbulent flows," *Physics of Fluids,* vol. 6, no. 8, pp. 2868-2870, 1994, doi: 10.1063/1.868111.

[71] C. D. Pierce and P. Moin, "Progress-variable approach for large-eddy simulation of non-premixed turbulent combustion," *Journal of Fluid Mechanics,* vol. 504, pp. 73-97, 2004, doi: 10.1017/s0022112004008213.

[72] S. H. Kim and H. Pitsch, "Conditional filtering method for large-eddy simulation of turbulent nonpremixed combustion," *Physics of Fluids,* vol. 17, no. 10, p. 105103, 2005, doi: 10.1063/1.2084229.

[73] S. B. Pope, "Computations of turbulent combustion: Progress and challenges," *Symposium (International) on Combustion,* vol. 23, no. 1, pp. 591-612, 1991, doi: 10.1016/s0082-0784(06)80307-3.

[74] P. J. Colucci, F. A. Jaberi, P. Givi, and S. B. Pope, "Filtered density function for large eddy simulation of turbulent reacting flows," *Physics of Fluids,* vol. 10, no. 2, pp. 499-515, 1998, doi: 10.1063/1.869537.

[75] P. Moin and K. Mahesh, "DIRECT NUMERICAL SIMULATION: A Tool in Turbulence Research," *Annual Review of Fluid Mechanics,* vol. 30, no. 1, pp. 539-578, 1998, doi: 10.1146/annurev.fluid.30.1.539.

[76] P. Trisjono and H. Pitsch, "Systematic Analysis Strategies for the Development of Combustion Models from DNS: A Review," *Flow, Turbulence and Combustion,* vol. 95, no. 2-3, pp. 231-259, 2015, doi: 10.1007/s10494-015-9645-x.

[77] E. R. Hawkes, R. Sankaran, J. C. Sutherland, and J. H. Chen, "Direct numerical simulation of turbulent combustion: fundamental insights towards predictive models," in *Journal of Physics: Conference Series*, 2005, vol. 16, no. 1: IOP Publishing, p. 009.

[78] O. J. McMillan and J. H. Ferziger, "Direct testing of subgrid-scale models," *Aiaa Journal,* vol. 17, no. 12, pp. 1340-1346, 1979.

[79] U. Piomelli, P. Moin, and J. H. Ferziger, "Model consistency in large eddy simulation of turbulent channel flows," *Physics of Fluids,* vol. 31, no. 7, p. 1884, 1988, doi: 10.1063/1.866635.

[80] B. Vreman, B. Geurts, and H. Kuerten, "A priori tests of large eddy simulation of the compressible plane mixing layer," *Journal of Engineering Mathematics,* vol. 29, no. 4, pp. 299-327, 1995, doi: 10.1007/bf00042759.

[81] M. P. Martin, U. Piomelli, and G. V. Candler, "Subgrid-scale models for compressible large-eddy simulations," *Theoretical and Computational Fluid Dynamics,* vol. 13, no. 5, pp. 361-376, 2000, doi: 10.1007/pl00020896.

[82] U. Piomelli, "Large-eddy simulation: achievements and challenges," *Progress in Aerospace Sciences,* vol. 35, no. 4, pp. 335-362, 1999, doi: 10.1016/s0376-0421(98)00014-1.

[83] M. Lesieur and O. Metais, "New Trends in Large-Eddy Simulations of Turbulence," *Annual Review of Fluid Mechanics,* vol. 28, no. 1, pp. 45-82, 1996, doi: 10.1146/annurev.fl.28.010196.000401.

[84] K. Mahesh, "Direct numerical and large–eddy simulation of complex turbulent flows," Elsevier, 2021, pp. 33-81.

[85] J. C. Oefelein, "Large eddy simulation of turbulent combustion processes in propulsion and power systems," *Progress in Aerospace Sciences,* vol. 42, no. 1, pp. 2-37, 2006.

[86] C. Fureby, "Towards the use of large eddy simulation in engineering," *Progress in Aerospace Sciences,* vol. 44, no. 6, pp. 381-396, 2008.

[87] G. Lacaze, A. Misdariis, A. Ruiz, and J. C. Oefelein, "Analysis of high-pressure Diesel fuel injection processes using LES with real-fluid thermodynamics and transport," *Proceedings of the Combustion Institute,* vol. 35, no. 2, pp. 1603-1611, 2015.

[88] J. C. Oefelein, "Mixing and combustion of cryogenic oxygen-hydrogen shear-coaxial jet flames at supercritical pressure," *Combustion Science and Technology,* vol. 178, no. 1-3, pp. 229-252, 2006, doi: 10.1080/00102200500325322.

[89] N. Zong, H. Meng, S.-Y. Hsieh, and V. Yang, "A numerical study of cryogenic fluid injection and mixing under supercritical conditions," *Physics of Fluids,* vol. 16, no. 12, pp. 4248-4261, 2004, doi: 10.1063/1.1795011.

[90] N. Zong and V. Yang, "Near-field flow and flame dynamics of LOX/methane shear-coaxial injector under supercritical conditions," *Proceedings of the Combustion Institute,* vol. 31, no. 2, pp. 2309-2317, 2007, doi: 10.1016/j.proci.2006.08.106.

[91] M. Masquelet, S. Menon, Y. Jin, and R. Friedrich, "Simulation of unsteady combustion in a LOX-GH2 fueled rocket engine," *Aerospace Science and Technology,* vol. 13, no. 8, pp. 466-474, 2009/12/01/ 2009, doi: https://doi.org/10.1016/j.ast.2009.07.005.

[92] X. Petit, G. Ribert, G. Lartigue, and P. Domingo, "Large-eddy simulation of supercritical fluid injection," *The Journal of Supercritical Fluids,* vol. 84, pp. 61-73, 2013, doi: 10.1016/j.supflu.2013.09.011.

[93] X. Wang and V. Yang, "Supercritical Mixing and Combustion of Liquid-Oxygen/ Kerosene Bi-Swirl Injectors," *Journal of Propulsion and Power,* vol. 33, no. 2, pp. 316-322, 2017, doi: 10.2514/1.b36262.

[94] X. Wang, L. Zhang, Y. Li, S.-T. Yeh, and V. Yang, "Supercritical combustion of gas-centered liquid-swirl coaxial injectors for staged-combustion engines," *Combustion and Flame,* vol. 197, pp. 204-214, 2018.

[95] M. Ihme, P. C. Ma, and L. Bravo, "Large eddy simulations of diesel-fuel injection and auto-ignition at transcritical conditions," *International Journal of Engine Research,* vol. 20, no. 1, pp. 58-68, 2019, doi: 10.1177/1468087418819546.

[96] P. C. Ma, H. Wu, T. Jaravel, L. Bravo, and M. Ihme, "Large-eddy simulations of transcritical injection and auto-ignition using diffuse-interface method and finite-rate chemistry," *Proceedings of the Combustion Institute,* vol. 37, no. 3, pp. 3303-3310, 2019.

[97] T. Schmitt, "Large-Eddy Simulations of the Mascotte test cases operating at supercritical pressure," *Flow, Turbulence and Combustion,* pp. 1-31, 2020.

[98] N. Okong'o, K. Harstad, and J. Bellan, "Direct numerical simulations of O/H temporal mixing layers under supercritical conditions," *AIAA journal,* vol. 40, no. 5, pp. 914-926, 2002.

[99] L. C. Selle, N. A. Okong'O, J. Bellan, and K. G. Harstad, "Modelling of subgrid-scale phenomena in supercritical transitional mixing layers: an a priori study," *Journal of Fluid Mechanics,* vol. 593, pp. 57-91, 2007, doi: 10.1017/s0022112007008075.

[100] G. Borghesi and J. Bellan, "A priori and a posteriori investigations for developing large eddy simulations of multi-species turbulent mixing under high-pressure conditions," *Physics of Fluids,* vol. 27, no. 3, p. 035117, 2015, doi: 10.1063/1.4916284.

[101] Z. Ma, A. Korucu, and R. S. Miller, "A priori analysis of subgrid scale pressure and heat flux in high pressure mixing and reacting shear layers," *Combustion Theory and Modelling,* vol. 19, no. 6, pp. 807-832, 2015, doi: 10.1080/13647830.2015.1100753.

[102] J. Foster and R. S. Miller, "A priori analysis of subgrid mass diffusion vectors in high pressure turbulent hydrogen/oxygen reacting shear layer flames," *Physics of Fluids,* vol. 24, no. 7, p. 075114, 2012, doi: 10.1063/1.4739065.

[103] P. E. Lapenna and F. Creta, "Mixing under transcritical conditions: An a-priori study using direct numerical simulation," *The Journal of Supercritical Fluids,* vol. 128, pp. 263-278, 2017, doi: 10.1016/j.supflu.2017.05.005.

[104] G. Ribert, X. Petit, and P. Domingo, "High-pressure methane-oxygen flames. Analysis of sub-grid scale contributions in filtered equations of state," *The Journal of Supercritical Fluids,* vol. 121, pp. 78-88, 2017, doi: 10.1016/j.supflu.2016.08.020.

[105] G. Ribert, P. Domingo, and L. Vervisch, "Analysis of sub-grid scale modeling of the ideal-gas equation of state in hydrogen–oxygen premixed flames," *Proceedings of the Combustion Institute,* vol. 37, no. 2, pp. 2345-2351, 2019, doi: 10.1016/j.proci.2018.07.054.

[106] P. E. Lapenna, G. Indelicato, R. Lamioni, and F. Creta, "Modeling the equations of state using a flamelet approach in LRE-like conditions," *Acta Astronautica,* vol. 158, pp. 460-469, 2019, doi: 10.1016/j.actaastro.2018.07.025.

[107] E. S. Taskinoglu and J. Bellan, "A posteriori study using a DNS database describing fluid disintegration and binary-species mixing under supercritical pressure: heptane and nitrogen," *Journal of Fluid Mechanics,* vol. 645, pp. 211-254, 2010, doi: 10.1017/s0022112009992606.

[108] K. Harstad and J. Bellan, "The Lewis number under supercritical conditions," *International Journal of Heat and Mass Transfer,* vol. 42, no. 6, pp. 961-970, 1999, doi: 10.1016/s0017-9310(98)00230-0.

[109] G. Ribert, N. Zong, V. Yang, L. Pons, N. Darabiha, and S. Candel, "Counterflow diffusion flames of general fluids: Oxygen/hydrogen mixtures," *Combustion and Flame,* vol. 154, no. 3, pp. 319-330, 2008, doi: 10.1016/j.combustflame.2008.04.023.

[110] S. Palle and R. S. Miller, "Analysis of high-pressure hydrogen, methane, and heptane laminar diffusion flames: Thermal diffusion factor modeling," *Combustion and Flame,* vol. 151, no. 4, pp. 581-600, 2007.

[111] S.-Y. Hsieh and V. Yang, "A Preconditioned Flux-Differencing Scheme for Chemically Reacting Flows at all Mach Numbers," *International Journal of Computational Fluid Dynamics,* vol. 8, no. 1, pp. 31-49, 1997, doi: 10.1080/10618569708940794.

[112] N. Zong and V. Yang, "An efficient preconditioning scheme for real-fluid mixtures using primitive pressure–temperature variables," *International Journal of Computational Fluid Dynamics,* vol. 21, no. 5-6, pp. 217-230, 2007, doi: 10.1080/10618560701584373.

[113] D.-Y. Peng and D. B. Robinson, "A new two-constant equation of state," *Industrial & Engineering Chemistry Fundamentals,* vol. 15, no. 1, pp. 59-64, 1976.

[114] O. Redlich and J. N. Kwong, "On the thermodynamics of solutions. V. An equation of state. Fugacities of gaseous solutions," *Chemical reviews,* vol. 44, no. 1, pp. 233-244, 1949.

[115] G. Soave, "Equilibrium constants from a modified Redlich-Kwong equation of state," *Chemical engineering science,* vol. 27, no. 6, pp. 1197-1203, 1972.

[116] K. C. Gottiparthi, R. Sankaran, A. M. Ruiz, G. Lacaze, and J. C. Oefelein, "Large eddy simulation of a supercritical fuel jet in cross flow using GPU-acceleration," in *54th AIAA Aerospace Sciences Meeting*, 2016, p. 1939.

[117] S. Yang, Y. Li, X. Wang, U. Unnikrishnan, V. Yang, and W. Sun, "Comparison of tabulation and correlated dynamic evaluation of real fluid properties for

supercritical mixing," presented at the 53rd AIAA/SAE/ASEE joint propulsion conference, 2017, AIAA 2017-4858.

[118] T. W. Leland and P. S. Chappelear, "The corresponding states principle—a review of current theory and practice," *Industrial & Engineering Chemistry,* vol. 60, no. 7, pp. 15-43, 1968.

[119] J. Rowlinson and I. Watson, "The prediction of the thermodynamic properties of fluids and fluid mixtures-I The principle of corresponding states and its extensions," *Chemical Engineering Science,* vol. 24, no. 10, pp. 1565-1574, 1969.

[120] R. C. Reid, J. M. Prausnitz, and B. E. Poling, "The properties of gases and liquids," 1987.

[121] G. J. Van Wylen and R. E. Sonntag, *Fundamentals of classical thermodynamics* (no. 536 VAN). 1985.

[122] J. F. Ely and H. Hanley, "Prediction of transport properties. 1. Viscosity of fluids and mixtures," *Industrial & Engineering Chemistry Fundamentals,* vol. 20, no. 4, pp. 323-332, 1981.

[123] J. F. Ely and H. Hanley, "Prediction of transport properties. 2. Thermal conductivity of pure fluids and mixtures," *Industrial & Engineering Chemistry Fundamentals,* vol. 22, no. 1, pp. 90-97, 1983.

[124] T. H. Chung, M. Ajlan, L. L. Lee, and K. E. Starling, "Generalized multiparameter correlation for nonpolar and polar fluid transport properties," *Industrial & engineering chemistry research,* vol. 27, no. 4, pp. 671-679, 1988.

[125] S. Takahashi, "Preparation of a generalized chart for the diffusion coefficients of gases at high pressures," *Journal of Chemical Engineering of Japan,* vol. 7, no. 6, pp. 417-420, 1975.

[126] R. B. Bird, W. E. Stewart, and E. N. Lightfoot, "Transport Phenomena " *John Wiley & Sons,* vol. 413, 1960.

[127] J. O. Hirschfelder, C. F. Curtiss, and R. B. Bird, "Molecular theory of gases and liquids," *Molecular theory of gases and liquids,* 1964.

[128] K. Harstad and J. Bellan, "An all-pressure fluid drop model applied to a binary mixture: heptane in nitrogen," *International Journal of Multiphase Flow,* vol. 26, no. 10, pp. 1675-1706, 2000.

[129] K. Harstad and J. Bellan, "Mixing rules for multicomponent mixture mass diffusion coefficients and thermal diffusion factors," *The Journal of chemical physics,* vol. 120, no. 12, pp. 5664-5673, 2004.

[130] K. Harstad and J. Bellan, "High-pressure binary mass diffusion coefficients for combustion applications," *Industrial & engineering chemistry research,* vol. 43, no. 2, pp. 645-654, 2004.

[131] S. B. Pope, *Turbulent flows*. Cambridge University Press, 2000.

[132] S. Ghosal and P. Moin, "The basic equations for the large eddy simulation of turbulent flows in complex geometry," *Journal of Computational Physics,* vol. 118, no. 1, pp. 24-37, 1995.

[133] S. A. Jordan, "A large-eddy simulation methodology in generalized curvilinear coordinates," *Journal of Computational Physics,* vol. 148, no. 2, pp. 322-340, 1999.

[134] H. van der Ven, "A family of large eddy simulation (LES) filters with nonuniform filter widths," *Physics of Fluids,* vol. 7, no. 5, pp. 1171-1172, 1995.

[135] O. V. Vasilyev, T. S. Lund, and P. Moin, "A general class of commutative filters for LES in complex geometries," *Journal of computational physics,* vol. 146, no. 1, pp. 82-104, 1998.

[136] A. L. Marsden, O. V. Vasilyev, and P. Moin, "Construction of commutative filters for LES on unstructured meshes," *Journal of Computational Physics,* vol. 175, no. 2, pp. 584-603, 2002.

[137] A. Favre, "Turbulence: Space-time statistical properties and behavior in supersonic flows," *Physics of Fluids,* vol. 26, no. 10, p. 2851, 1983, doi: 10.1063/1.864049.

[138] M. Germano, "A proposal for a redefinition of the turbulent stresses in the filtered Navier–Stokes equations," *Physics of Fluids,* vol. 29, no. 7, p. 2323, 1986, doi: 10.1063/1.865568.

[139] A. Leonard, "Energy cascade in large-eddy simulations of turbulent fluid flows," in *Advances in geophysics*, vol. 18: Elsevier, 1975, pp. 237-248.

[140] C. G. Speziale, "Galilean invariance of subgrid-scale stress models in the large-eddy simulation of turbulence," *Journal of Fluid Mechanics,* vol. 156, no. -1, p. 55, 1985, doi: 10.1017/s0022112085001987.

[141] J. Janicka and A. Sadiki, "Large eddy simulation of turbulent combustion systems," *Proceedings of the Combustion Institute,* vol. 30, no. 1, pp. 537-547, 2005, doi: 10.1016/j.proci.2004.08.279.

[142] P. Givi, "Filtered density function for subgrid scale modeling of turbulent combustion," *AIAA journal,* vol. 44, no. 1, pp. 16-23, 2006.

[143] N. Peters, "Turbulent combustion," ed: IOP Publishing, 2001.

[144] S. Menon and A. R. Kerstein, "The linear-eddy model," in *Turbulent combustion modeling*: Springer, 2011, pp. 221-247.

[145] D. K. Lilly, "On the application of the eddy viscosity concept in the inertial sub-range of turbulence," *NCAR manuscript,* vol. 123, 1966.

[146] D. K. Lilly, "A proposed modification of the Germano subgrid-scale closure method," *Physics of Fluids A: Fluid Dynamics,* vol. 4, no. 3, pp. 633-635, 1992, doi: 10.1063/1.858280.

[147] Y. Zang, R. L. Street, and J. R. Koseff, "A dynamic mixed subgrid-scale model and its application to turbulent recirculating flows," *Physics of Fluids A: Fluid Dynamics,* vol. 5, no. 12, pp. 3186-3196, 1993, doi: 10.1063/1.858675.

[148] B. Vreman, B. Geurts, and H. Kuerten, "On the formulation of the dynamic mixed subgrid-scale model," *Physics of Fluids,* vol. 6, no. 12, pp. 4057-4059, 1994, doi: 10.1063/1.868333.

[149] J. C. Oefelein, "Thermophysical characteristics of shear-coaxial LOX–H2 flames at supercritical pressure," *Proceedings of the Combustion Institute,* vol. 30, no. 2, pp. 2929-2937, 2005.

[150] A. M. Ruiz *et al.*, "Numerical benchmark for high-Reynolds-number supercritical flows with large density gradients," *AIAA Journal,* vol. 54, no. 5, pp. 1445-1460, 2016.

[151] M. M. Ameen and J. Abraham, "Are “2D DNS” results of turbulent fuel/air mixing layers useful for assessing subgrid-scale models?," *Numerical Heat Transfer, Part A: Applications,* vol. 69, no. 1, pp. 1-13, 2016, doi: 10.1080/10407782.2015.1052312.

[152] H. Huo and V. Yang, "Subgrid-scale models for large-eddy simulation of supercritical combustion," in *51st AIAA Aerospace Sciences Meeting including the New Horizons Forum and Aerospace Exposition*, 2013, p. 706.

[153] U. Unnikrishnan, H. Huo, X. Wang, and V. Yang, "Subgrid scale modeling considerations for large eddy simulation of supercritical turbulent mixing and combustion," *Physics of Fluids,* vol. 33, no. 7, p. 075112, 2021, doi: 10.1063/5.0055751.

[154] R. C. Swanson and E. Turkel, "On central-difference and upwind schemes," *Journal of computational physics,* vol. 101, no. 2, pp. 292-306, 1992.

[155] X. Wang, H. Huo, U. Unnikrishnan, and V. Yang, "A systematic approach to high-fidelity modeling and efficient simulation of supercritical fluid mixing and combustion," *Combustion and Flame,* vol. 195, pp. 203-215, 2018, doi: 10.1016/j.combustflame.2018.04.030.

[156] K. Hsieh, J. Shuen, and V. Yang, "Droplet vaporization in high-pressure environments I: Near critical conditions," *Combustion Science and Technology,* vol. 76, no. 1-3, pp. 111-132, 1991.

[157] J. Shuen, V. Yang, and C. Hsiao, "Combustion of liquid-fuel droplets in supercritical conditions," *Combustion and Flame,* vol. 89, no. 3-4, pp. 299-319, 1992.

[158] N. Zong and V. Yang, "Cryogenic fluid jets and mixing layers in transcritical and supercritical environments," *Combustion science and technology,* vol. 178, no. 1-3, pp. 193-227, 2006.

[159] X. Wang, H. Huo, Y. Wang, and V. Yang, "Comprehensive study of cryogenic fluid dynamics of swirl injectors at supercritical conditions," *AIAA journal,* vol. 55, no. 9, pp. 3109-3119, 2017.

[160] H. Pitsch, M. Chen, and N. Peters, "Unsteady flamelet modeling of turbulent hydrogen-air diffusion flames," in *Symposium (international) on combustion*, 1998, vol. 27, no. 1: Elsevier, pp. 1057-1064.

[161] X. Wang, H. Huo, and V. Yang, "Counterflow diffusion flames of oxygen and n-alkane hydrocarbons (CH4-C16H34) at subcritical and supercritical conditions," *Combustion Science and Technology,* vol. 187, no. 1-2, pp. 60-82, 2015.

[162] H. Huo, X. Wang, and V. Yang, "A general study of counterflow diffusion flames at subcritical and supercritical conditions: Oxygen/hydrogen mixtures," *Combustion and flame,* vol. 161, no. 12, pp. 3040-3050, 2014.

[163] L. Pons, N. Darabiha, and S. Candel, "Pressure effects on nonpremixed strained flames," *Combustion and Flame,* vol. 152, no. 1-2, pp. 218-229, 2008.

[164] J. Van Oijen, R. Bastiaans, G. Groot, and L. De Goey, "Direct numerical simulations of premixed turbulent flames with reduced chemistry: Validation and flamelet analysis," *Flow, Turbulence and Combustion,* vol. 75, no. 1, pp. 67-84, 2005.

[165] J. Van Oijen, R. Bastiaans, and L. De Goey, "Low-dimensional manifolds in direct numerical simulations of premixed turbulent flames," *Proceedings of the Combustion Institute,* vol. 31, no. 1, pp. 1377-1384, 2007.

[166] A. Vreman, J. Van Oijen, L. De Goey, and R. Bastiaans, "Direct numerical simulation of hydrogen addition in turbulent premixed Bunsen flames using flamelet-generated manifold reduction," *International journal of hydrogen energy,* vol. 34, no. 6, pp. 2778-2788, 2009.

[167] S. Mukhopadhyay, R. Bastiaans, J. van Oijen, and L. de Goey, "Analysis of a filtered flamelet approach for coarse DNS of premixed turbulent combustion," *Fuel,* vol. 144, pp. 388-399, 2015.

[168] C. Sung, C. K. Law, and J.-Y. Chen, "An augmented reduced mechanism for methane oxidation with comprehensive global parametric validation," in *Symposium (International) on Combustion*, 1998, vol. 27, no. 1: Elsevier, pp. 295-304.

[169] C. Sung, C. Law, and J.-Y. Chen, "Further validation of an augmented reduced mechanism for methane oxidation: Comparison of global parameters and detailed structure," *Combustion science and technology,* vol. 156, no. 1, pp. 201-220, 2000.

[170] U. Guven and G. Ribert, "Impact of non-ideal transport modeling on supercritical flow simulation," *Proceedings of the Combustion Institute,* vol. 37, no. 3, pp. 3255-3262, 2019, doi: 10.1016/j.proci.2018.05.013.

[171] S. M. Ovais, K. A. Kemenov, and R. S. Miller, "Direct numerical simulation of supercritical oxy-methane mixing layers with CO2 substituted counterparts," *Physics of Fluids,* vol. 33, no. 3, p. 035115, 2021, doi: 10.1063/5.0039166.

[172] E. Masi, J. Bellan, K. G. Harstad, and N. A. Okong'o, "Multi-species turbulent mixing under supercritical-pressure conditions: modelling, direct numerical simulation and analysis revealing species spinodal decomposition," *Journal of Fluid Mechanics,* vol. 721, pp. 578-626, 2013.

[173] L. Sciacovelli and J. Bellan, "The influence of the chemical composition representation according to the number of species during mixing in high-pressure turbulent flows," *Journal of Fluid Mechanics,* vol. 863, pp. 293-340, 2019.

[174] J. Bellan, "Direct numerical simulation of a high-pressure turbulent reacting temporal mixing layer," *Combustion and Flame,* vol. 176, pp. 245-262, 2017, doi: 10.1016/j.combustflame.2016.09.026.

[175] G. Singla, P. Scouflaire, C. Rolon, and S. Candel, "Transcritical oxygen/transcritical or supercritical methane combustion," *Proceedings of the combustion institute,* vol. 30, no. 2, pp. 2921-2928, 2005.

[176] R. Krishna, "Uphill diffusion in multicomponent mixtures," *Chemical Society Reviews,* vol. 44, no. 10, pp. 2812-2836, 2015.

[177] T. Poinsot and D. Veynante, *Theoretical and numerical combustion*. RT Edwards, Inc., 2005.

[178] C. Fureby, "Comparison of flamelet and finite rate chemistry LES for premixed turbulent combustion," presented at the 45th AIAA Aerospace Sciences Meeting and Exhibit, 2007, AIAA 2007-1413.

[179] A. J. Aspden, N. Zettervall, and C. Fureby, "An a priori analysis of a DNS database of turbulent lean premixed methane flames for LES with finite-rate chemistry," *Proceedings of the Combustion Institute,* vol. 37, no. 2, pp. 2601-2609, 2019, doi: 10.1016/j.proci.2018.05.017.

[180] P. E. Desjardin and S. H. Frankel, "Large eddy simulation of a nonpremixed reacting jet: Application and assessment of subgrid-scale combustion models," *Physics of Fluids,* vol. 10, no. 9, pp. 2298-2314, 1998, doi: 10.1063/1.869749.

[181] A. Y. Klimenko and R. W. Bilger, "Conditional moment closure for turbulent combustion," *Progress in energy and combustion science,* vol. 25, no. 6, pp. 595-687, 1999.

[182] T. Echekki and E. Mastorakos, *Turbulent combustion modeling: Advances, new trends and perspectives*. Springer Science & Business Media, 2010.

[183] E. S. Taşkinoğlu and J. Bellan, "Subgrid-scale models and large-eddy simulation of oxygen stream disintegration and mixing with a hydrogen or helium stream at supercritical pressure," *Journal of Fluid Mechanics,* vol. 679, pp. 156-193, 2011, doi: 10.1017/jfm.2011.130.

[184] U. Unnikrishnan, J. C. Oefelein, and V. Yang, "Direct numerical simulation of a liquid-oxygen/methane mixing layer at supercritical pressure," presented at the 2018 Joint Propulsion Conference, 2018, AIAA 2018-4564.

[185] U. Unnikrishnan, J. C. Oefelein, and V. Yang, "A priori analysis of subfilter scalar covariance fields in turbulent reacting LOX-CH4 mixing layers," presented at the AIAA Scitech 2019 Forum, 2019, AIAA 2019-1495.

[186] D. Veynante, A. Trouvé, K. Bray, and T. Mantel, "Gradient and counter-gradient scalar transport in turbulent premixed flames," *Journal of Fluid Mechanics,* vol. 332, pp. 263-293, 1997.

[187] Y. Gao, M. Klein, and N. Chakraborty, "Assessment of sub-grid scalar flux modelling in premixed flames for Large Eddy Simulations: A-priori Direct Numerical Simulation analysis," *European Journal of Mechanics-B/Fluids,* vol. 52, pp. 97-108, 2015.

[188] A. Gnanaskandan and J. R. Bellan, "Large Eddy Simulations of high pressure jets: Effect of subgrid scale modeling," presented at the 55th AIAA Aerospace Sciences Meeting, 2017, 2017-1105.

[189] U. Unnikrishnan, X. Wang, S. Yang, and V. Yang, "Subgrid scale modeling of the equation of state for turbulent flows under supercritical conditions," presented at the 53rd AIAA/SAE/ASEE Joint Propulsion Conference, 2017, AIAA 2017-4855.

[190] S. Ghosal, T. S. Lund, P. Moin, and K. Akselvoll, "A dynamic localization model for large-eddy simulation of turbulent flows," *Journal of Fluid Mechanics,* vol. 286, no. -1, pp. 229-255, 1995, doi: 10.1017/s0022112095000711.

[191] T. Drozda, M. Sheikhi, C. Madnia, and P. Givi, "Developments in formulation and application of the filtered density function," *Flow, Turbulence and Combustion,* vol. 78, no. 1, pp. 35-67, 2007.

[192] D. C. Haworth, "Progress in probability density function methods for turbulent reacting flows," *Progress in Energy and combustion Science,* vol. 36, no. 2, pp. 168-259, 2010.

[193] C. Wall, B. J. Boersma, and P. Moin, "An evaluation of the assumed beta probability density function subgrid-scale model for large eddy simulation of nonpremixed, turbulent combustion with heat release," *Physics of Fluids,* vol. 12, no. 10, p. 2522, 2000, doi: 10.1063/1.1287911.

[194] F. A. Jaberi, P. J. Colucci, S. James, P. Givi, and S. B. Pope, "Filtered mass density function for large-eddy simulation of turbulent reacting flows," *Journal of Fluid Mechanics,* vol. 401, pp. 85-121, 1999, doi: 10.1017/s0022112099006643.

[195] P. Sagaut and M. Germano, "On the filtering paradigm for LES of flows with discontinuities," *Journal of Turbulence,* vol. 6, p. N23, 2005, doi: 10.1080/14685240500149799.

[196] D. V. Kotov, H. C. Yee, A. A. Wray, A. Hadjadj, and B. Sjögreen, "High Order Numerical Methods for the Dynamic SGS Model of Turbulent Flows with Shocks," *Communications in Computational Physics,* vol. 19, no. 2, pp. 273-300, 2016, doi: 10.4208/cicp.211014.040915a.

[197] C. D. Pierce and P. Moin, "A dynamic model for subgrid-scale variance and dissipation rate of a conserved scalar," *Physics of Fluids,* vol. 10, no. 12, pp. 3041-3044, 1998, doi: 10.1063/1.869832.

[198] P. Kundu, M. M. Ameen, C. Xu, U. Unnikrishnan, T. Lu, and S. Som, "Implementation of Detailed Chemistry Mechanisms in Engine Simulations," *Journal of Engineering for Gas Turbines and Power,* vol. 141, no. 1, 2019, doi: 10.1115/1.4041281.

[199] X. Petit, G. Ribert, and P. Domingo, "Framework for real-gas compressible reacting flows with tabulated thermochemistry," *The Journal of Supercritical Fluids,* vol. 101, pp. 1-16, 2015.

[200] P. Domingo and L. Vervisch, "DNS and approximate deconvolution as a tool to analyse one-dimensional filtered flame sub-grid scale modelling," *Combustion and Flame,* vol. 177, pp. 109-122, 2017.